Noncovalent Functionalization of 1D and 2D Nanomaterials

Leire de Juan Fernández

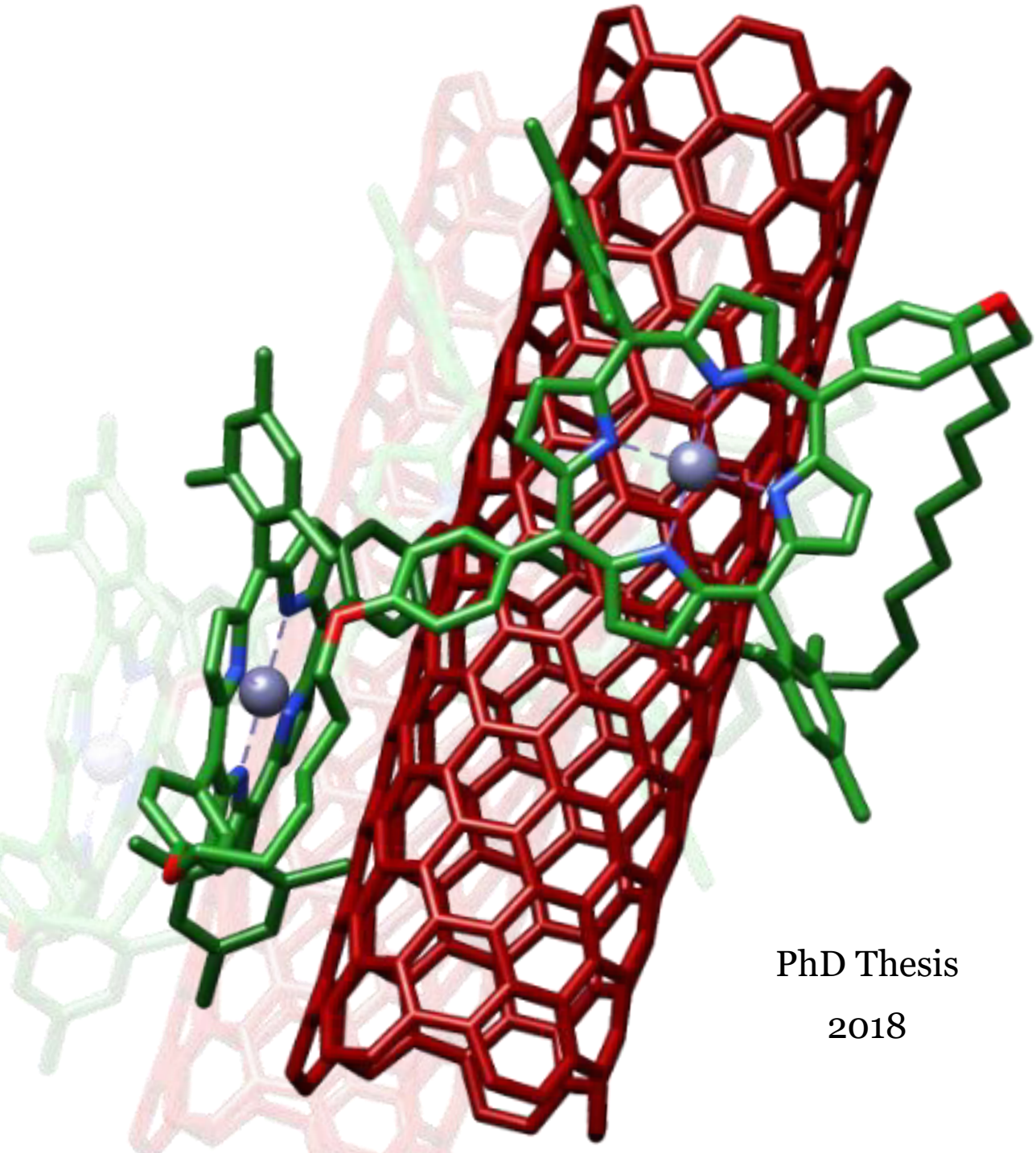

PhD Thesis

2018

NONCOVALENT FUNCTIONALIZATION OF 1D AND 2D NANOMATERIALS

PhD Thesis

Leire de Juan Fernández

Madrid, 2018

Director de Tesis:

Prof. Emilio M. Pérez

Tutor académico:

Dr. Giovanni Bottari

Memoria presentada por

Leire de Juan Fernández

para optar al título de DOCTOR EN QUÍMICA ORGÁNICA

Departamento de Química Orgánica

Universidad Autónoma de Madrid

Instituto IMDEA Nanociencia

Madrid, 2018

A mi familia

Agradecimientos

Llega el momento de poder agradeceros toda vuestra ayuda y deciros lo importante que sois para mí para que hoy esté escribiendo esta tesis. Han sido más de 4 años de mucho trabajo, pero en los que he coincidido y aprendido con personas maravillosas.

Quiero empezar expresando mi agradecimiento a Emilio, por darme esta oportunidad. Ha sido una gran etapa, tanto profesional como personal. Gracias por todo lo que me has enseñado, por tu apoyo y por estar siempre dispuesto a ayudarme, encontrando siempre solución a mis dudas y dificultades. Gracias por estos años de tesis. Me gustaría agradecer también al Ministerio de Educación la financiación recibida durante esta tesis, y durante mi estancia en el Reino Unido.

A Quino, por haberme metido en esto. Por acogerme desde bien joven en tu grupo de investigación y por tus ánimos para que siguiera adelante hasta llegar aquí. Gracias por ayudarme siempre con cualquier cosa. Me gustaría extender mi agradecimiento a todos los Villarribianos porque, a pesar del tiempo y la distancia, sé que puedo contar con vosotros para todo, ¡sois geniales!

A Gianni, por haber sido un gran tutor. Gracias por tu ayuda con el papeleo siempre que lo he necesitado y, sobre todo, gracias por contar conmigo durante todos estos años para dar las prácticas de laboratorio. Ha sido una magnífica experiencia de la que he aprendido y disfrutado muchísimo.

Gracias a mis compañeros del grupo EMP, a todos los que habéis pasado por aquí desde que se montó este laboratorio. A Alex, por acordarte de mí cuando Emilio buscaba candidatos para hacer el doctorado y por tu ayuda con todo durante este tiempo, esta etapa en IMDEA también te la debo a ti, gracias. A Alberto, por todo lo me has enseñado de tubos, junto con Alex y Sofía, y por tu ayuda con aquellos montajes ingenieriles. A Mar, por tu ayuda en mis primeros pasos con las porfirinas.

A Sofía, porque te debo media tesis. Gracias por ser una gran compañera, por lo que me has enseñado, por tu ayuda en todo momento, por tu apoyo en mis momentos de agobio y tu alegría en los buenos momentos. Sinceramente, gracias por haber compartido esta tesis conmigo. A Prabhash, thank you for teaching me to work in the clean room and for those first experiments in the fabrication of devices. A María, por tu alegría y apoyo durante el tiempo que pasaste con nosotros. A Emerson, por todo lo que he aprendido contigo y por tu gran ayuda siempre para encontrar soluciones. A Tere, gracias por tu alegría y por esas risas cuando subía al laboratorio de arriba. A Sofi Mena, por intentar ayudar siempre con todo y por esas buenas ideas para comprar regalos. A Belén, por tus cálculos y modelizaciones que nos han hecho un poquito más fácil nuestros proyectos. A Matías, gracias por tu ayuda en el labo y por tu esfuerzo para intentar que mis porfirinas funcionaran como catalizadores. A Juls, porque te debo la otra mitad de la tesis. Gracias por estar ahí día a día, por tu gran apoyo, por esas ideas que te hacen seguir para delante, por tus ánimos cuando las cosas no salen como te esperas y por todos esos buenos momentos en el labo y fuera de él. Gracias por esta etapa que hemos compartido juntas. A Mariano, porque, aunque muchas veces os he dicho '¡Estáis fatal!', has sido un gran compañero, gracias por tu ayuda en el labo durante todo este tiempo. A Enrique, gracias por lo que me has enseñado de Física y por todo tu esfuerzo para intentar encontrar una aplicación a mis moléculas, ¡ojalá salga algo interesante con nuestras porfirinas de cobalto! A Amalia, thank you for reaching this lab. Thanks for your help with everything, for your great support every day and because with you here, I have improved my English. Thank you very much for your love and for those encouragements that make me stay ahead. A Tomás, por tu simpatía, porque, aunque no nos ha dado tiempo a compartir mucho tiempo en el labo, siempre es agradable coincidir contigo cuando voy por allí. Por último, a nuestros técnicos, Javi, Zulay y Cristina, por haber estado y estar siempre dispuestos a ayudarnos con todo,

por tener los equipos a punto e intentar que todo funcione bien para que podamos trabajar día a día.

Porque mi tesis también ha estado marcada por un montón de colaboraciones, de las cuales he aprendido muchas cosas diferentes, quiero agradecer de manera especial a todas aquellas personas de otros grupos con las que he trabajado. Entre ellas, gracias a Andrés Castellanos y todo su grupo, Aday, Luis, Patricia y Riccardo, por el trabajo con los dispositivos de MoS_2 y los colorantes orgánicos. A David González y Raquel, por todos esos paseos a IMDEA y a la UAM para intentar entender la interacción entre vuestras moléculas y nuestros nanotubos, por todas las medidas y quebraderos de cabeza, gracias por este gran trabajo. A Dirk Guldi, Peter y Arjun, thanks for the photophysical characterization of the MINT-porphyrin samples. Gracias también a Dani Granados, Andrés Black, Fernando y Guillermo, por el trabajo de funcionalización de grafeno con porfirinas.

Por supuesto, no puedo olvidarme de mis compañeros de estancia. Tres meses únicos y maravillosos en Manchester que nunca olvidaré. First, thank you to Dave Leigh for giving me the opportunity to join his group. And then, of course, thanks to all the Leigh Group! Thank you all for being a big family, for your warm welcome, the wonderful atmosphere you have in the lab, your help with everything in and out the lab, the beers, Windermere… thanks for all those good moments and for that fantastic experience that made my stay super. Special thanks to the Spanish and Italian team, Vanesa, Jaramillo, Javi, Alberto, Albano and Simone, you are great!

También quería agradecer al resto de personas de IMDEA que me han ayudado durante todo este tiempo de una u otra manera. Gracias a Luis y David, por ser un apoyo especial durante esta tesis, por escucharme cada vez que os iba con uno de mis agobios, por intentar ayudarme con todo, por estar ahí siempre que lo he necesitado, por esos ánimos que no encuentro palabras para agradecer, y porque, aunque estéis en el laboratorio de al lado, me hacía sentirme acompañada, sobre

todo cuando se nos hacía tarde. Gracias chicos por ser grandes compañeros. A todos los que están y estuvieron en los laboratorios de Bea, Gorka, Nazario, Álvaro, y en general a todos los Químicos, Físicos, Biólogos… de este instituto, porque es genial tener compañeros como vosotros, porque así no te importa quedarte sin una botella de diclorometano, un rollo de papel, necesitar una micropipeta, o cualquier otra cosa que sin pensarlo puedas necesitar cualquier día. Gracias a todos por ayudarme siempre con una gran sonrisa. En especial, gracias a Fran, Ana y todos los del grupo de Ana Pizarro, por haber sido casi como parte de nuestro grupo. También quería agradecer a Jose Sánchez, Estefanía y Esther vuestra ayuda para intentar cristalizar mis porfis. Por supuesto, no puedo terminar esta parte de agradecimientos sin mencionar a Juancar, IMDEA no es lo mismo sin ti, gracias por alegrarme el día según entraba por la puerta cada mañana, por estar ahí las mil veces al día que te llamábamos para cualquier cosa que necesitábamos, por ayudarnos con todo, porque contigo no había dificultades para nada. A Roberto, por tu amabilidad y tu ayuda diaria. A Antonio, por cuidarnos tanto el instituto, por todas las veces que te hemos hecho subir para arreglar cualquier cosa o tirar disolventes y por estar siempre dispuesto a ayudarnos con una sonrisa. A Rodolfo, Jose Luis, Marije, Isabel, Juani, Elena, Paloma, Óscar por toda vuestra ayuda con cosas administrativas y papeleos. Gracias Marije por tu paciencia y ayuda con los informes de la FPU.

También quiero agradecer su trabajo a Santi, por su paciencia con el AFM hasta conseguir una buena imagen de mis muestras. Y, por supuesto, a Luisa, por su gran trabajo con el TEM, ¡al final sacamos una imagen estupenda! Gracias también al SIdI de la UAM, en especial a los laboratorios de RMN y Masas, por sus servicios para la caracterización de mis moléculas.

Por último, quiero dar las gracias a las personas más importantes en mi vida y para las cuales no creo que encuentre palabras de agradecimiento suficientes. Muchas gracias familia por estar siempre a mi lado. A mi padre, porque sé que te

hubiera encantado verme terminar la tesis, porque seguro que me hubieras dado un abrazo de esos tan apretados que me hubieras estrujado enterita, y porque sin tu ayuda no lo hubiera conseguido. A mi madre, por todo lo que has hecho por mí durante estos 29 años, porque no tengo palabras para poder agradecértelo. Por tu cariño y apoyo incondicional, por todo lo que me cuidas, por ayudarme siempre con todo, por encontrar siempre respuesta a mis dudas, por tu paciencia, tus ánimos, tus consejos, tus mimos y por hacer de mí una chica fuerte y valiente. Gracias mamá. A mi hermano, porque no podía haber tenido un hermano mejor, gracias por todo tu cariño, tu apoyo, tus ánimos, tu ayuda en todo momento y por esa gran alegría que nos transmites. A mis abuelos, Celes y Ana, porque nunca podré agradeceros todo lo que hacéis por nosotros, por vuestro cariño, vuestra ayuda, por todos esos caprichos que nos dais, y, sobre todo, por estar a nuestro lado por encima de todo. A mi tío Javi, por estar siempre ahí, por tus consejos y tu ayuda con todo. A mi tía Conchita, y los suyos, por todo lo que nos cuidáis y por vuestro apoyo incondicional. Y, por supuesto, a Álvaro. Son ya muchos años juntos y es difícil agradecerte con palabras todo lo que has hecho y haces por mí. Gracias por tu gran paciencia, sobre todo durante estos últimos años de tesis porque, aunque salga tardísimo del laboratorio, siempre me estás esperando con una gran sonrisa. Gracias por tu cariño, apoyo, ayuda, ánimo, y por todo lo que me cuidas y me aportas cada día. Gracias por estar siempre a mi lado y compartir tu vida conmigo. Me gustaría agradecer también a su familia el cariño recibido. Gracias por preocuparos tanto por mí. Por último, gracias a todos mis amigos por apoyarme durante todo este camino. Sin vosotros familia, no hubiera llegado hasta aquí, ¡Os Quiero!

Después de todos estos años de agobios y alegrías, llegan momentos especiales que te hacen recordar, sobre todo, lo que has disfrutado durante este tiempo.

Os echaré de menos. ¡Gracias!

Table of contents

Notes, references, abbreviations and acronyms

In this thesis only published work has been presented. Some projects and results have been left out.

Bibliographic citations have been placed as footnotes in the pages where they were first cited in the section; they were added independently at every section or chapter, so they are duplicated in different chapters when necessary.

Throughout this manuscript, abbreviations and acronyms recommended by the American Chemical Society in the Organic Chemistry area (updated in the *Journal of Organic Chemistry* on April **2018**; http://pubs.acs.org/paragonplus/submission/joceah/joceah_authguide.pdf) have been employed.

2D	two-dimensional
AC-HRTEM	aberration corrected-high resolution TEM
AFM	atomic force microscopy
C	cytidine
CCG	chemically converted graphene
CD	circular dichroism
CNT	carbon nanotube
D-A	donor-acceptor
DCM	dichloromethane
DDQ	2,3-dichloro-5,6-dicyano-1,4-benzoquinone
DFT	density functional theory
DMF	dimethylformamide

DMSO	dimethyl sulfoxide
DSSC	dye-sensitized solar cell
FAB	fast atom bombardment
FET	field-effect transistor
FTIR	Fourier-transform infrared
G	guanosine
GO	graphene oxide
HER	hydrogen-evolution reaction
HF	Hartree-Fock
IR	infrared
LED	light-emitting diode
MALDI	matrix-assisted laser desorption ionization
MIM	mechanically interlocked molecule
MINT	mechanically interlocked carbon nanotube
MOF	metal-organic framework
MS	mass spectrometry
MWCNT	multi-walled carbon nanotube
NMP	*N*-methyl pyrrolidone
NMR	nuclear magnetic resonance
OD	optical density
ODCB	*o*-dichlorobenzene
ORR	oxygen reduction reaction
PAMAM	polyamidoamine
Pc	phthalocyanine

PDI	perylenediimide
PDMS	poly(dimethylsiloxane)
PLE	photoluminescence excitation
por	porphyrin
PTFE	polytetrafluoroethylene
RBM	radial breathing modes
RCM	ring-closing metathesis
SDBS	sodium dodecylbenzene sulfonate
SDS	sodium dodecylsulfate
SWCNT	single-walled carbon nanotube
TBAF	tetrabutylammonium fluoride
TCE	tetrachloroethane
TEM	transmission electron microscopy
TFA	trifluoroacetic acid
TGA	thermogravimetric analysis
THF	tetrahydrofuran
TLC	thin-layer chromatography
TMDC	transition metal dichalcogenide
TPP	tetraphenyl porphyrin
UV	ultraviolet
vis	visible

ABSTRACT – RESUMEN

Abstract

In this work we present three main results:

- **The synthesis of rotaxane-type species composed of macrocyclic porphyrin rings mechanically interlocked with single-walled carbon nanotubes (SWCNTs) threads.** The mechanical bond was introduced as a new tool for chemical manipulation of carbon nanotubes, combining the advantages of both covalent and noncovalent methods. In the key rotaxane-forming step, we synthesize macrocycle precursors equipped with two porphyrins as recognition units for SWCNTs and terminated with bisalkenes that are closed around the nanotubes through ring-closing metathesis (RCM). Mechanically interlocked SWCNTs derivatives (MINTs) are widely characterized by analytical, spectroscopic and microscopic techniques, as well as by adequate control experiments. Individual macrocycles are observed by AC-HRTEM to circumscribe the nanotubes.

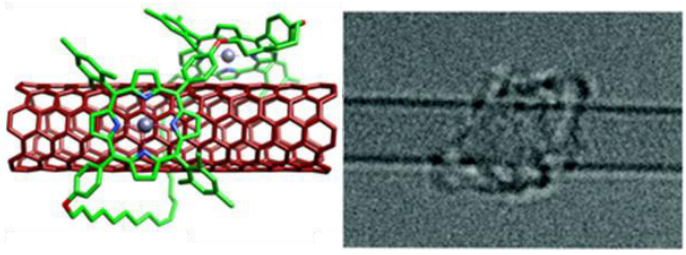

- **The reversible dispersion and release of carbon nanotubes *via* cooperative clamping interactions with hydrogen-bonded nanorings.** We describe a synergistic relationship established between (6,5)SWCNTs and a dinucleoside monomer that is able to self-assemble in nanorings *via* Watson-Crick base-pairing. We study by theoretical methodologies, spectroscopic and microscopic techniques that the H-bonded rings are able to associate with SWCNTs by embracing the tube sidewalls. This allows for an efficient SWCNT debundling

and for the production of long-lasting SWCNT dispersions. Also, nanoring stability is enhanced in the presence of SWCNTs, establishing multiple cooperative noncovalent interactions, which supplies on the other hand, the required reversibility to simply and effectively recover the pristine material.

- **The noncovalent functionalization of MoS_2-based photodetectors with molecular dyes.** By drop-casting a CH_2Cl_2 solution of PDI and TPP, we effectively functionalize MoS_2 devices improving their optoelectronic properties. The functionalization process is technologically trivial, air-stable, fully reversible and reproducible. We study it by different electronic and optoelectronic techniques, observing a dramatic enhancement of the photoresponse by about four orders of magnitude, and responsivities up to 100 A W^{-1}.

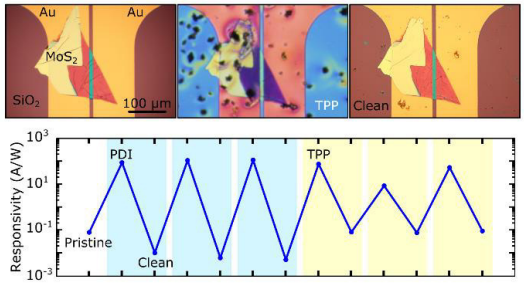

Resumen

En este trabajo se presentan tres resultados principales:

- **La síntesis de estructuras de tipo rotaxano compuestas por macrociclos de porfirina enlazados mecánicamente con nanotubos de carbono de pared sencilla (SWCNTs).** El enlace mecánico se introdujo como una nueva herramienta para la manipulación química de nanotubos de carbono, combinando las ventajas de los métodos covalente y no covalente. Para la formación del rotaxano, sintetizamos precursores macrocíclicos formados por dos unidades de porfirina que actúan como motivos de reconocimiento para los nanotubos de carbono, y se encuentran funcionalizadas por dos cadenas alquílicas con dobles enlaces terminales que se cierran alrededor de los nanotubos mediante una reacción de metátesis de cierre de anillo. Los derivados de SWCNTs enlazados mecánicamente (MINTs) se caracterizan en detalle mediante técnicas analíticas, espectroscópicas y microscópicas, así como los experimentos control correspondientes. Por microscopía electrónica de alta resolución podemos observar macrociclos individuales rodeando SWCNTs.

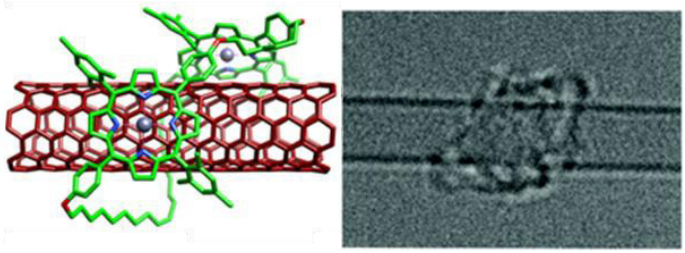

- **La dispersión reversible y la liberación de nanotubos de carbono mediante interacciones cooperativas con macrociclos formados mediante enlaces de hidrógeno.** Se describe una relación sinérgica establecida entre (6,5)SWCNTs y un monómero que presenta dos bases nitrogenadas capaz de auto-ensamblarse en macrociclos a través del apareamiento Watson-Crick de las nucleobases.

Mediante técnicas teóricas, espectroscópicas y microscópicas estudiamos cómo los macrociclos formados por enlaces de hidrógeno pueden asociar SWCNTs colocándose alrededor de los mismos. Esta asociación permite la ruptura de los agregados de nanotubos y la formación de dispersiones de SWCNTs de larga duración. Además, la estabilidad del macrociclo también mejora en presencia de los nanotubos, estableciéndose interacciones cooperativas no covalentes. Estas interacciones proporcionan, por otro lado, la reversibilidad necesaria para recuperar de manera simple y efectiva el material prístino.

- **La funcionalización no covalente de fotodetectores de MoS_2 con colorantes moleculares.** Mediante un método sencillo basado en 'drop-casting' y utilizando disoluciones de PDI y TPP, conseguimos funcionalizar dispositivos de MoS_2 de manera eficaz mejorando sus propiedades optoelectrónicas. El proceso de funcionalización es tecnológicamente trivial, estable al aire, reversible y reproducible, y estudiándolo mediante diversas técnicas electrónicas y optoelectrónicas, observamos un excelente aumento de la fotorrespuesta de cuatro órdenes de magnitud, y responsividades de hasta 100 A W^{-1}.

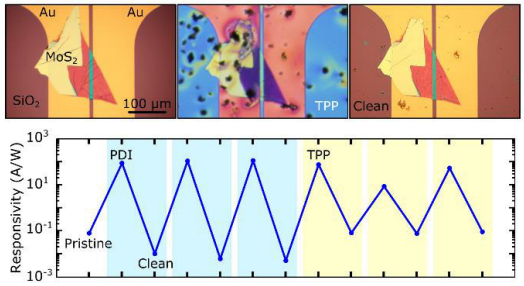

1. INTRODUCTION

1. Introduction

1.1. Porphyrins

During the past decade, porphyrin and its derivatives have been widely studied.[1] In this work, I will describe the chemistry and the physical and chemical properties of porphyrins and provide examples of their applications in several fields.

1.1.1. Chemistry

Porphyrins are heterocyclic macrocycles derived from four pyrrolic units linked by methine bridges at their α-positions. They are highly conjugated aromatic rings with 22π electrons delocalized over the macrocycle.

Porphyrins can coordinate hydrogen or metal cations in their centre through the four isoindole nitrogen atoms. A great variety of metalloporphyrins are known; almost every metal can be coordinated inside the macrocycle, different oxidation states are possible and further coordination can happen at the axial positions, in case there are free coordination sites.

The unsubstituted porphyrin has been named *porphine*. The two most frequently encountered substitution patterns are provided by β-octaalkylporphyrins and *meso*-tetraarylporphyrins. Naturally occurring porphyrins are β-substituted in an unsymmetrical fashion (Figure 1).

[1] T. Q. Nguyen, M. C. S. Escano, H. Kasai, *Handbook of Porphyrins: Chemistry, Properties and Applications* **2012**, 229-260.

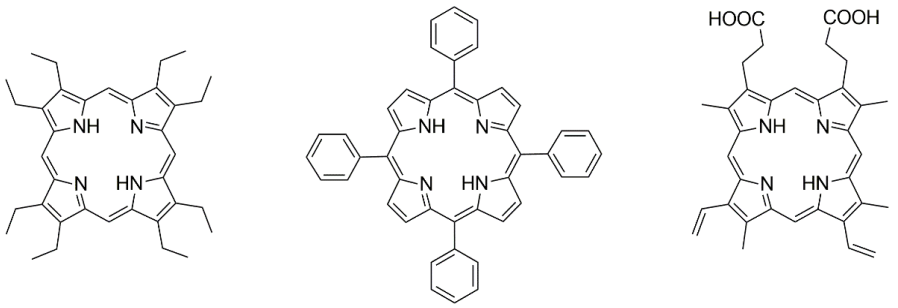

Figure 1. Favourite substitution patterns: β-octaethylporphyrin (left), *meso*-tetraphenylporphyrin (centre), protoporphyrin IX (right).

The unique light absorption properties of porphyrinoids and the ability of the ring to bind metals makes them a frequently observed structure in Nature. Three well-known natural porphyrin-like molecules are shown in Figure 2: the cobalt containing cobyrinic amide, the central component of vitamin B_{12}, plays a key role in cellular metabolism;[2] the iron-containing heme, found in hemoglobin, is responsible for the binding and transportation of oxygen within blood cells;[3] finally, chlorophyll, a magnesium-metallated porphyrinoid chromophore, acts as the light-harvesting agent in photosynthetic organisms.[4]

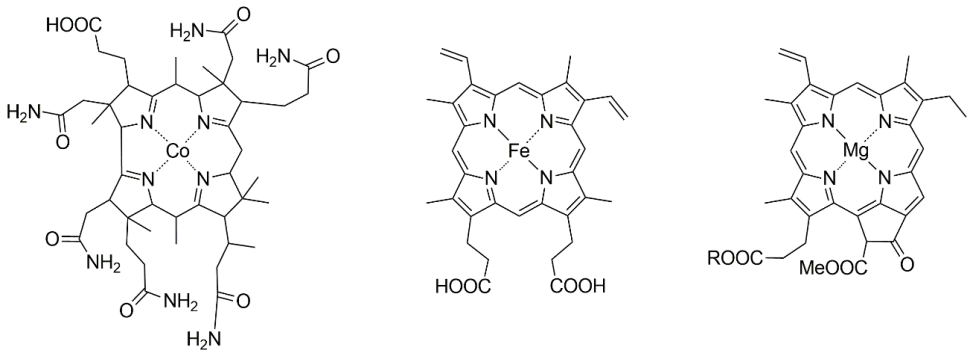

Figure 2. Natural porphyrin-like molecules: cobyrinic amide (left), heme (centre) and chlorophyll (right).

[2] F. J. Widner, F. Gstrein, B. Krautler, *Helv. Chim. Acta* **2017**, *100*, e1700170.
[3] L. Zhang, *Heme Biology* **2011**, 1-6.
[4] H. Tamiaki, *Coord. Chem. Rev.* **1996**, *148*, 183-197.

1.1.2. Properties and applications

Porphyrins have an aromatic character,[5,6] which is reflected in the planarity of the porphyrin core and which differs between free-base and metallated porphyrins (Figure 3).[7] In the free-base, it involves 18 of the 22π electrons leaving two localized double bonds on two opposing pyrroles; this, combined with the tautomerism, makes the pyrrole rings less aromatic than the 'internal cross' represented by the porphyrin without β-pyrrolic carbons. In metalloporphyrins, instead, all electrons are delocalized all over the porphyrin ring.

Figure 3. Aromaticity in free-base (left) and metallated (right) porphyrins.

Aromaticity is probably the most important reason for which porphyrins have been utilized by Nature in a wide range of processes; the possibility to delocalize electrons over such a large system gives porphyrins a good thermal stability and the ability to be oxidized and reduced with little destabilization of the overall system. Moreover, substituents and coordinated metals can have a strong effect on the electronic system, allowing chemical and physical properties to be finely tuned.

Porphyrins are also one of the strongest light absorbing materials in Nature, to the point that they are often called "pigments of life". The presence of highly conjugated π-electronic systems is responsible for the very high molar extinction

[5] T. M. Krygowski, M. K. Cyrański, *Phys. Chem. Chem. Phys.* **2004**, *6*, 249-255.
[6] P. Lazzeretti, *Phys. Chem. Chem. Phys.* **2004**, *6*, 217-223.
[7] M. K. Cyrański, T. M. Krygowski, M. Wisiorowski, N. J. R. van Eikema Hommes, P. von Ragué Schleyer, *Angew. Chem. Int. Ed.* **1998**, *37*, 177-180.

coefficient for the π-π* transitions in the near-UV/visible part of the electromagnetic spectrum. All porphyrins and metalloporphyrins show a very strong ($\varepsilon > 200{,}000$ L mol^{-1} cm^{-1}) Soret (or B) band at around 400 nm and weaker ($\varepsilon < 30{,}000$ L mol^{-1} cm^{-1}) Q bands in the 500-700 nm region. The excited states produced by these transitions are usually characterized by long lifetimes and often relax to the ground state radiatively, by fluorescence.

As a result of those physical and chemical properties, natural porphyrins play critical roles in biological activities like redox processes,[8,9] oxygen transport and light harvesting.[10,11] Porphyrin chemistry has been intensively investigated over the last 50 years and synthetic porphyrins have been introduced into a variety of interesting applications such as in catalysis,[12] medicine[13,14,15] and optical devices.[16,17]

1.2. Carbon nanotubes and porphyrins

Carbon nanotubes (CNTs) are an allotrope form of carbon, like diamond, graphite, graphene and fullerene. CNTs are tubular in shape and they are made of rolled-up graphene sheets. According to the number of carbon layers, CNTs are classified in multi-walled carbon nanotubes (MWCNTs) and single-walled carbon nanotubes (SWCNTs). MWCNTs were discovered in 1991 by Iijima in the carbon soot of graphite electrodes during an arc-discharge intended to produce fullerenes.[18]

[8] G. Pratviel, *Coord. Chem. Rev.* **2016**, *308*, 460-477.
[9] M. Trytek, M. Majdan, J. Fiedurek, *Biomimetic Based Applications* **2011**, 59-104.
[10] P. Fromme, A. Melkozernov, P. Jordan, N. Krauss, *FEBS Lett.* **2003**, *555*, 40-44.
[11] L.-L. Li, E. W.-G. Diau, *Chem. Soc. Rev.* **2013**, *42*, 291-304.
[12] W.-B. Sheng, Q. Jiang, W.-P. Luo, C.-C. Guo, *J. Org. Chem.* **2013**, *78*, 5691-5693.
[13] H. Sheng, I. Spasojevic, D. S. Warner, I. Batinic-Haberle, *Neurosci. Lett.* **2004**, *366*, 220-225.
[14] S. S. Stylli, M. Howes, L. MacGregor, P. Rajendra, A. H. Kaye, *J. Clinical Neurosci*. **2004**, *11*, 584-596.
[15] M. Ethirajan, Y. Chen, P. Joshi, R. K. Pandey, *Chem. Soc. Rev.* **2011**, *40*, 340-362.
[16] R. K. Lammi, A. Ambroise, R. W. Wagner, J. R. Diers, D. F. Bocian, D. Holten, J. S. Lindsey, *Chem. Phys. Lett.* **2001**, *341*, 35-44.
[17] D. Kim, A. Osuka, *J. Phys. Chem. A* **2003**, *107*, 8791-8816.
[18] S. Iijima, *Nature* **1991**, *354*, 56-58.

Two years later, SWCNTs were described; whereas the MWCNTs were formed on the carbon cathode, these SWCNTs grew in the gas phase.[19]

The structure of carbon nanotubes has been extensively reviewed.[20,21] SWCNTs can be separated in three types depending on how the graphene layer is rolled up. The structure is defined by a roll-up vector $\boldsymbol{C}_h$ given by two unit vectors $\boldsymbol{a}_1$ and $\boldsymbol{a}_2$: $\boldsymbol{C}_h = n\boldsymbol{a}_1 + m\boldsymbol{a}_2$, where n and m are integers and designated as the roll-up index (n, m), as shown in Figure 4.[22]

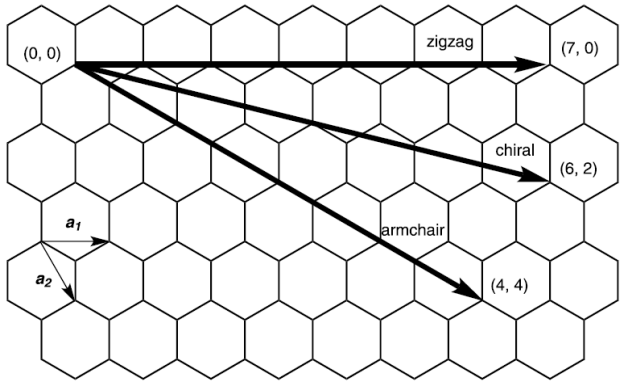

Figure 4. (n, m) SWCNT defined by rolling up the graphene along the roll-up vector $\boldsymbol{C}_h$.

Depending on the alignment of the hexagonal rings along the tube axis, three types of SWCNTs can be formed: when $m = n$, the nanotube is called *armchair*, when $m = 0$, the nanotube is called *zigzag*, and *chiral* nanotubes include all other configurations (Figure 5).

[19] S. Iijima, T. Ichihashi, *Nature* **1993**, *363*, 603-605.
[20] M. Terrones, *Annu. Rev. Mater. Res.* **2003**, *33*, 419-501.
[21] M. Zhang, J. Li, *Mater. Today* **2009**, *12*, 12-18.
[22] N. Komatsu, *Top Heterocycl Chem* **2008**, *17*, 161-198.

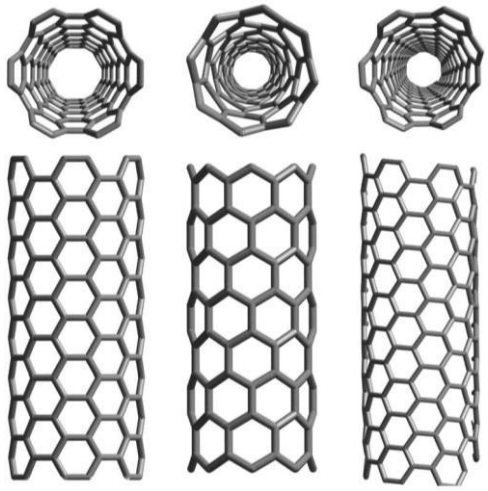

Figure 5. Armchair (left), zigzag (centre) and chiral (right) structures of SWCNTs.

Carbon nanotubes have unique electronic and mechanical properties. SWCNTs are one-dimensional nanowires that can be metallic or semiconducting. They can accept both electrons and holes, which can be transported under nearly resistance-free conditions along the axis.[23] Their electrical conductivity, morphology and good chemical stability make SWCNTs extraordinary and promising building blocks for nanotechnology, suitable to be used in a wide range of applications,[24] including polymer composites,[25] energy conversion,[26] catalysis,[27] and biological applications.[28]

[23] A. Javey, J. Guo, Q. Wang, M. Lundstrom, H. Dai, *Nature* **2003**, *424*, 654-657.
[24] J. M. Schnorr, T. M. Swager, *Chem. Mater.* **2011**, *23*, 646-657.
[25] P. J. F. Harris, *Int. Mater. Rev.* **2004**, *49*, 31-43.
[26] (a) H. Wang, G. I. Koleilat, P. Liu, G. Jiménez-Osés, Y.-C. Lai, M. Vosgueritchian, Y. Fang, S. Park, K. N. Houk, Z. Bao, *ACS Nano* **2014**, *8*, 2609-2617; (b) D. M. Guldi, G. M. A. Rahman, V. Sgobba, N. A. Kotov, D. Bonifazi, M. Prato, *J. Am. Chem. Soc.* **2006**, *128*, 2315-2323; (c) S. Bhattacharyya, E. Kymakis, G. A. J. Amaratunga, *Chem. Mater.* **2004**, *16*, 4819-4823.
[27] (a) A. Le Goff, V. Artero, B. Jousselme, P. D. Tran, N. Guillet, R. Métayé, A. Fihri, S. Palacin, M. Fontecave, *Science* **2009**, *326*, 1384-1387; (b) X. Tan, W. Deng, M. Liu, Q. Zhang, Y. Wang, *Chem. Commun.* **2009**, 7179-7181; (c) V. Lordi, N. Yao, J. Wei, *Chem. Mater.* **2001**, *13*, 733-737.
[28] (a) M. Adeli, R. Soleyman, Z. Beiranvanda, F. Madania, *Chem. Soc. Rev.* **2013**, *42*, 5231-5256; (b) G. Cellot, E. Cilia, S. Cipollone, V. Rancic, A. Sucapane, S. Giordani, L. Gambazzi, H. Markram, M. Grandolfo, D. Scaini, F. Gelain, L. Casalis, M. Prato, M. Giugliano, L. Ballerini, *Nat Nano* **2009**, *4*, 126-133; (c) W. Wu, S. Wieckowski, G. Pastorin, M. Benincasa, C. Klumpp, J. P. Briand, R. Gennaro, M. Prato, A. Bianco, *Angew. Chem. Int. Ed.* **2005**, *44*, 6358-6362.

Nevertheless, although pristine SWCNTs can be used in many applications, a major drawback is that they tend to agglomerate into ropes or bundles due to strong van der Waals forces and, consequently, these cohesive forces lead to poor solubility in most common solvents, making chemical manipulation difficult and their use in practical applications challenging. For this reason, in order to improve their solubility, purify them and/or to modulate their properties, the chemical modification of SWCNTs represents an important area into these materials.

The methods for the functionalization of SWCNTs can be divided into two broad categories: covalent, and non-covalent or supramolecular approaches. Covalent functionalization involves binding molecular fragments saturating some of the sp^2 carbons of the nanotube wall, producing an array of modified nanotube structures bearing small molecules or polymers.[29] However, this strategy modifies the conjugated π-system of the SWCNTs, which necessarily changes their electronic and structural properties.

The non-covalent approach involves physisorption of molecules capable of establishing π-stacking or van der Waals interactions with the nanotube wall. This procedure does not introduce perturbations in graphitic structure of the nanotube, so that the electronic structure of the SWCNTs can be maintained.[30] However, because of the very nature of this type of functionalization, involving weak reversible forces, the attachment and detachment of the adsorbed molecules takes place continuously, under equilibrium.

In order to functionalize SWCNTs and modify their solubility and electronic properties, a large number of different species have been used. One of the directions that we have considered in our research is the using of porphyrins to obtain carbon nanotubes derivatives through either covalent or non-covalent links.

[29] (a) D. Tasis, N. Tagmatarchis, A. Bianco, M. Prato, *Chem. Rev.* **2006**, *106*, 1105-1136; (b) A. Hirsch, *Angew. Chem. Int. Ed.* **2002**, *41*, 1853-1859.

[30] (a) P. Bilalis, D. Katsigiannopoulos, A. Avgeropoulos, G. Sakellariou, *RSC Adv.* **2014**, *4*, 2911-2934; (b) A. Di Crescenzo, V. Ettorre, A. Fontana*, Beilstein J. Nanotechnol.* **2014**, *5*, 1675-1690.

Taking into account the unique photophysical and electrochemical properties of porphyrins, and the extraordinary properties of SWCNTs, hybrids of porphyrins with SWCNTs have been extensively investigated.

1.2.1. Covalent SWCNT-porphyrin hybrids

The covalent approach can roughly be subdivided into two categories: the use of the nanotube-bound carboxylic acids arising from defects created by the shortening of nanotubes upon oxidation and the direct attachment of functional groups onto the nanotube sidewall.[31,32] Both categories may have different effects on the structure and intrinsic properties of carbon nanotubes.

1.2.1.1. Functionalization of SWCNTs using carboxyl groups

An approach to the covalent functionalization of SWCNTs involves the reaction of SWCNTs with strong acids, usually mixtures of concentrated sulfuric and nitric acids.[33] This oxidizing treatment yields shortened, uncapped SWCNTs bearing oxygen-containing groups, such as carboxylates, at the open ends and defective sites of the sidewalls. The carboxyl groups can be readily derivatized to acid chlorides and subsequently coupled to alcohols or amines to form esters or amides, respectively.

Using this strategy, the covalent linking of porphyrins to SWCNTs was achieved by esterification/amidation of hydroxyl/amino groups appended porphyrins with the oxidized SWCNT. One of the first covalent connections between SWCNTs and porphyrins was described by Sun et al. in 2004,[34] where two different porphyrins bearing hydroxyl groups connected with long and short alkyl linkages are

[31] T. Umeyama, H. Imahori, *J. Phys. Chem. C* **2013**, *117*, 3195-3209.
[32] F. Langa, M. J. Gómez-Escalonilla, P. de la Cruz, *J. Porphyrins Phthalocyanines* **2007**, *11*, 348-358.
[33] J. Liu, A. G. Rinzler, H. Dai, J. H. Hafner, R. K. Bradley, P. J. Boul, A. Lu, T. Iverson, K. Shelimov, C. B. Huffman, F. Rodriguez-Macias, Y.-S. Shon, T. R. Lee, D. T. Colbert, R. E. Smalley, *Science* **1998**, *280*, 1253-1256.
[34] H. P. Li, R. B. Martin, B. A. Harruff, R. A. Carino, L. F. Allard, Y. P. Sun, *Adv. Mater.* **2004**, *16*, 896-900.

covalently appended to SWCNTs though esterification (Figure 6). Both porphyrin derivatives are soluble in non-polar solvents, which allowed the characterization of these materials by spectroscopic techniques such as ^{1}H NMR, FTIR and Raman spectroscopy. Analyzing these samples by transmission electron microscopy (TEM) individual SWCNTs were found at high resolution, with soft material attached (attributed to the porphyrin moiety) that could be removed by thermal treatment at 370 °C for 30 min. The absorption spectra of both structures suggest no significant interactions between the porphyrin and the nanotube in the ground state, and the fluorescence intensity of the composite was decreased by ~30% compared to the corresponding porphyrin, which was attributed to photoinduced energy transfer from the free-base porphyrin excited single state to the SWCNT framework.

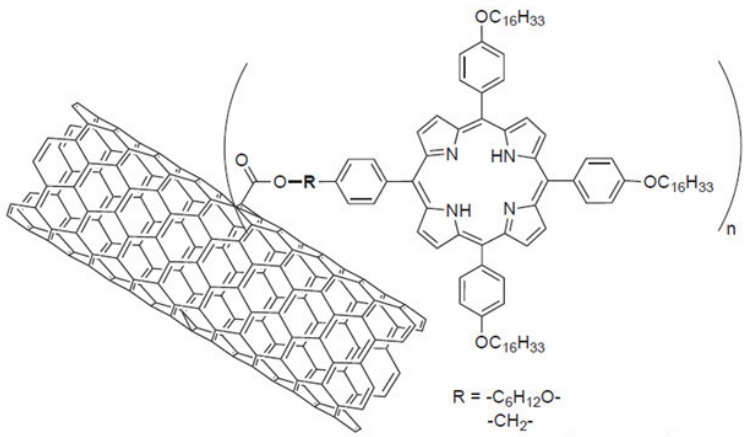

Figure 6. Structure of porphyrin-decorated SWCNTs.

Baskaran et al. later described the functionalization of SWCNTs with 5-*p*-hydroxyphenyl-10,15,20-tritolyl-porphyrin through an ester bond.[35] In this case, the fluorescence of the porphyrin moieties was quenched by 95-100% with respect to the porphyrin precursor, a finding that supports the existence of an electron transfer

[35] D. Baskaran, J. W. Mays, X. P. Zhang, M. S. Bratcher, *J. Am. Chem. Soc.* **2005**, *127*, 6916-6917.

process from the singlet excited state of the porphyrin to the SWCNT, which was proven to be an efficient electron acceptor.

Few years ago, a ferrocene-porphyrin-SWCNT triad (Figure 7) was prepared by amidation reaction between oxidized SWCNT and aminoporphyrin bearing an appended ferrocenyl substituent.[36] The steady-state emission characteristics revealed the existence of the effective photoinduced electron transfer among ferrocene, excited porphyrin moiety and SWCNT, which was further confirmed by the results of time-resolved transient absorption spectra. The final lifetime of charge-separation state was observed to be increased compared to the reference nanohybrid porphyrin-SWCNT. Therefore, the ferrocene-porphyrin-SWCNT triad constructed is expected to be applicable to photoelectrochemical devices exhibiting efficient photocurrent generation.

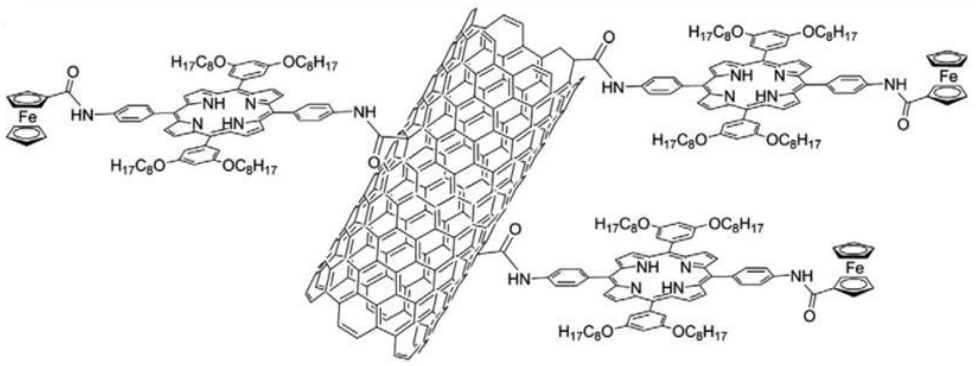

Figure 7. Structure of ferrocene-porphyrin-SWCNT triad hybrid.

[36] H. Zhao, Y. Zhu, C. Chen, L. He, J. Zheng, *Carbon* **2012**, *50*, 4894-4902.

1.2.1.2. Direct addition of porphyrin onto the SWCNT sidewall

Direct attachment of photoactive molecules onto the sidewalls of SWCNTs can provide photoactive molecule-SWCNT composites with robust and well-defined structures, in comparison with the functionalization with carboxylates introduced at the terminals and defective sites of the SWCNT by the acid treatments. Therefore, such covalently sidewall-functionalized SWCNTs by porphyrins are attractive for a better understanding of the interactions between the two components in the ground and excited states.

Direct addition reactions to the SWCNT sidewall using azomethine ylides[37] and aryl diazonium compounds[38] are widely used and of particular importance as a convenient method for attachment of functional groups. Guo et al. reported a covalently linked porphyrin-functionalized SWCNT,[39] prepared using diazonium compounds, that incorporates porphyrins directly linked onto the wall of SWCNT, with a direct linkage mode between the two moieties. As it is shown in Scheme 1, this material was synthesized by the reaction of the porphyrin TPP-NH_2 with SWCNT using the corresponding porphyrin diazonium compound, generated *in situ* by oxidation of the amino group of porphyrin with isoamyl nitrite.

In this resulting nanohybrid, the fluorescence of the photoexcited porphyrin was quenched through intramolecular electron transfer process, indicating that the direct linkage mode facilitated the effective energy and electron transfer between the excited porphyrin moiety and the extended π-system of SWCNTs. More significantly, these covalently modified SWCNTs show superior optical limiting properties, and are promising candidates for optoelectronic devices, such as optical limiting and solar-energy conversion applications.

---

[37] V. Georgakilas, K. Kordatos, M. Prato, D. M. Guldi, M. Holzinger, A. Hirsch, *J. Am. Chem. Soc.* **2002**, *124*, 760-761.
[38] J. L. Bahr, J. Yang, D. V. Kosynkin, M. J. Bronikowski, R. E. Smalley, J. M. Tour, *J. Am. Chem. Soc.* **2001**, *123*, 6536-6542.
[39] Z. Guo, F. Du, D. Ren, Y. Chen, J. Zheng, Z. Liu, J. Tian, *J. Mater. Chem.* **2006**, *16*, 3021-3030.

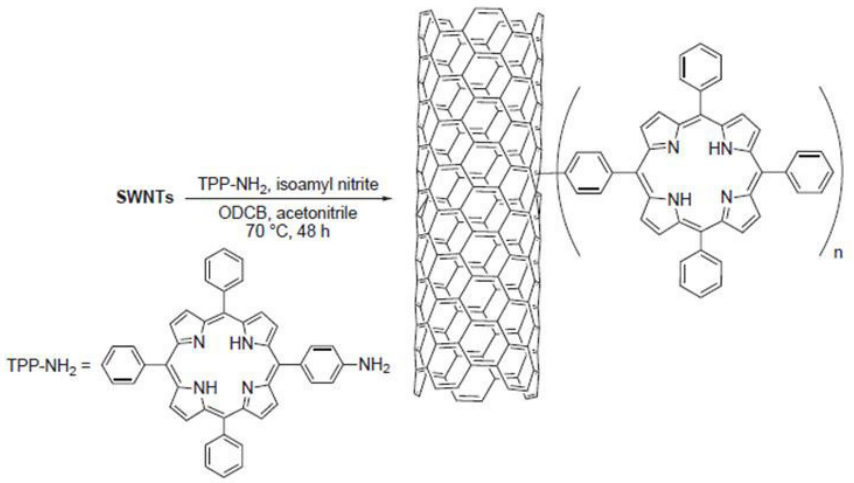

Scheme 1. Synthesis of the SWCNT-TPP composite.

Two-step functionalization procedures, i.e., the preparation of a prefunctionalized SWCNTs by 1,3-dipolar cycloaddition of azomethine ylides or aryl addition of diazonium compounds and subsequent amidation or click reactions,[40] were also utilized to prepare SWCNT-porphyrin linked systems. Arai et al. prepared SWCNT tethering zinc porphyrins with an ethylene spacer (ZnP-E-SWCNT, Figure 8) by the two-step method to investigate photophysical and photovoltaic properties of ZnP-E-SWCNT.[41]

Studying the ZnP-E-SWCNT composite under illumination by visible light and in the presence of a sacrificial electron donor, they observed that this material effectively catalyzed the reduction of the benzylviologen dication and also the H_2 evolution in the presence of Pt particles in aqueous solution. Furthermore, the photocurrent and photovoltage were observed to respond to the on-off cycles of the visible light irradiation in a solar cell consisting of a transparent glass electrode modified with ZnP-E-SWCNT; the photocurrent action spectrum showed that the

[40] T. Palacin, H. L. Khanh, B. Jousselme, P. Jegou, A. Filoramo, C. Ehli, D. M. Guldi, S. Campidelli, *J. Am. Chem. Soc.* **2009**, *131*, 15394-15402.
[41] T. Arai, S. Nobukuni, A. S. D. Sandanayaka, O. Ito, *J. Phys. Chem. C* **2009**, *113*, 14493-14499.

ZnP unit was responsible for the photochemical events; i.e., the photoexcitement of ZnP may induced charge separation with SWCNT forming $ZnP^{\bullet+}$-E-$SWCNT^{\bullet-}$, followed by the subsequent electron transfer to the substrate.

These experiments suggest that the covalently bonded ZnP tethering the SWCNT provides the favorable orientation, resulting in the efficient intramolecular charge separation and subsequent intermolecular electron transfer.

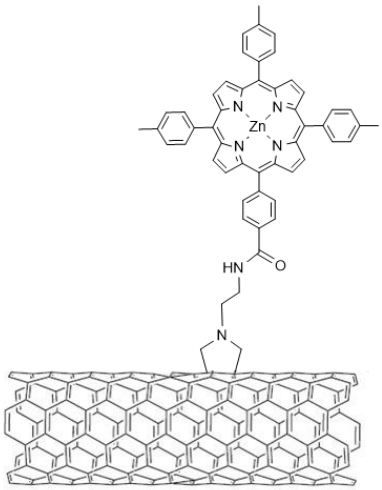

Figure 8. Structure of ZnP-E-SWCNT.

As indicated above, the covalent functionalization of the wall of SWCNTs causes a change in the conjugated π-system and this affects their electronic and optical properties. However, it has been shown that a weak functionalization can improve the processability of SWCNT derivatives while keeping their conjugated π-systems almost intact. Polymers and dendrimers allow a limited number of functional groups to be attached to the SWCNT surface. In this context, Prato et al. described the construction of polyamidoamine (PAMAM) dendrimers using the nanotubes as a central core (Figure 9).[42]

[42] S. Campidelli, C. Sooambar, E. Lozano, C. Ehli, D. M. Guldi, M. Prato, *J. Am. Chem. Soc.* **2006**, *128*, 12544-12552.

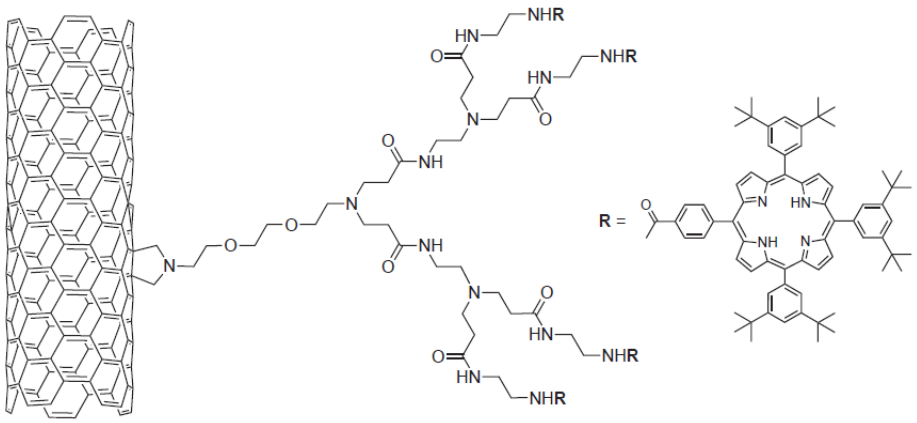

Figure 9. Structure of PAMAM dendrimer-functionalized SWCNT.

These functionalized SWCNTs presented a second generation of polyamidoamine dendrimers, built directly onto the nanotube surface using a divergent methodology, whose amino terminal groups had been functionalized with tetraphenylporphyrins. This approach allows the number of functional groups on the nanotubes to be increased without provoking significant damage to the conjugated π-system of the SWCNTs.

The photophysical properties of the resulting nanoconjugates were investigated by steady state and time-resolved spectroscopy, and this showed fast charge separations from the photoexcited porphyrin chromophores. Most importantly, the oxidized porphyrin chromophore was identified through its fingerprint absorption in the 550-800 nm range, while the signature of reduced SWCNTs appears in the 850-1400 nm range.

They demonstrated that dendrimers permit an increase of photoactive groups on the surface of the nanotubes. These dendrimers with their porphyrins play conceptually the role of an antenna: harvesting light to give more efficient electron transfers.

1.2.2. Non-covalent SWCNT-porphyrin hybrids

Porphyrins are functional dyes that have been shown to strongly interact with the π-electronic surface of graphite.[43] Carbon nanotubes contain, in a similar way to graphite, highly delocalized π-electrons. Therefore, the surface of nanotubes is easily functionalized through π-π interactions with compounds that possess π-electron-rich structures. In this way, the combination of porphyrins and SWCNTs[22,32] has drawn special attention as these flat, planar aromatic structures are ideal for π-stacking interactions with the conjugated sidewalls of SWCNTs, showing unique photophysical and electrochemical properties.

One of the first non-covalent SWCNT-porphyrin conjugates was reported by Nakashima et al.[44] SWCNTs were insoluble in DMF, but a reddish-black colored transparent solution was obtained in a Zn-porphyrin solution in DMF, without further precipitation being observed even after two months.

Soon after the report, solvation of SWCNTs in a selective manner was reported by Sun et al. using a free-base porphyrin monomer.[45] Non-covalent interactions of SWCNTs with the 5,10,15,20-tetrakis(hexadecyloxyphenyl)porphyrin (THPP) resulted in the enrichment of semiconducting SWCNTs in the solubilized sample and metallic SWCNTs in the residual sample, while the use of Zn-THPP under the same experimental conditions, did not lead to any solubilizing interactions. Removal of the excess porphyrin from the solution resulted in the recovery of insoluble SWCNTs, indicating that the SWCNT-porphyrin complex could be easily dissociated.

A dynamic coordinative-directed solubilization of SWCNTs in aqueous solutions has been achieved by Stoddart et al.[46] through a combination of a Zn^{II}

[43] T. Sagara, M. Fukuda, N. Nakashima, *J. Phys. Chem. B.* **1998**, *102*, 521-527.
[44] H. Murakami, T. Nomura, N. Nakashima, *Chem. Phys. Lett.* **2003**, *378*, 481-485.
[45] H. Li, B. Zhou, Y. Lin, L. Gu, W. Wang, K. A. S. Fernando, S. Kumar, L. F. Allard, Y.-P. Sun, *J. Am. Chem. Soc.* **2004**, *126*, 1014-1015.
[46] K. S. Chichak, A. Star, M. Virginia, P. Altoé, J. F. Stoddart, *Small* **2005**, *1*, 452-461.

metalloporphyrin complex and a *cis*-protected Pd^{II} complex, which are believed to form charged acyclic and/or cyclic adducts on or around the sidewalls of the SWCNTs. The solubilization of SWCNTs in aqueous solution only occurs when these acyclic and/or cyclic complexes are allowed to enter simultaneously into a self-assembly process with SWCNTs under mild conditions.

Protonated porphyrins provide a convenient way to construct ordered molecular assemblies. Kamat et al. reported SWCNT-driven aggregation of a protonated porphyrin (5,15-bis(3,5-di-*tert*-butylphenyl)porphyrin, Figure 10) to produce supramolecular assemblies in the form of macroscopic bundles.[47] The π-π interaction between porphyrins and SWCNTs plays an important role in influencing the orientation of protonated porphyrins, inducing *J*- and *H*-type aggregation effects on the SWCNT surface, as shown in Figure 10. These aggregation effects played an important role in constructing not only ordered supramolecular assembly at the molecular level, but also large rod-like structures at the microscopic level.

The supramolecular assemblies of the protonated form of this porphyrin and SWCNTs were found to undergo photoexcited intramolecular electron transfer. This photochemical behaviour in the supramolecular assemblies was applied to solar cells systems, giving ~13% of the incident photon to photocurrent efficiency at an applied potential of 0.2 V versus saturated calomel electrode.[48]

[47] T. Hasobe, S. Fukuzumi. P. V. Kamat, *J. Am. Chem. Soc.* **2005**, *127*, 11884-11885.
[48] T. Hasobe, S. Fukuzumi. P. V. Kamat, *J. Phys. Chem. B* **2006**, *110*, 25477-25484.

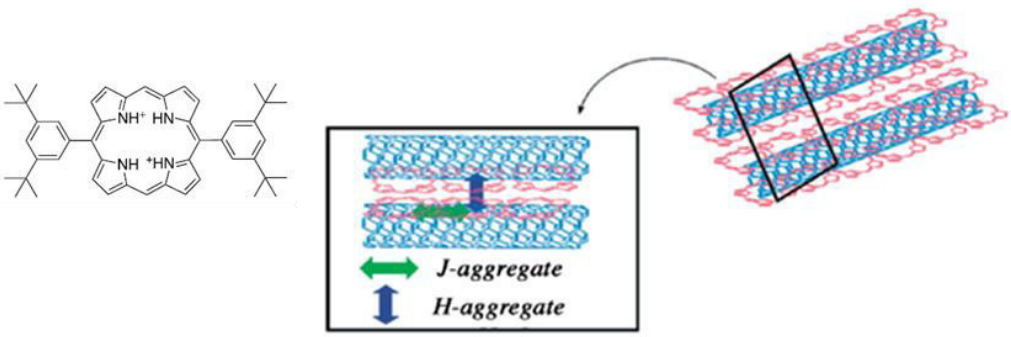

Figure 10. Protonated form of 5,15-bis(3,5-di-*tert*-butylphenyl)porphyrin and an illustration of supramolecular assembly between porphyrins and SWCNTs.

Water-soluble porphyrin molecules, like *meso*-(tetrakis-4-sulfonatophenyl)porphine dihydrochloride, have been employed to solubilize SWCNTs in aqueous solutions, which are stable for several weeks.[49] The SWCNT-porphyrin interaction is selective for the free base form, and this interaction stabilizes the free base against protonation to the diacid. In this case, under mildly acidic conditions the nanotube-mediated aggregate form is unstable in solution and results in precipitation of the nanotubes over the course of a few days. Porphyrin-coated SWCNTs can be precisely aligned on hydrophilic poly(dimethylsiloxane) (PDMS) surfaces by combing SWCNT solution along a desired direction and then transferring it onto silicon substrates by stamping. Parallel SWCNT patterns have been fabricated in this manner.

With the aim of searching novel electron donor-acceptor nanohybrid structures, several groups have studied the immobilization of porphyrins onto the SWCNT surface.[50] In a more elaborate example, the groups of Prato and Guldi studied the systematic immobilization of an octasodium salt of a zinc porphyrin derivative as oligo-anionic chromophores/electron donors onto electron-accepting

[49] J. Chen, C. P. Collier, *J. Phys. Chem. B* **2005**, *109*, 7605-7609.
[50] G. M. A. Rahman, D. M. Guldi, S. Campidelli, M. Prato, *J. Mater. Chem.* **2006**, *16*, 62-65.

SWCNTs (Scheme 2).[51] Van der Waals interactions have been used to favour intermolecular recognition between the SWCNT and the pyrene ammonium cation. The anionic porphyrin was immobilized on the dyad through electrostatic interactions, providing the nanohybrid SWCNT/pyrene^{+}/ZnP^{8-}.

The photophysical and electrochemical studies revealed that electron-transfer from the photoexcited porphyrin (ZnP^{8-}) to SWCNT occurred to create long-lived radical ion pairs.[52,53] The lifetimes of the charge-separated states are sufficiently long that these systems appear as excellent candidates for the fabrication of photovoltaic devices for solar-energy conversion.[54,55]

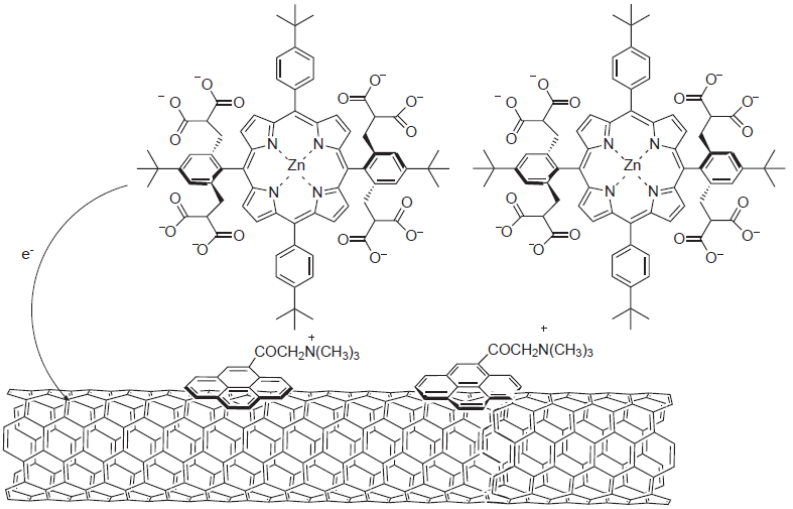

Scheme 2. Structure of SWCNT/pyrene^{+}/ZnP^{8-} nanohybrid.

[51] D. M. Guldi, G. M. A. Rahman, N. Jux, N. Tagmatarchis, M. Prato, *Angew. Chem. Int. Ed.* **2004**, *43*, 5526-5530.
[52] N. Tagmatarchis, M. Prato, D. M. Guldi, *Physica E*. **2005**, *29*, 546-550.
[53] C. Ehli, G. M. A. Rahman, N. Jux, D. Balbinot, D. M. Guldi, F. Paolucci, M. Marcaccio, D. Paolucci, M. Melle-Franco, F. Zerbetto, S. Campidelli, M. Prato, *J. Am. Chem. Soc.* **2006**, *128*, 11222-11231.
[54] D. M. Guldi, G. M. A. Rahman, M. Prato, N. Jux, S. Qin, W. Ford, *Angew. Chem. Int. Ed.* **2005**, *44*, 2015-2018.
[55] S. Sadasivan, K. Köhler, G. B. Sukhorukov, *Adv. Funct. Mater.* **2006**, *16*, 2083-2088.

Pristine SWCNTs have been used as electron-acceptor components in supramolecular "polymer wraps".[56] It is expected that a more stable complex of SWCNT is formed with oligomeric and polymeric porphyrins compared to the monomeric ones. It was demonstrated that the stability of the complex SWCNT-porphyrin is proportional to the number of porphyrin units in the triply fused Zn-porphyrin oligomers (Figure 11).[57]

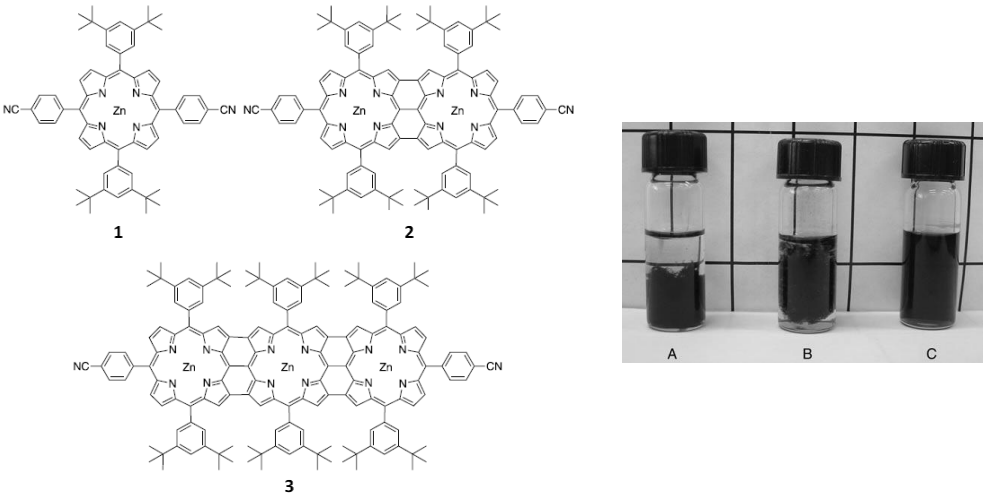

Figure 11. Structures of porphyrin monomer **1**, dimer **2**, trimer **3** and photograph of three samples in acidified THF (containing 5% TFA). SWCNT complexes of A) monomeric **1**, B) dimeric **2**, and C) trimeric **3**.

Similarly, a soluble and conjugated Zn-porphyrin polymer strongly interacted with the surface of SWCNTs, resulting in the formation of very stable and highly soluble polymer-SWCNT nanocomposites (Figure 12).[58] A successful complexation requires the addition of trifluoroacetic acid to the solvent (THF). The polymer-SWCNT assembly process induces a coplanarization in the polymer repeat units, causing enhanced conjugation and obtaining a very dark and stable solution,

[56] A. Satake, Y. Miyajima, Y. Kobuke, *Chem. Mater.* **2005**, *17*, 716-724.
[57] F. Cheng, S. Zhang, A. Adronov, L. Echegoyen, F. Diederich, *Chem. Eur. J.* **2006**, *12*, 6062-6070.
[58] F. Cheng, A. Adronov, *Chem. Eur. J.* **2006**, *12*, 5053-5059.

while it was observed that the monomer-SWCNT interactions were significantly weaker, leading to nanotube precipitation within minutes. The broad absorption spectrum of polymer-SWCNT complex, ranging from the UV to the near-IR, together with the nanotube solubility opens this novel supramolecular system to potential applications in the development of light-harvesting photovoltaic systems and other optoelectronic devices.

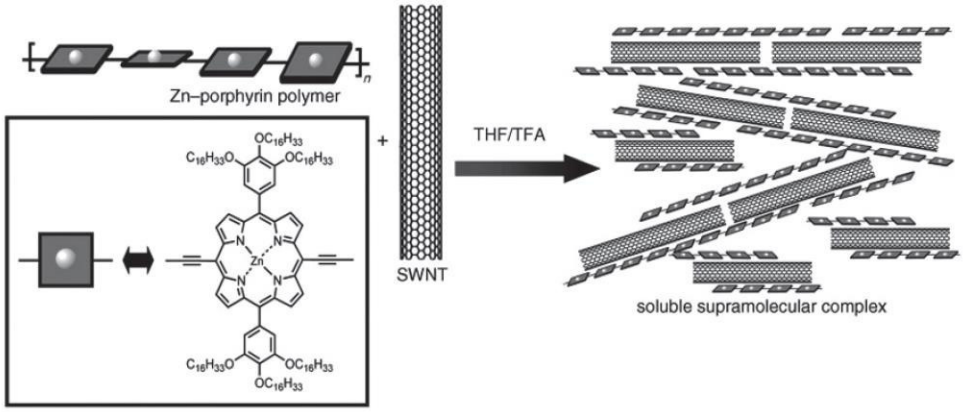

Figure 12. Supramolecular assembly of the conjugated Zn-porphyrin polymer with SWCNTs, forming a soluble polymer-nanotube complex.

Osuka et al. later described the ability of 'gable-type' porphyrin dimers not only to solubilize SWCNTs, but also to discriminate their structures.[59] These porphyrin dimers consisting of a rigid spacer and two porphyrin units with asymmetrical moieties at their periphery (Figure 13) were found to extract CoMoCAT SWCNTs. The chiral porphyrins bind with different affinities to the left- and right-handed helical nanotube isomers to form complexes with unequal stabilities that can be readily separated. Significantly, the diporphyrins can be liberated from the complexes afterwards, providing optically enriched pure

[59] (a) X. Peng, N. Komatsu, S. Bhattacharya, T. Shimawaki, S. Aonuma, T. Kimura, A. Osuka, *Nat. Nanotechnol.* **2007**, *2*, 361-365; (b) X. Peng, N. Komatsu, T. Kimura, A. Osuka, *J. Am. Chem. Soc.* **2007**, *129*, 15947-15953.

SWCNTs. Computer-generated complex structures between the stereoisomers of (6,5)-SWCNTs and the chiral porphyrin dimers are illustrated in Figure 13.

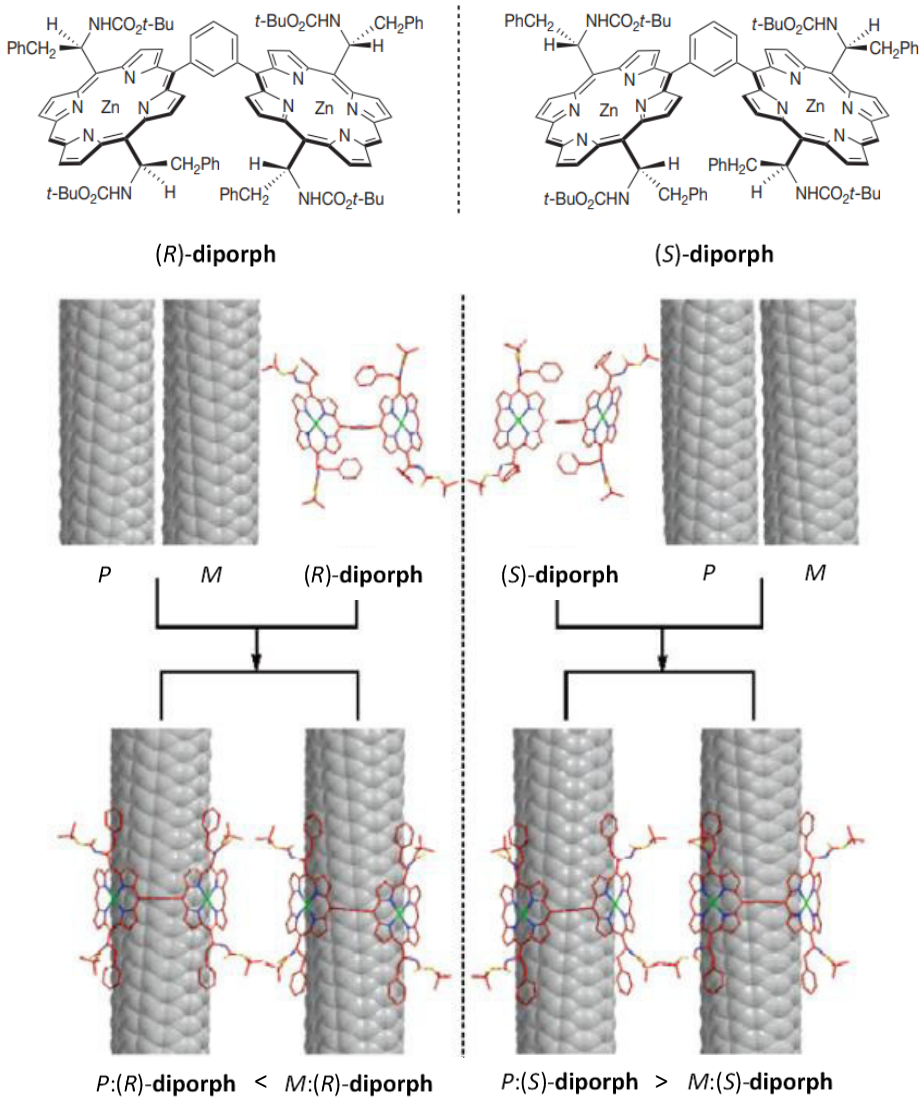

Figure 13. ‘Gable-type’ porphyrin dimers and computer-generated molecular modeling of the complexes of (*R*)- and (*S*)-**diporphyrins** with (*P*)- and (*M*)-(6,5)-SWCNTs.

1.2.3. Applications of SWCNT-porphyrin molecular assemblies

The interactions between SWCNTs and porphyrins have been investigated in a wide range of applications in nanotechnology.[60] The most explored field taking advantage of the properties of SWCNT and porphyrin assemblies is that of photosynthetic systems. Different porphyrin molecules, as well as device designs have been created.[54,61,62] In addition to the technological importance of the subject, the underlying phenomena related to the photoinduced charge transfer is of general interest in light harvesting by aromatic compounds exhibiting interactions with allotropic forms of carbon.[63,64] Porphyrins can harvest light very efficiently, converting the photons energy to a pair of electronic carriers, and carbon nanotubes can carry these generated electronic current, without significant loss, to electric pads and then to batteries, for instance.

The SWCNT-porphyrin pair has also been used as electrochemical sensor for a variety of chemical substances.[65,66] Most devices were used to detect NO_2 or H_2O_2.[67] Acetone, methanol, ethyl acetate and tetrahydrofuran among others were detected at room temperature using a network of SWCNTs covered with metalloporphyrins (Figure 14),[68] and even explosives could be detected with covalently bound SWCNT-porphyrin assemblies.[69]

[60] G. A. M. Sáfar, D. C. S. Martins, G. DeFreitas-Silva, J. S. Rebouças, Y. M. Idemori, A. Righi, *Synthetic Metals* **2014**, *193*, 64-70.
[61] G. M. A. Rahman, A. Troeger, V. Sgobba, D. M. Guldi, N. Jux, D. Balbino, M. N. Tchoul, W. T. Ford, A. Mateo-Alonso, M. Prato, *Chem. Eur. J.* **2008**, *14*, 8837-8846.
[62] Q. Zhong, V. V. Diev, S. T. Roberts, P. D. Antunez, R. L. Brutchey, S. E. Bradforth, M. E. Thompson, *ACS Nano* **2013**, *7*, 3466-3475.
[63] H. Imahori, T. Umeyama, K. Kurotobi, Y. Takano, *Chem. Commun.* **2012**, *48*, 4032-4045.
[64] L. M. Arellano, M. Barrejón, H. B. Gobeze, M. J. Gómez-Escalonilla, J. L. G. Fierro, F. D'Souza, F. Langa, *Nanoscale* **2017**, *9*, 7551-7558.
[65] S. F. Liu, A. R. Petty, G. T. Sazama, T. M. Swager, *Angew. Chem. Int. Ed.* **2015**, *54*, 6554-6557.
[66] S. F. Liu, L. C. H. Moh, T. M. Swager, *Chem. Mater.* **2015**, *27*, 3560-3563.
[67] (a) F. Valentini, L. Cristofanelli, M. Carbone, G. Palleschi, *Electrochim. Acta* **2012**, *63*, 37-46; (b) H. Jeong, M.S. Ahmed, S. Jeon, *J. Nanosci. Nanotechnol.* **2011**, *11*, 987-993.
[68] M. Penza, M. Alvisi, R. Rossi, E. Serra, R. Paolesse, A. D'Amico, C. Di Natale, *Nanotechnology* **2011**, *22*, 125502.
[69] X. Lu, Y. Quan, Z. Xue, B. Wu, H. Qi, D. Liu, *Colloids Surf. B: Biointerfaces* **2011**, *88*, 396-401.

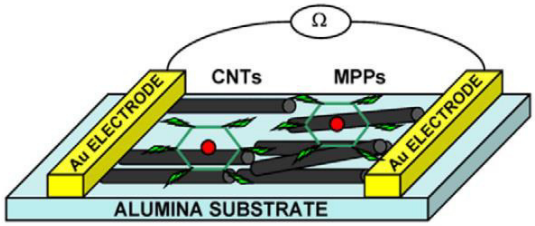

Figure 14. A pictorial view of the two-pole chemiresistor based on carbon nanotubes networks functionalized by metalloporphyrins.

Due to their large area-to-volume ratio and their low mass density, SWCNTs are excellent supports for any kind of nanometric catalysts. Metalloporphyrins are amongst the smallest and lightest existing nanocatalysts, which make the SWCNT-metalloporphyrin couple a very versatile combination for catalysis. Several works reported nanotube-porphyrin hybrids as supported catalysts for oxygen reduction reactions,[70] conversion of CO_2 into CO,[71] or even cycloaddition reactions of epoxides and CO_2 for the synthesis of cyclic carbonates[72] (Figure 15).

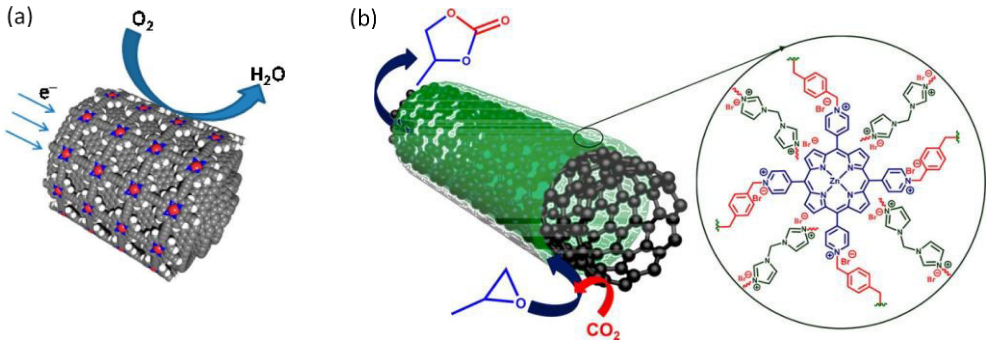

Figure 15. (a) Carbon nanotube-templated synthesis of covalent porphyrin network for oxygen reduction reaction. (b) Cationic Zn-porphyrin polymer coated onto carbon nanotubes as a cooperative catalyst for the synthesis of cyclic carbonates.

[70] (a) P.-J. Wei, G.-Q. Yu, Y. Naruta, J.-G. Liu, *Angew. Chem. Int. Ed.* **2014**, *53*, 6659-6663; (b) I. Hijazi, T. Bourgeteau, R. Cornut, A. Morozan, A. Filoramo, J. Leroy, V. Derycke, B. Jousselme, S. Campidelli, *J. Am. Chem. Soc.* **2014**, *136*, 6348-6354.
[71] A. Maurin, M. Robert, *J. Am. Chem. Soc.* **2016**, *138*, 2492-2495.
[72] S. Jayakumar, H. Li, J. Chen, Q. Yang, *ACS Appl. Mater. Interfaces* **2018**, *10*, 2546-2555.

Recently, application of these SWCNT-porphyrin hybrids as optoelectronic devices has also been described;[73] but perhaps, the most promising area for the use of SWCNT-porphyrin supramolecular assemblies in biological environment is photodynamic therapy. These assemblies have been successfully used as photosensitizers. An efficient nano-photosensitizer delivery system based on noncovalent interactions between chlorin e6 (Ce6) and SWCNTs was developed.[74] By taking advantage of the high surface area of SWCNTs, Ce6 was loaded onto SWCNT by noncovalent π-π interactions. Then, the Ce6-SWCNT assemblies were wrapped by chitosan to improve aqueous solubility and biocompatibility (Scheme 3). The resulting chitosan-Ce6-SWCNT composites exhibited low dark toxicity and high photodynamic therapy efficacy to cancer cells.

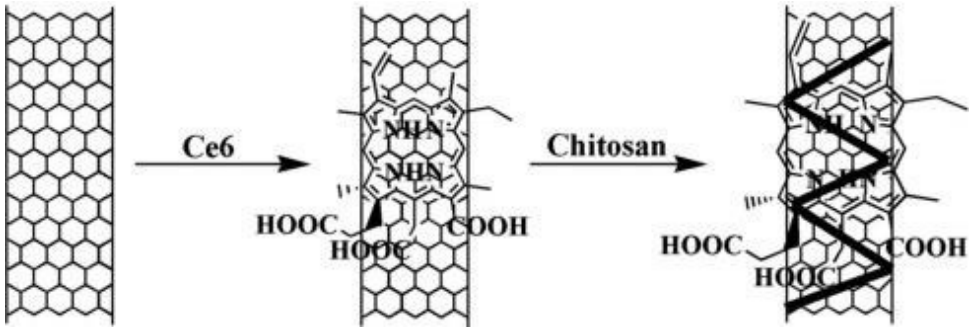

Scheme 3. Preparation steps for chitosan-Ce6-SWCNT composite.

1.3. Two-dimensional materials and porphyrins

During the first decades of the 20th century, the existence of two-dimensional (2D) materials was a highly debated issue in the physics community. According to classical physics, 2D materials are thermodynamically unstable at any finite temperature due to thermal lattice fluctuations.[75] It was not until 2004 that

[73] G. Delport, F. Vialla, C. Roquelet, S. Campidelli, C. Voisin, J.-S. Lauret, *Nano Lett.* **2017**, *17*, 6778-6782.
[74] H. Xiao, B. Zhu, D. Wang, Y. Pang, L. He, X. Ma, R. Wang, C. Jin, Y. Chen, X. Zhu, *Carbon* **2012**, *50*, 1681-1689.
[75] R. E. Peierls, *Helv. Phys. Acta* **1934**, *7*, 81-83.

materials science had a major scientific breakthrough, when Novoselov and Geim isolated the first single layer 2D material, graphene, through the Scotch tape exfoliation of graphite.[76] The importance of this achievement was sealed in 2010, when the Nobel Prize was awarded to both researchers.

Graphene is another allotrope of carbon, composed of a single atomic layer of sp^2-hybridized carbon atoms in the form of a 2D hexagonal lattice.[77,78] It is a fundamental building block for other carbon materials such as 0D fullerene, 1D carbon nanotubes and 3D graphite (Figure 16).[79]

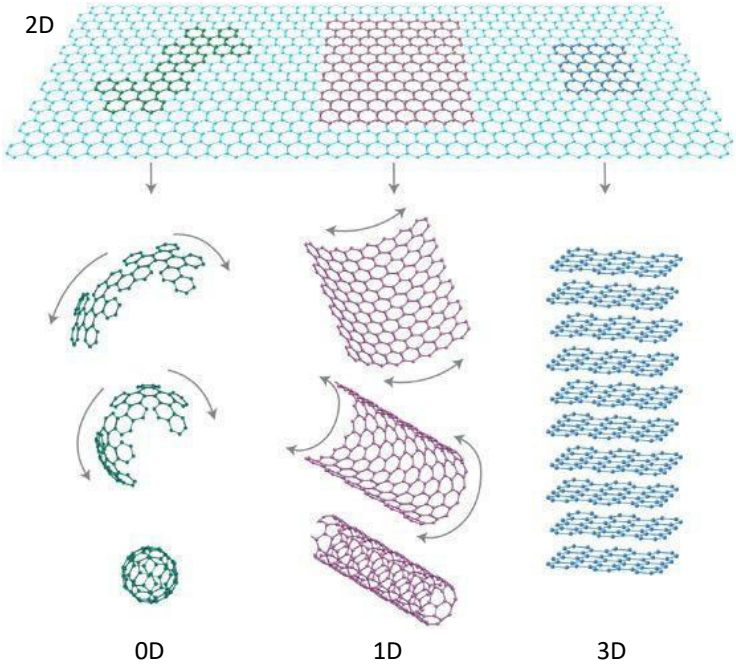

Figure 16. Mother of all graphitic forms. Graphene is a 2D building material for carbon materials of all other dimensionalities.

[76] K. S. Novoselov, A. K. Geim, S. V. Morozov, D. Jiang, Y. Zhang, S. V. Dubonos, I. V. Grigorieva, A. A. Firsov, *Science* **2004**, *306*, 666-669.
[77] P. Miró, M. Audiffred, T. Heine, *Chem. Soc. Rev.* **2014**, *43*, 6537-6554.
[78] M. Xu, T. Liang, M. Shi, H. Chen, *Chem. Rev.* **2013**, *113*, 3766-3798.
[79] A. K. Geim, K. S. Novoselov, *Nat. Mater.* **2007**, *6*, 183-191.

Many extraordinary properties of graphene have been reported. Graphene is the first truly 2D material, being only one atom thick. This leads to a high surface area of 2630 m^2/g for a single graphene sheet.[80] It also exhibits high carrier mobility, that can be as high as 10^5 $cm^2 V^{-1} s^{-1}$ at room temperature and 10^6 $cm^2 V^{-1} s^{-1}$ at low temperature.[81] Graphene has almost the same crystal energy as diamond, but as each graphene carbon has only three bonds instead of four for diamond, the graphene C-C bonds are about 25% stronger. Its Young's modulus has been found to be 1.0 TPa, which establish graphene as one of the strongest materials known to date.[82] It also shows excellent thermal conductivity, ~5000 W/mK,[83] and a 2.3% of absorption in the white light spectrum, as a consequence of its unique electronic structure.[84]

Because of these remarkable properties, many applications using graphene have been explored in a wide range of areas, including high-speed electronics[85] and optical devices,[86] energy generation and storage,[87,88] hybrid materials,[89,90] chemical sensors,[91] and even DNA sequencing.[92,93]

[80] M. D. Stoller, S. Park, Y. Zhu, J. An, R. S. Ruoff, *Nano Lett.* **2008**, *8*, 3498-3502.
[81] A. S. Mayorov, R. V. Gorbachev, S. V. Morozov, L. Britnell, R. Jalil, L. A. Ponomarenko, P. Blake, K. S. Novoselov, K. Watanabe, T. Taniguchi, A. K. Geim, *Nano Lett*. **2011**, *11*, 2396-2399.
[82] C. Lee, X. Wei, J. W. Kysar, J. Hone, *Science* **2008**, *321*, 385-388.
[83] A. A. Balandin, S. Ghosh, W. Bao, I. Calizo, D. Teweldebrhan, F. Miao, C. N. Lau, *Nano Lett*. **2008**, *8*, 902-907.
[84] R. R. Nair, P. Blake, A. N. Grigorenko, K. S. Novoselov, T. J. Booth, T. Stauber, N. M. R. Peres, A. K. Geim, *Science* **2008**, *320*, 1308.
[85] Y.-M. Lin, C. Dimitrakopoulos, K. A. Jenkins, D. B. Farmer, H.-Y. Chiu, A. Grill, P. Avouris, *Science* **2010**, *327*, 662.
[86] M. Liu, X. Yin, E. Ulin-Avila, B. Geng, T. Zentgraf, L. Ju, F. Wang, X. Zhang, *Nature* **2011**, *474*, 64-67.
[87] K. S. Kim, Y. Zhao, H. Jang, S. Y. Lee, J. M. Kim, K. S. Kim, J.-H. Ahn, P. Kim, J.-Y. Choi, B. H. Hong, *Nature* **2009**, *457*, 706-710.
[88] Y. Zhu, S. Murali, M. D. Stoller, K. J. Ganesh, W. Cai, P. J. Ferreira, A. Pirkle, R. M. Wallace, K. A. Cychosz, M. Thommes, D. Su, E. A. Stach, R. S. Ruoff, *Science* **2011**, *332*, 1537-1541.
[89] M. F. El-Kady, V. Strong, S. Dubin, R. B. Kaner, *Science* **2012**, *335*, 1326-1330.
[90] X. Yang, M. Xu, W. Qiu, X. Chen, M. Deng, J. Zhang, H. Iwai, E. Watanabe, H. Chen, *J. Mater. Chem.* **2011**, *21*, 8096-8103.
[91] M. Deng, X. Yang, M. Silke, W. Qiu, M. Xu, G. Borghs, H. Chen, *Sensors Actuators B: Chem.* **2011**, *158*, 176-184.
[92] M. Xu, D. Fujita, N. Hanagata, *Small* **2009**, *5*, 2638-2649.
[93] S. Garaj, W. Hubbard, A. Reina, J. Kong, D. Branton, J. A. Golovchenko, *Nature* **2010**, *467*, 190-193.

However, pristine graphene itself is unlikely to be used for the fabrication of logical circuits operated at room temperature with low standby power dissipation, resulting in a small current on/off ratio in graphene field-effect transistors (FETs).[94] This is because graphene is a semi-metal without band gap, the density-of-states is zero at the Fermi level (Figure 17a). The Fermi level is crossed by electronic bands near the six corners of the two-dimensional hexagonal Brillouin zone (Figure 17b). The dispersion relation is linear at these points, a unique feature that leads to zero effective mass for electrons and holes, and thus to very high currents. Due to this linear or conical dispersion relation, electrons and holes near these six points behave like relativistic particles described by the Dirac equation. Therefore, the electrons and holes are called Dirac fermions and the six corners of the Brillouin zone are called Dirac points.

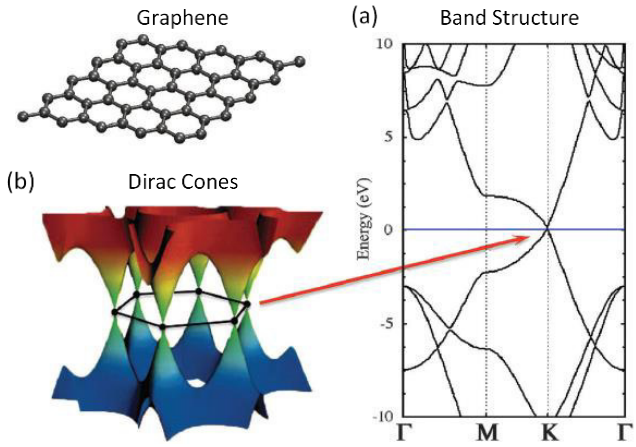

Figure 17. Graphene, the prototype 2D material. (a) Graphene band structure. (b) Dirac cones in graphene.

The existence of this zero band gap for pristine graphene, could be interpreted as a drawback for certain applications, so due to the fascinating

[94] K. Kim, J.-Y. Choi, T. Kim, S.-H. Cho, H.-J. Chung, *Nature* **2011**, *479*, 338-344.

properties and extensive applications of graphene, other 2D layered materials such as metal chalcogenides, transition metal oxides, etc. gained renewed interest.

Transition metal dichalcogenides (TMDCs) consist of hexagonal layers of metal atoms (M) sandwiched between two layers of chalcogen atoms (X) with a MX_2 stoichiometry (Figure 18). Depending on the combination of chalcogen (typically S, Se or Te) and transition metal (typically Mo, W, Nb, Re, Ni or V),[95] TMDCs occur in more than 40 different categories.

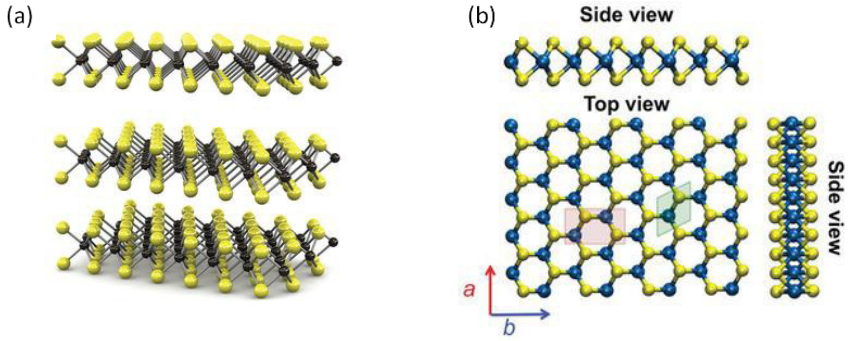

Figure 18. (a) Schematic representation of a typical MX_2 structure, with the metal atoms (M) in black and the chalcogen atoms (X) in yellow. (b) Top and side view of a MX_2 monolayer.

Together with layered transition oxides[96] such as MoO_3 and La_2CuO_4,[97] insulator hexagonal boron nitride (*h*-BN),[98] and topological insulators like Bi_2Te_3, Sb_2Se_3 and Bi_2Se_3,[99] the common feature of these layered materials is that the bulk 3D crystals are stacked structures. They involve van der Waals interactions between adjacent sheets with strong covalent bonding within each sheet. Such materials span the entire range of electronic structures, from insulator to metal, and display

[95] J. A. Wilson, A. D. Yoffe, *Adv. Phys.* **1969**, *18*, 193-335.
[96] M. Osada, T. Sasaki, *Adv. Mater.* **2012**, *24*, 210-228.
[97] L. Hozoi, L. Siurakshina, P. Fulde, J. van der Brink, *Sci. Rep.* **2011**, *1*, 65.
[98] D. Golberg, Y. Bando, Y. Huang, T. Terao, M. Mitome, C. Tang, C. Zhi, *ACS Nano* **2010**, *4*, 2979-2993.
[99] H. Zhang, C.-X. Liu, X.-L. Qi, X. Dai, Z. Fang, S.-C. Zhang, *Nat. Phys.* **2009**, *5*, 438-442.

interesting properties. These include the topological insulator effect,[100,101] superconductivity,[102] and thermoelectricity.[103]

Furthermore, a strong interest in group-IV graphene-like 2D buckled nanosheets emerged. Silicene and germanene, the silicon- or germanium-based counterparts of graphene, are found to exhibit similar features in the electronic band structure to graphene;[104] the bands cross at the Fermi level, located in the Dirac points of the reciprocal lattice. Interestingly, the linear dispersion, which results from the honeycomb structure, is preserved even when the hybridization of the atoms changes (C is in sp^2 hybridization, while isoelectronic Si and Ge prefer sp^3).

Because of their distinct properties and high specific surface areas, these 2D materials are important in various applications such as optoelectronics, spintronics, catalysts,[105] chemical and biological sensors,[106] supercapacitors, solar cells,[107] and lithium ion batteries.[108]

In contrast to the zero band gap of pristine graphene, bulk MoS_2 is a semiconductor with an indirect band gap of 1.23 eV.[109] Several studies[110,111] have confirmed a transition from an indirect band gap to a direct band gap (E_g = 1.90 eV) for MoS_2 as the thickness of this material decreased to a monolayer (Figure 19). This accounts for more than a 10^4-fold enhancement of the photoluminescence quantum yield from bulk to monolayer MoS_2.[112] The result is that MoS_2 is a

[100] M. Lang, L. He, F. Xiu, X. Yu, J. Tang, Y. Wang, X. Kou, W. Jiang, A. V. Fedorov, K. L. Wang, *ACS Nano* **2012**, *6*, 295-302.
[101] H. B. Zhang, H. L. Yu, D. H. Bao, S. W. Li, C. X. Wang, G. W. Yang, *Adv. Mater.* **2012**, *24*, 132-136.
[102] F. R. Gamble, B. G. Silbernagel, *J. Chem. Phys.* **1975**, *63*, 2544-2552.
[103] X. Tang, W. Xie, H. Li, W. Zhao, Q. Zhang, M. Niino, *Appl. Phys. Lett.* **2007**, *90*, 012102.
[104] S. Cahangirov, M. Topsakal, E. Aktürk, H. Sahin, S. Ciraci, *Phys. Rev. Lett.* **2009**, *102*, 236804.
[105] J. Liu, C. Guo, A. Vasileff, S. Qiao, *Small Methods* **2017**, *1*, 1600006.
[106] B. Ryu, E. Yang, Y. Park, K. Kurabayashi, X. Liang, *J. Vac. Sci. Technol. B* **2017**, *35*, 06G805.
[107] C. Li, Q. Cao, F. Wang, Y. Xiao, Y. Li, J.-J. Delaunay, H. Zhu, *Chem. Soc. Rev.* **2018**, *47*, 4981-5037.
[108] S. Wang, B. Y. Guan, L. Yu, X. W. Lou, *Adv. Mater.* **2017**, *29*, 1702724.
[109] K. Dolui, C. D. Pemmaraju, S. Sanvito, *ACS Nano* **2012**, *6*, 4823-4834.
[110] A. Splendiani, L. Sun, Y. Zhang, T. Li, J. Kim, C.-Y. Chim, G. Galli, F. Wang, *Nano Lett.* **2010**, *10*, 1271-1275.
[111] T. Korn, S. Heydrich, M. Hirmer, J. Schmutzler, C. Schüller, *Appl. Phys. Lett.* **2011**, *99*, 102109.
[112] K. F. Mak, C. Lee, J. Hone, J. Shan, T. F. Heinz, *Phys. Rev. Lett.* **2010**, *105*, 136805.

promising material that has the potential to be used in building FETs,[113] digital circuits[114] and light-emitting diodes. For instance, the current on/off ratio of single-layer MoS_2 transistors exceeds 10^8 at room temperature.[115] This is much higher than that (approximately 100) of graphene transistors.[79]

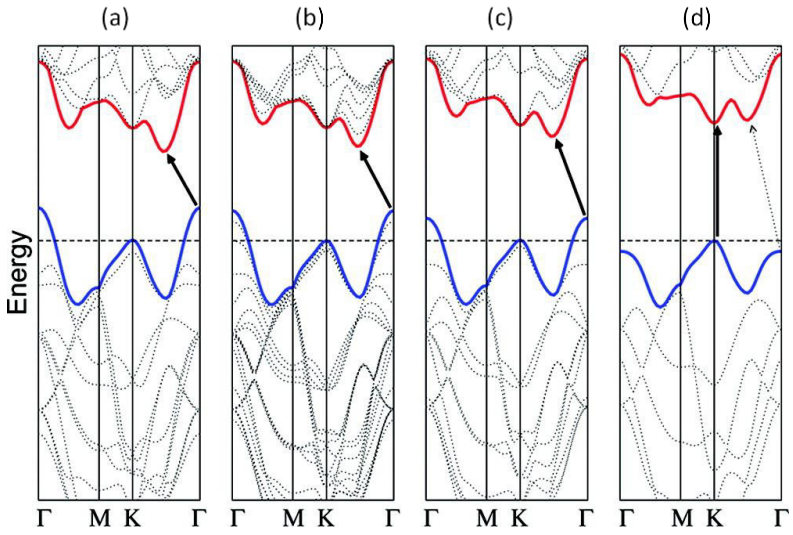

Figure 19. Calculated band structures of (a) bulk, (b) quadrilayer, (c) bilayer, and (d) monolayer MoS_2. The solid arrows indicate the lowest energy transitions.

The use of these 2D materials in certain real-world applications would benefit from their chemical functionalization to add new functionalities or to modify inherent physical properties. Both covalent and non-covalent functionalization of graphene and other 2D compounds represent a very challenging and important research field.

[113] H. Wang, L. Yu, Y.-H. Lee, Y. Shi, A. Hsu, M. L. Chin. L.-J. Li, M. Dubey, J. Kong, T. Palacios, *Nano Lett.* **2012**, *12*, 4674-4680.
[114] B. Radisavljevic, M. B. Whitwick, A. Kis, *ACS Nano* **2011**, *5*, 9934-9938.
[115] B. Radisavljevic, A. Radenovic, J. Brivio, V. Giacometti, A. Kis, *Nat. Nanotechnol.* **2011**, *6*, 147-150.

Following our research line, based on combining porphyrins and nanomaterials, some representative examples on the functionalization of 2D materials with porphyrins are studied.

1.3.1. Graphene-porphyrin systems

1.3.1.1. Covalently linked graphene-porphyrin systems

Just as in the case of SWCNTs, the covalent functionalization of graphene requires the formation of covalent bonds on the basal plane of its carbon lattice, an addition which changes the hybridization of the addend-carrying graphene carbon atoms from sp^2 to sp^3. This process can be formally considered as an introduction of defects, and leads to the modification of the electronic, optical and mechanical properties of the 2D carbon allotrope. On the other hand, the covalent functionalization offers the opportunity to improve the solubility and processability of graphene. Furthermore, this covalent functionalization allows for the combination of the unique properties of graphene with those of photo- and electroactive compounds, such as porphyrins.

To date, several strategies have been used for the covalent functionalization of graphene with porphyrins,[31,116] most of them employing the same synthetic protocols previously described for the functionalization of carbon nanotubes.

Graphene oxide (GO) has often been employed as the starting material for the preparation of graphene derivatives through acylation reactions, due to the hydroxyl, carboxyl and epoxy groups providing remarkable hydrophilic character and chemical reactivity.[117,118] The covalent linking of porphyrins to graphene has been achieved by esterification/amidation of hydroxyl/amino-appended porphyrins

[116] A. Wang, J. Ye, M. G. Humphrey, C. Zhang, *Adv. Mater.* **2018**, *30*, 1705704.
[117] S. H. Noh, H. Park, W. Jang, K. H. Koh, M. Yi, J. M. Lee, S. Thirumalairajan, J. Y. Jaung, D. H. Wang, T. H. Han, *Carbon* **2017**, *119*, 476-482.
[118] R. K. Yadav, J.-O. Baeg, G. H. Oh, N.-J. Park, K. Kong, J. Kim, D. W. Hwang, S. K. Biswas, *J. Am. Chem. Soc.* **2012**, *134*, 11455-11461.

with GO, as in the case of oxidized SWCNTs. Chen et al. in 2009 reported one of the first coupling of porphyrins and GO by condensing an amino-modified tetraphenylporphyrin (TPP) to the carboxylic-functionalized GO and affording GO-TPP nanohybrids (Scheme 4).[119]

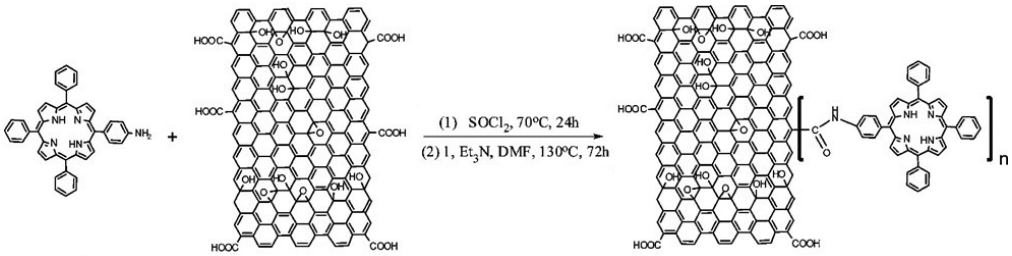

Scheme 4. Synthesis of the GO-TPP composite.

Aryl addition reactions of diazonium compounds and cycloadditions of azomethine ylides to the π-network of the graphene surface have also been demonstrated.[120,121] Zhang et al. prepared a porphyrin-graphene covalent composite (Figure 20a) by a two-step functionalization procedure, i.e., the preparation of prefunctionalized graphene with *p*-ethynylphenyl groups by the direct aryl addition reaction, and subsequent click reactions with azide-terminated porphyrin.[122] This composite has a relatively long, tilted phenylene-triazole-phenylene spacer between the porphyrins and the graphene sheets. The absorption spectrum of the porphyrin-graphene hybrid revealed the broadening and redshift of the Soret band relative to the porphyrin reference, suggesting the significant interaction between the porphyrin and the graphene in the ground state. Upon

[119] Y. Xu, Z. Liu, X. Zhang, Y. Wang, J. Tian, Y. Huang, Y. Ma, X. Zhang, Y. Chen, *Adv. Mater.* **2009**, *21*, 1275-1279.
[120] J. R. Lomeda, C. D. Doyle, D. V. Kosynkin, W.-F. Hwang, J. M. Tour, *J. Am. Chem. Soc.* **2008**, *130*, 16201-16206.
[121] M.-E. Ragoussi, J. Malig, G. Katsukis, B. Butz, E. Spiecker, G. Torre, T. Torres, D. M. Guldi, *Angew. Chem. Int. Ed.* **2012**, *51*, 6421-6425.
[122] H.-X. Wang, K.-G. Zhou, Y.-L. Xie, J. Zeng, N.-N. Chai, J. Li, H.-L. Zhang, *Chem. Commun.* **2011**, *47*, 5747-5749.

excitation, the effective emission quenching of the porphyrin in the composite is also indicative of the strong electronic interaction.

Feringa et al. synthesized a porphyrin-graphene covalent composite by a one-step cycloaddition reaction using azomethine ylide with free-base porphyrin units (Figure 20b).[123] They prepared graphene by solvent dispersion of graphite because it gives the advantage of retaining the intrinsic properties of graphene while maintaining the dispersibility of graphene in certain solvents. Fluorescence quenching was observed with concomitant decreases in excited state lifetimes, confirming that energy- and/or electron-transfer processes between graphene and the covalently bound porphyrins occur. The amounts of TPP present in the hybrids were determined by TGA and the covalent linkages were confirmed by Raman and FTIR spectroscopy.

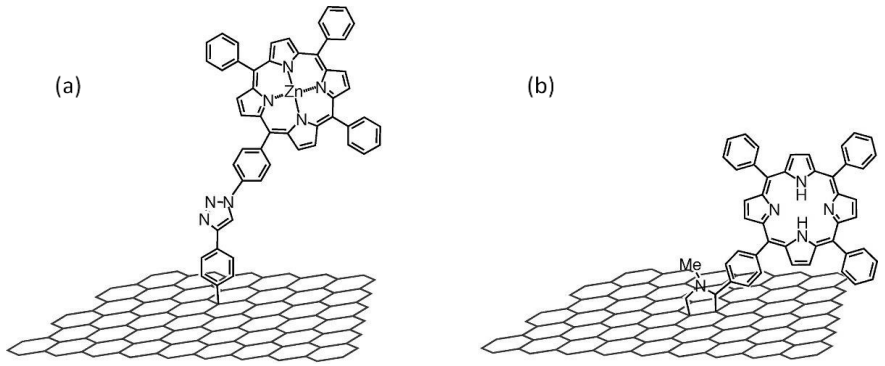

Figure 20. Structures of porphyrin-graphene linked hybrids, prepared by (a) aryl addition reaction of diazonium compounds and (b) cycloaddition reaction of azomethine ylides.

The functionalities incorporated by the 1,3-dipolar cycloaddition are dispersed across the graphene surface, with a higher density localized next to the defects. This is in contrast to functionalization via ester/amide bond condensation,

[123] X. Zhang, L. Hou, A. Cnossen, A. C. Coleman, O. Ivashenko, P. Rudolf, B. J. van Wees, W. R. Browne, B. L. Feringa, *Chem. Eur. J.* **2011**, *17*, 8957-8964.

where these functionalities only exist at the edges. The morphology of the nanohybrids is not affected by the cycloaddition reactions, and the relatively low degree of graphene functionalization allows the retention of the inherent properties of graphene, rendering the samples suitable for optoelectronic applications.

Regarding photoinduced charge transfer interactions in donor-acceptor porphyrin-graphene covalent hybrids, chemically converted graphene (CCG) covalently linked with porphyrins was prepared by a Suzuki coupling reaction between iodophenyl-functionalized CCG and porphyrin boronic ester as shown in Scheme 5.[124] In this case, the covalently linked CCG-porphyrin composite was designed to possess a short, rigid phenylene spacer between the porphyrin and the graphene. The composite material formed stable dispersions in DMF and the structure was characterized by spectroscopic, thermal and microscopic measurements. Fluorescence lifetime and femtosecond transient absorption measurements of the porphyrin-linked CCG revealed a short-lived porphyrin singlet excited state, without yielding the porphyrin radical cation. This observation substantiated the occurrence of energy transfer from the porphyrin excited state to graphene and subsequent rapid decay of the CCG excited state to the ground state. Accordingly, the photocurrent action spectrum of a photoelectrochemical device with a SnO_2 electrode coated with the porphyrin-linked CCG exhibited no photocurrent response from the porphyrin absorption.

[124] T. Umeyama, J. Mihara, N. Tezuka, Y. Matano, K. Stranius, V. Chukharev, N. V. Tkachenko, H. Lemmetyinen, K. Noda, K. Matsushige, T. Shishido, Z. Liu, K. Hirose-Takai, K. Suenaga, H. Imahori, *Chem. Eur. J.* **2012**, *18*, 4250-4257.

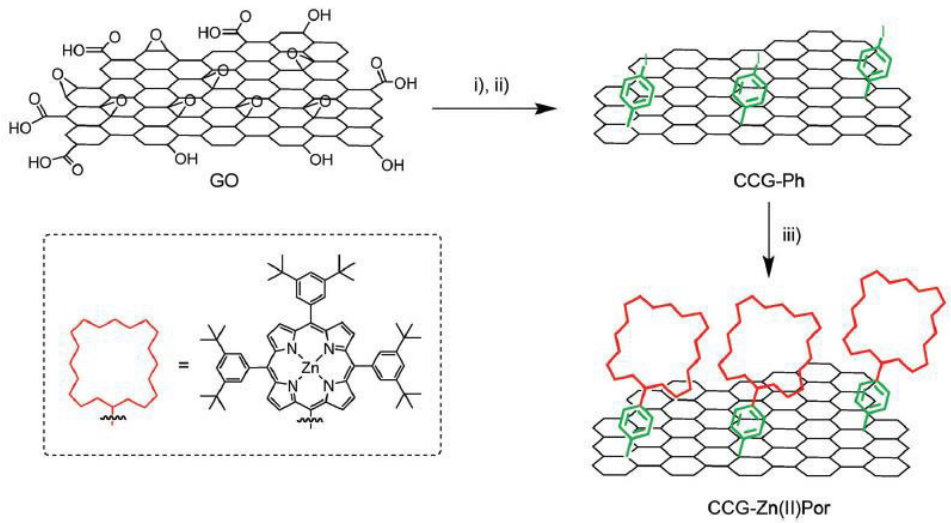

Scheme 5. Synthesis of porphyrin-linked CCG. (i) Sodium dodecylsulfate (SDS), $N_2H_4 \cdot H_2O$, NH_3 (aqueous), 95 °C, 1 h; (ii) 4-iodobenzenediazonium tetrafluoroborate, H_2O, r.t., 2 h; (iii) 5,10,15-tris(3,5-di-*tert*-butylphenyl)-20-(4,4,5,5-tetramethyl[1,3,2]dioxaborolan-2-yl)Zn(II) porphyrin, $Pd(PPh_3)_4$, Cs_2CO_3, DMF, 90 °C, 24h.

1.3.1.2. Non-covalently linked graphene-porphyrin systems

Graphene, in a similar way to carbon nanotubes, shows the feature of delocalized and conjugated electron structure. By virtue of its 2D structure, it represents an ideal platform for the preparation of tailored hybrid materials through non-covalent interactions with opto- and electronically active organic components such as porphyrins.

Non-covalent functionalization of graphene with porphyrins through electrostatic and π-π interactions, is also particularly attractive since it allows preserving the conjugated π-system of graphene. Moreover, this modification also let to enhance its solubility and self-assembly properties. Strategies that were used earlier in the context of carbon nanotubes, have been also explored for the non-covalent functionalization of graphene with porphyrins.[125]

[125] G. Bottari, M. A. Herranz, L. Wibmer, M. Volland, L. Rodríguez-Pérez, D. M. Guldi, A. Hirsch, N. Martín, F. D'Souza, T. Torres, *Chem. Soc. Rev.* **2017**, *46*, 4464-4500.

There have been several methods for the preparation of graphene, mechanical exfoliation,[76] solvent dispersion of graphite,[126] chemical methods,[127] and chemical vapor deposition.[128] Each of these methods has different advantages and disadvantages. In 2010, Jung et al. developed a simple and efficient method for the preparation of high-quality graphene *via* non-ionic porphyrin exfoliation of graphite in *N*-methyl-pyrrolidone (NMP).[129] The exfoliation is attributed to the π-π interactions between graphene and porphyrins, and follows the intercalation of organic ammonium ions. It was shown that both the porphyrin and tetrabutyl-ammonium hydroxide (TBA) play important roles in generating high concentrations of dispersed graphene. It is also important to note that the graphene prepared has a concentration as high as *ca*. 0.05 mg ml^{-1}, which is *ca.* 5 times higher than that produced by using a previously reported method, exfoliating graphite in NMP but without the presence of porphyrins.[126] The graphene sheets obtained by this method show undisturbed sp^2 carbon networks. Moreover, this method is more versatile, showing another advantage in preparing photoactive graphene-porphyrin hybrids due to porphyrin's unique photochemical properties.

Shi et al. reported the supramolecular assembly or complexation of cationic 5,10,15,20-tetrakis(1-methyl-4-pyridinio)porphyrin (TMPyP) and negatively charged chemically converted graphene (CCG) sheets in aqueous media.[130] During the process, a large bathochromic shift of the porphyrin Soret band was observed, which was attributed to the flattening of porphyrin molecules induced by CCG through electrostatic and π-π stacking cooperative interactions (Figure 21). Furthermore, this flattening of TMPyP in the complex of TMPyP and CCG greatly

[126] Y. Hernandez, V. Nicolosi, M. Lotya, F. M. Blighe, Z. Sun, S. De, I. T. McGovern, B. Holland, M. Byrne, Y. K. Gun'ko, J. J. Boland, P. Niraj, G. Duesberg, S. Krishnamurthy, R. Goodhue, J. Hutchison, V. Scardaci, A. C. Ferrari, J. N. Coleman, *Nat. Nanotechnol.* **2008**, *3*, 563-568.
[127] S. Park, R. S. Ruoff, *Nat. Nanotechnol.* **2009**, *4*, 217-224.
[128] A. Reina, X. Jia, J. Ho, D. Nezich, H. Son, V. Bulovic, M. S. Dresselhaus, J. Kong, *Nano Lett.* **2009**, *9*, 30-35.
[129] J. Geng, B.-S. Kong, S. B. Yanga, H.-T. Jung, *Chem. Commun.* **2010**, *46*, 5091-5093.
[130] Y. Xu, L. Zhao, H. Bai, W. Hong, C. Li, G. Shi, *J. Am. Chem. Soc.* **2009**, *131*, 13490-13497.

accelerated the incorporation of Cd^{2+} ions into the porphyrin rings. Thus, TMPyP/CCG complex can be used as a new optical probe for sensing Cd^{2+} ions, exhibiting rapid and selective responses and improving selectivity toward cadmium (II) ions in aqueous media.

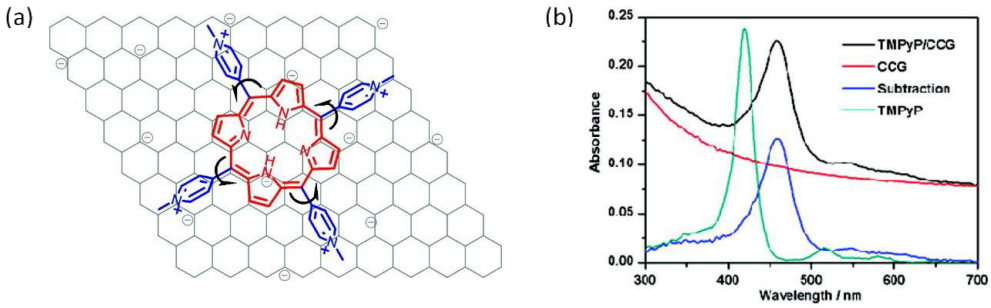

Figure 21. (a) Molecular flattening of TMPyP adsorbed on the CCG sheet. (b) Absorption spectra of the TMPyP/CCG complex formed, pure CCG and pure TMPyP solutions, and the subtraction spectrum between the spectra of the TMPyP/CCG complex and CCG.

Just like porphyrin-graphene covalent hybrids, non-covalent interaction of photosensitizers such as porphyrins or phthalocyanines with graphene also provides interesting electron donor-acceptor systems.

Supramolecular D-A hybrids composed of few-layer graphene as an electron acceptor and **$(Pyr)_4Zn(II)Por$** or **$(Pyr)_4H_2Pc$** bearing four pyrene entities as photosensitizer donors (Figure 22) were formulated and characterized by various techniques.[131] Due to the presence of four pyrene units, strong ground and excited state interactions were observed wherein the fluorescence of both porphyrin and phthalocyanine was quenched by over 80% due to interactions with graphene. Femtosecond transient absorption studies on these hybrids revealed occurrence of ultrafast charge separation whose rates were on the order of 10^{11}-10^{12} s^{-1}. The fast

[131] C. B. KC, S. K. Das, K. Ohkubo, S. Fukuzumi, F. D'Souza, *Chem. Commun.* **2012**, *48*, 11859-11861.

kinetic process was attributed to the close proximity of the donor and acceptor entities in the π-stacked D-A hybrids.

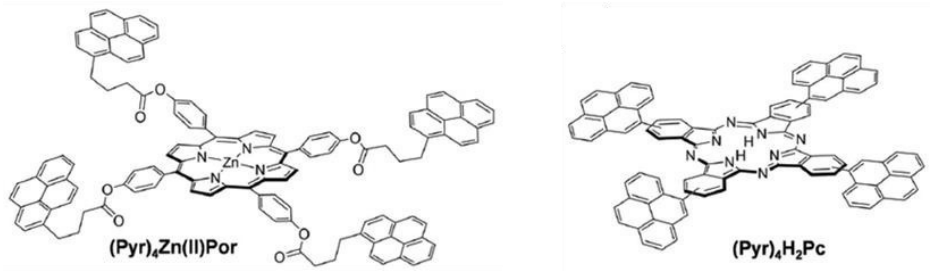

Figure 22. Molecular structure of pyrene-substituted **(Pyr)$_4$Zn(II)Por** and **(Pyr)$_4$H$_2$Pc**.

As iron porphyrins play a vital role in oxygen transport and reduction reactions in biological systems,[3] and cathodic oxygen reduction reaction (ORR) is an active area of research because of its crucial role in electrochemical energy conversion in fuel cells,[132] Loh et al. in 2012 considered attractive to study if iron porphyrins supported on graphene could function as an alternative to Pt-based electrode in fuel cells for ORR in alkaline media.[133] They employed reduced graphene oxide sheets that were functionalized on either side of the basal plane with pyridine ligands; these function as struts to link metalloporphyrin nodes to form the hybrid graphene-MOF framework (Figure 23). At the same time, the oxygenated functional groups on the graphene could facilitate ORR by acting as an electron transfer mediator. The results showed that the addition of pyridine-functionalized graphene changes the crystallization process of iron-porphyrin in the MOF, increases its porosity and enhances the electrochemical charge transfer rate of iron-porphyrin. The graphene-metalloporphyrin hybrid shows facile 4-electron ORR and can be used as a promising Pt-free cathode in alkaline Direct Methanol Fuel Cell.

[132] R. Bashyam, P. Zelenay, *Nature* **2006**, *443*, 63-66.
[133] M. Jahan, Q. Bao, K. P. Loh, *J. Am. Chem. Soc.* **2012**, *134*, 6707-6713.

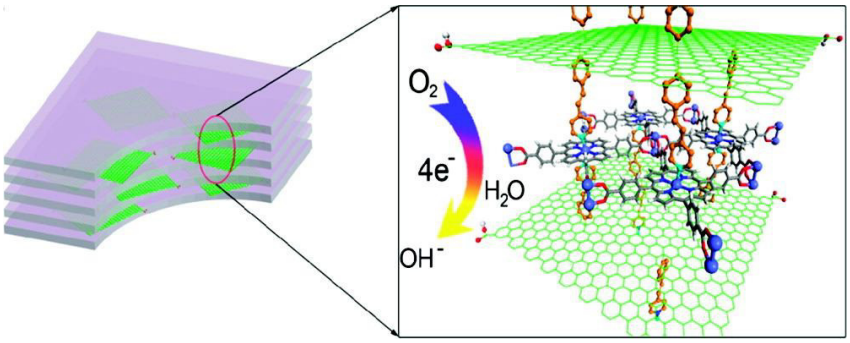

Figure 23. Magnified view of layers inside the framework of graphene-MOF, showing how graphene sheets intercalated between porphyrin networks.

1.3.2. MoS_2-porphyrin composites

There has also been wide interest in studies of TMDCs in the past few years because of their unique layer-number-dependent physical properties and potential applications in electronics, catalysis, energy storage and sensing.[134] Molybdenum disulfide (MoS_2) demonstrates high in-plane carrier mobility and on/off ratio,[115] which are critical in nanoelectronics and optoelectronics.[112] It also has been explored as a promising photoelectrode material in photoelectrochemical cells.[135] Its good stability against photo-damage and wide range of visible absorption, render MoS_2 useful as photoanodes.[136] Given the cost-effectiveness and excellent electrocatalytic properties of MoS_2, it has been explored as an additive agent for counter electrodes in dye-sensitized solar cells (DSSCs).[137] MoS_2 may also be exploited as a catalyst for the hydrogen-evolution reaction,[138] in which sulfur vacancies from optimized 2H-MoS_2 monolayers can serve as catalytic sites.

[134] Q. H. Wang, K. Kalantar-Zadeh, A. Kis, J. N. Coleman, M. S. Strano, *Nat. Nanotechnol.* **2012**, *7*, 699-712.
[135] M. Buscema, J. O. Island, D. J. Groenendijk, S. I. Blanter, G. A. Steele, H. S. van der Zant, A. Castellanos-Gomez, *Chem. Soc. Rev.* **2015**, *44*, 3691-3718.
[136] A. M. Goldberg, A. R. Beal, F. A. Lévy, E. A. Davis, *Philos. Mag.* **1975**, *32*, 367-378.
[137] J. Zhang, S. Najmaei, H. Lin, J. Lou, *Nanoscale* **2014**, *6*, 5279-5283.
[138] Q. Xiang, J. Yu, M. Jaroniec, *J. Am. Chem. Soc.* **2012**, *134*, 6575-6578.

Despite the advantages of MoS_2, there are several challenges in utilizing this 2D material in some applications, such as preparation of large-area 2D MoS_2 films, non-radiative recombination or suppression of charge transfer due to small crystallites and crystal defects.[139,140] Thus, to overcome these issues, some groups have investigated the covalent and non-covalent functionalization of MoS_2 nanosheets with different species. In relation to porphyrins, some examples of MoS_2-porphyrin composites have been reported.

Typically, functionalization of MoS_2 is achieved through the binding of sulfur-containing ligands with the unsaturated molybdenum sites present at the edges or basal planes.[141] Another general method to form covalent bonds between organic functional groups and the sulfur atoms of MoS_2, which does not rely on defect engineering, was reported by Chhowalla et al.[142]

Recently, Rao et al. have carried out the covalent functionalization of nanosheets of MoS_2 by substituted benzenes and other organic molecules, like porphyrins.[143] They studied the reaction of MoS_2 with *para*-substituted iodobenzenes, where the electron-withdrawing or -donating power of the *para* substituent varies significantly in order to examine the electronic transfer involving the reaction in determining the reactivity of the sulfur sites. Exfoliated MoS_2, containing excess electrons on the surface, acts as a nucleophile and undergoes nucleophilic substitution of the iodo group in iodobenzene by the sulfur of MoS_2, thereby forming the C-S bond. In order to establish the generality of the functionalization reaction, they carried out the reactions with few other organic molecules, such as pyrene, coumarin and porphyrin derivatives. Reaction of

[139] L. A. King, W. Zhao, M. Chhowalla, D. J. Riley, G. Eda, *J. Mater. Chem. A* **2013**, *1*, 8935-8941.
[140] H. Nan, Z. Wang, W. Wang, Z. Liang, Y. Lu, Q. Chen, D. He, P. Tan, F. Miao, X. Wang, J. Wang, Z. Ni, *ACS Nano* **2014**, *8*, 5738-5745.
[141] E. P. Nguyen, B. J. Carey, J. Z. Ou, J. van Embden, E. D. Gaspera, A. F. Chrimes, M. J. S. Spencer, S. Zhuiykov, K. Kalantar-zadeh, T. Daeneke, *Adv. Mater.* **2015**, *27*, 6225-6229.
[142] D. Voiry, A. Goswami, R. Kappera, C. de Carvalho Castro e Silva, D. Kaplan, T. Fujita, M. Chen, T. Asefa, M. Chhowalla, *Nat. Chem.* **2014**, *7*, 45-49.
[143] P. Vishnoi, A. Sampath, U. V. Waghmare, C. N. R. Rao, *Chem. Eur. J.* **2017**, *23*, 886-895.

tetra(4-bromophenyl)porphyrin gives an adduct with MoS_2, which shows photoluminescence as well as absorption spectral characteristics of the porphyrin. This functionalization of MoS_2 causes remarkable changes in its photophysical properties and increases the potential for applications in photocatalysis as in electronic and optoelectronic devices.

Choi et al. demonstrated interfacial molecular engineering of large-area 2D MoS_2 films to enhance their photoelectrochemical properties. The aim of this study was to develop a facile method for engineering MoS_2 nanolayers with porphyrin molecules to improve light-harvesting characteristics.[144] In particular, eight porphyrin species from three distinct families were examined (Figure 24). These porphyrin molecules were physically adsorbed onto large-area 2D MoS_2 films and studied by using atomic force microscopy (AFM), micro-Raman spectroscopy and photoelectrochemistry. They found that the photocurrent is greatly dependent upon the porphyrin molecules at the interface. For example, ZnPP demonstrated a maximum tenfold increase in photocurrent, whereas H_2T4 and ZnTPP do not alter the MoS_2 photocurrent significantly, concluding that the photocurrent enhancements correlate to the HOMO energies of the porphyrins. The higher the energy of the HOMO, the greater the photocurrent enhancement produced by the functionalized MoS_2 films. Thus, the interfacial porphyrins significantly supress charge recombination pathways, being able to modulate both the magnitude of the photocurrent and the direction of electron flow.

[144] H. Zhang, J. Choi, A. Ramani, D. Voiry, S. N. Natoli, M. Chhowalla, D. R. McMillin, J. H. Choi, *ChemPhysChem* **2016**, *17*, 2854-2862.

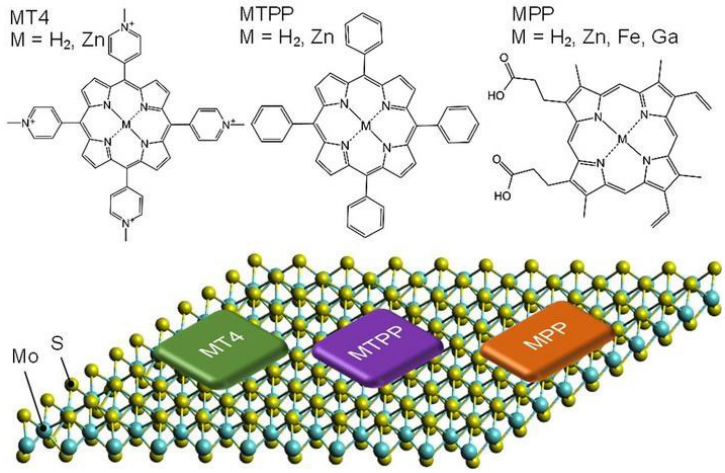

Figure 24. Eight molecules from three porphyrin families were examined for their ability to improve the light-harvesting properties of MoS_2: MT4 (tetra(*N*-methyl-4-pyridyl)porphines), MTPP (tetraphenylporphyrins), and MPP (protoporphyrins IX).

More recently, another example of assembly between porphyrins and MoS_2 nanosheets has been proposed to construct porphyrin-MoS_2 composite photoelectrocatalysts.[145] During the past few years, MoS_2-based catalysts have been considered as promising photoelectrocatalysts for the hydrogen-evolution reaction (HER) for their relatively low cost, earth abundance, high catalytic activity and good stability.[138] In this work, Xu et al. propose a dye-sensitization strategy to enhance the light-harvesting ability of MoS_2. They construct a dye-anchored 2D MoS_2 catalyst, using tetra(4-carboxyphenyl)porphyrin (TCPP) as sensitizer. The as-prepared porphyrin-MoS_2 system for photocatalytic H_2 production (Figure 25) shows a significantly enhanced photocurrent response as high as 16 μA cm^{-2}, which is about 2 times higher than that of bare MoS_2. Furthermore, the composites exhibit excellent durability when tested for 23000 s, thus providing a useful strategy for the design of highly efficient dye-sensitized photoelectrochemical catalysts.

[145] W. Wu, C. Wei, X. Lin, Q. Xu, *Chem. Asian J.* **2018**, *13*, 1293-1296.

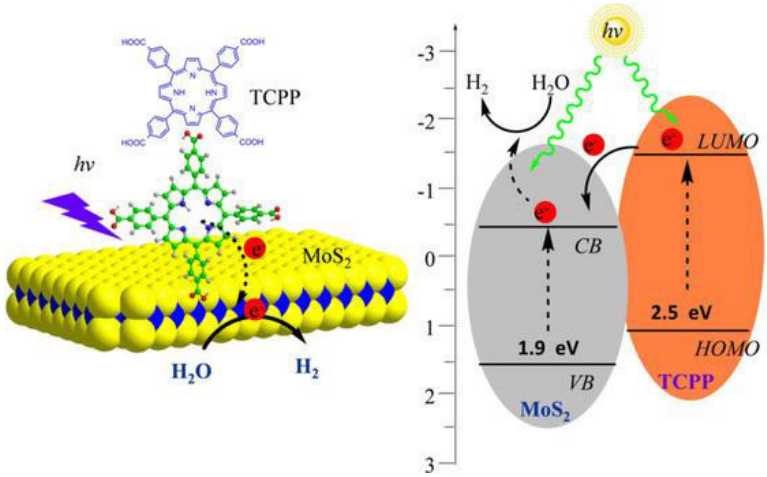

Figure 25. Schematic illustration of photocatalytic hydrogen evolution of the TCPP-MoS_2 nanosheets.

As mentioned above, in 2009 Shi's group reported a nice work about porphyrin-graphene composites and their sensing application.[130] Few years later, something similar was described by Zhao et al., but in this case using MoS_2 nanosheets. A self-assembled nanocomposite consisted of 5,10,15,20-tetrakis(1-methyl-4-pyridinio)porphyrin (TMPyP) and MoS_2 nanosheets was reported (Scheme 6).[146]

[146] W. Yin, X. Dong, J. Yu, J. Pan, Z. Yao, Z. Gu, Y. Zhao, *ACS Appl. Mater. Interfaces* **2017**, *9*, 21362-21370.

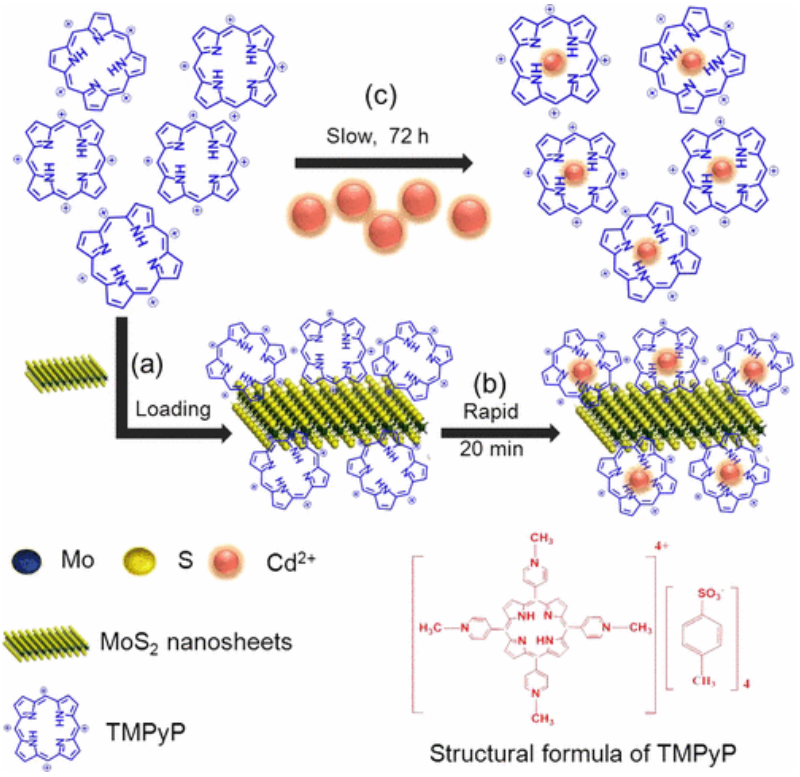

Scheme 6. Schematic illustration of the strategy based on TMPyP self-assembly with MoS_2 nanosheets for detection of Cd^{2+} ions in aqueous solution (a, b) compared with the use of pure TMPyP as probe (c).

This nanocomposite can also assist coordination of metal ions with TMPyP and be used for rapid detection of cadmium (II) ions, greatly accelerated from 72 h to 20 min with the assistance of MoS_2. Furthermore, this nanocomposite can be effectively used for removing of Cd^{2+} in water, with a removal efficiency of 91%. Thus, MoS_2-TMPyP complex can be used as other low cost, rapid and selective sensor for the detection and removal of Cd^{2+} ions in aqueous media, one of the major toxic and carcinogenic pollutants.[147]

[147] (a) A. Åkesson, B. Julin, A. Wolk, *Cancer Res.* **2008**, *68*, 6435-6441; (b) G. Jiang, L. Xu, S. Song, C. Zhu, Q. Wu, L. Zhang, L. Wu, *Toxicology* **2008**, *244*, 49-55.

2. OBJECTIVES

2. Objectives

The present thesis addresses the noncovalent functionalization of 1D and 2D nanomaterials following different chemical strategies. In particular, we have three main objectives:

- The design and synthesis of **porphyrin-based U-shaped and macrocyclic molecules** to interface them with **SWCNTs** through mechanical links.
  The **mechanically interlocked SWCNTs (MINTs)** obtained will be characterized by analytical, spectroscopic and microscopic techniques, and confirmed by a thorough spectroscopic characterization carried out by Prof. D. M. Guldi's group.

- The study of cooperative clamping interactions between **carbon nanotubes** and **hydrogen-bonded nanorings**.
  The **synergistic relationship** established will be analyzed by theoretical, spectroscopic and microscopic techniques, proving also the recovery of pristine SWCNTs. The dinucleoside monomer that is able to self-assemble in nanorings will be prepared by Dr. D. González-Rodríguez's group.

- The combination of **molecular dyes** (PDI and TPP) with **MoS_2 photodetectors** for the modulation of their optoelectronic properties.
  The resulting **noncovalent functionalization** will be evaluated through electronic and optoelectronic techniques, demonstrating also the reproducibility and reversibility of the process. This characterization will be carried out in collaboration with Dr. A. Castellanos-Gomez's group.

3. INTERFACING PORPHYRINS AND CARBON NANOTUBES THROUGH MECHANICAL LINKS

3. Interfacing porphyrins and carbon nanotubes through mechanical links

We describe the synthesis of rotaxane-type species composed of macrocyclic porphyrin rings mechanically interlocked with SWCNT threads. The formation of mechanically interlocked SWCNTs (MINTs) proceeds with chiral selectivity, and was confirmed by spectroscopic and analytical techniques and adequate control experiments, and corroborated by high-resolution electron microscopy. From a thorough characterization of the MINTs through UV-vis-NIR absorption, fluorescence, Raman and transient absorption spectroscopy we analyse in detail the electronic interactions of the porphyrins and the SWCNTs in the ground and excited states.

Chem. Sci. **2018**, *9*, 6779-6784.

3.1. Introduction

The ability of metalloporphyrins to reversibly coordinate gases is exploited by Nature in the transport of oxygen by the heme group. Directly related to this is another main biological function of porphyrinoid structures, that is, as co-factors in cytochrome P450, which is responsible for many catalytic redox reactions. Finally, the intense absorption in the visible region and the ability to accept electrons upon photoexcitation of the structurally related chlorophylls renders them ideal light antennas and primary electron acceptors in photosynthesis. Inspired by these crucial roles, porphyrins are one of the most extensively studied organic

chromophores.[1,2,3,4,5] A particularly active area of research is the combination of porphyrins and carbon nanotubes (CNTs), which also benefits from the extraordinary physical properties of CNTs.[6,7,8,9] Porphyrin-CNT hybrids have been successfully applied to the fabrication of bioinspired high-performance gas sensors,[10,11] catalysts,[12,13,14,15] model photosynthetic systems,[16,17,18] and other optoelectronic devices.[19] The physical properties of all these artificial systems depend crucially on the nature of the linker between them.

A covalent porphyrin-CNT connection typically leads to good kinetic stability, and the structure of the spacer can be used to modulate porphyrin-CNT communication.[20,21,22] Interfacing porphyrins and CNTs *via* non-covalent interactions provides an alternative means to generate porphyrin-CNT

[1] L.-L. Li, E. W.-G. Diau, *Chem. Soc. Rev.* **2013**, *42*, 291-304.
[2] M. Ethirajan, Y. Chen, P. Joshi, R. K. Pandey, *Chem. Soc. Rev.* **2011**, *40*, 340-362.
[3] J. A. A. W. Elemans, R. van Hameren, R. J. M. Nolte, A. E. Rowan, *Adv. Mater.* **2006**, *18*, 1251-1266.
[4] J. L. Sessler, D. Seidel, *Angew. Chem. Int. Ed.* **2003**, *42*, 5134-5175.
[5] D. M. Guldi, *Chem. Soc. Rev.* **2002**, *31*, 22-36.
[6] T. Umeyama, H. Imahori, *J. Phys. Chem. C* **2013**, *117*, 3195-3209.
[7] D. M. Guldi, R. D. Costa, *J. Phys. Chem. Lett.* **2013**, *4*, 1489-1501.
[8] M. F. L. De Volder, S. H. Tawfick, R. H. Baughman, A. J. Hart, *Science* **2013**, *339*, 535-539.
[9] N. Karousis, N. Tagmatarchis, D. Tasis, *Chem. Rev.* **2010**, *110*, 5366-5397.
[10] S. F. Liu, A. R. Petty, G. T. Sazama, T. M. Swager, *Angew. Chem. Int. Ed.* **2015**, *54*, 6554-6557.
[11] S. F. Liu, L. C. H. Moh, T. M. Swager, *Chem. Mater.* **2015**, *27*, 3560-3563.
[12] A. Maurin, M. Robert, *J. Am. Chem. Soc.* **2016**, *138*, 2492-2495.
[13] P.-J. Wei, G.-Q. Yu, Y. Naruta, J.-G. Liu, *Angew. Chem. Int. Ed.* **2014**, *53*, 6659-6663.
[14] I. Hijazi, T. Bourgeteau, R. Cornut, A. Morozan, A. Filoramo, J. Leroy, V. Derycke, B. Jousselme, S. Campidelli, *J. Am. Chem. Soc.* **2014**, *136*, 6348-6354.
[15] S. Jayakumar, H. Li, J. Chen, Q. Yang, *ACS Appl. Mater. Interfaces* **2018**, *10*, 2546-2555.
[16] Q. Zhong, V. V. Diev, S. T. Roberts, P. D. Antunez, R. L. Brutchey, S. E. Bradforth, M. E. Thompson, *ACS Nano* **2013**, *7*, 3466-3475.
[17] H. Imahori, T. Umeyama, K. Kurotobi, Y. Takano, *Chem. Commun.* **2012**, *48*, 4032-4045.
[18] L. M. Arellano, M. Barrejon, H. B. Gobeze, M. J. Gomez-Escalonilla, J. L. G. Fierro, F. D'Souza, F. Langa, *Nanoscale* **2017**, *9*, 7551-7558.
[19] G. Delport, F. Vialla, C. Roquelet, S. Campidelli, C. Voisin, J.-S. Lauret, *Nano Lett.* **2017**, *17*, 6778-6782.
[20] T. Palacin, H. L. Khanh, B. Jousselme, P. Jegou, A. Filoramo, C. Ehli, D. M. Guldi, S. Campidelli, *J. Am. Chem. Soc.* **2009**, *131*, 15394-15402.
[21] D. M. Guldi, H. Taieb, G. M. A. Rahman, N. Tagmatarchis, M. Prato, *Adv. Mater.* **2005**, *17*, 871-875.
[22] D. M. Guldi, G. M. A. Rahman, M. Prato, N. Jux, S. Qin, W. Ford, *Angew. Chem. Int. Ed.* **2005**, *44*, 2015-2018.

hybrids.[23,24,25,26,27,28,29] The intrinsic porphyrin-CNT non-covalent interactions have been skilfully exploited to associate and purify single-walled CNTs (SWCNTs) in a chirality and enantioselective fashion.[30,31,32,33,34]

Mechanically interlocked molecules (MIMs) are composed of covalent components linked together by their topology. Rotaxanes are prototypical examples of MIMs, in which one or more macrocycles are linked to a dumbbell-shaped linear component: the thread. The mechanical bond imparts MIMs with unique dynamic properties.[35,36] Specifically, the macrocycles can be moved along or around the thread through controlled submolecular motion. This is a key step for the construction of some of the most advanced examples of synthetic molecular machines.[37,38,39]

We have developed methods to thread SWCNTs through macrocycles to form rotaxane-like mechanically interlocked nanotube derivatives (MINTs) using a

[23] G. Bottari, O. Trukhina, M. Ince, T. Torres, *Coord. Chem. Rev.* **2012**, *256*, 2453-2477.
[24] F. D'Souza, O. Ito, *Chem. Commun.* **2009**, 4913-4928.
[25] S. Fukuzumi, T. Kojima, *J. Mater. Chem.* **2008**, *18*, 1427-1439.
[26] L. Rodriguez-Pérez, S. Vela, C. Atienza, N. Martin, *Org. Lett.* **2017**, *19*, 4810-4813.
[27] J. Lopez-Andarias, S. H. Mejias, T. Sakurai, W. Matsuda, S. Seki, F. Feixas, S. Osuna, C. Atienza, N. Martin, A. L. Cortajarena, *Adv. Funct. Mater.* **2018**, *28*, 1704031.
[28] C. Ehli, G. M. A. Rahman, N. Jux, D. Balbinot, D. M. Guldi, F. Paolucci, M. Marcaccio, D. Paolucci, M. Melle-Franco, F. Zerbetto, S. Campidelli, M. Prato, *J. Am. Chem. Soc.* **2006**, *128*, 11222-11231.
[29] K. S. Chichak, A. Star, M. V. P. Altoé, J. F. Stoddart, *Small* **2005**, *1*, 452-461.
[30] G. Liu, F. Wang, S. Chaunchaiyakul, Y. Saito, A. K. Bauri, T. Kimura, Y. Kuwahara, N. Komatsu, *J. Am. Chem. Soc.* **2013**, *135*, 4805-4814.
[31] A. F. M. M. Rahman, F. Wang, K. Matsuda, T. Kimura, N. Komatsu, *Chem. Sci.* **2011**, *2*, 862-867.
[32] X. Peng, N. Komatsu, T. Kimura, A. Osuka, *ACS Nano* **2008**, *2*, 2045-2050.
[33] X. Peng, N. Komatsu, T. Kimura, A. Osuka, *J. Am. Chem. Soc.* **2007**, *129*, 15947-15953.
[34] X. Peng, N. Komatsu, S. Bhattacharya, T. Shimawaki, S. Aonuma, T. Kimura, A. Osuka, *Nat. Nanotechnol.* **2007**, *2*, 361-365.
[35] R. S. Forgan, J.-P. Sauvage, J. F. Stoddart, *Chem. Rev.* **2011**, *111*, 5434-5464.
[36] J. F. Stoddart, *Chem. Soc. Rev.* **2009**, *38*, 1802-1820.
[37] J. F. Stoddart, *Angew. Chem. Int. Ed.* **2017**, *56*, 11094-11125.
[38] J.-P. Sauvage, *Angew. Chem. Int. Ed.* **2017**, *56*, 11080-11093.
[39] D. A. Leigh, *Angew. Chem. Int. Ed.* **2016**, *55*, 14506-14508.

clipping strategy.[40] More recently, groups led by Kruss,[41] and Miki and Ohe,[42] have described the encapsulation of SWCNTs into peptide barrels and rigid cycloparaphenyleneacetylenes, respectively. The native structure of SWCNTs is preserved upon formation of MINTs, while the extreme aspect ratio of SWCNTs prevent the macrocycles from dissociating, providing MINTs with a kinetic stability comparable to that of covalently functionalized SWCNTs.[43,44,45] We have also documented that MINTs feature unique physical properties, which are quite different from classic supramolecular SWCNT derivatives.[46,47]

Here, we interface porphyrins and SWCNTs through mechanical links. The MINT-forming reaction proceeds with chiral selectivity for the smaller diameter SWCNTs. The electronic interactions between the porphyrins and the nanotubes in the ground state, as well as the charge separation and recombination processes and their underlying dynamics upon photoexcitation are also described in detail.

3.2. Results and Discussion

It should be noted that the chemical structure of the U-shaped porphyrin synthesized (**U-por** in Figure 1) is a bit different with respect to other U-shaped molecules we have previously used in the synthesis of MINTs. Specifically, we

[40] E. M. Pérez, *Chem. Eur. J.* **2017**, *23*, 12681-12689.
[41] F. A. Mann, J. Horlebein, N. F. Meyer, D. Meyer, F. Thomas, S. Kruss, *Chem.-Eur. J.* **2018**, *24*, 12241-12245.
[42] K. Miki, K. Saiki, T. Umeyama, J. Baek, T. Noda, H. Imahori, Y. Sato, K. Suenaga, K. Ohe, *Small* **2018**, *14*, 1800720.
[43] S. Leret, Y. Pouillon, S. Casado, C. Navio, A. Rubio, E. M. Pérez, *Chem. Sci.* **2017**, *8*, 1927-1935.
[44] A. Lopez-Moreno, E. M. Pérez, *Chem. Commun.* **2015**, *51*, 5421-5424.
[45] A. de Juan, Y. Pouillon, L. Ruiz-Gonzalez, A. Torres-Pardo, S. Casado, N. Martin, A. Rubio, E. M. Pérez, *Angew. Chem. Int. Ed.* **2014**, *53*, 5394-5400.
[46] A. López-Moreno, B. Nieto-Ortega, M. Moffa, A. de Juan, M. M. Bernal, J. P. Fernández-Blázquez, J. J. Vilatela, D. Pisignano, E. M. Pérez, *ACS Nano* **2016**, *10*, 8012-8018.
[47] E. Martinez-Perinan, A. de Juan, Y. Pouillon, C. Schierl, V. Strauss, N. Martin, A. Rubio, D. M. Guldi, E. Lorenzo, E. M. Pérez, *Nanoscale* **2016**, *8*, 9254-9264.

change the spacer between the two recognition units. In our previous samples, we linked the recognition units through a 1,4-xylylene spacer.[40] However, using these porphyrin units as recognition motifs for SWCNTs, we observed that the macrocycle cannot be formed, even testing C_{10}, C_{14} and C_{18} alkenyl spacers. This experimental observation was attributed to an unexpected rigid behavior for the aromatic spacer. Molecular mechanics calculations confirm that, in this case, the central p-xylylene spacer behaves fundamentally as a rigid unit.

For this reason, and in order to increase the flexibility of the ring, we have used an alkyl spacer of similar size, 1,6-dibromohexane, to synthesize the U-shaped porphyrin. With this more flexible spacer, we indeed succeed in the synthesis of the corresponding porphyrin-macrocycle.

Thus, we focused on a U-shaped molecule equipped with two porphyrin recognition units for SWCNTs and synthesized as shown in Scheme 1.

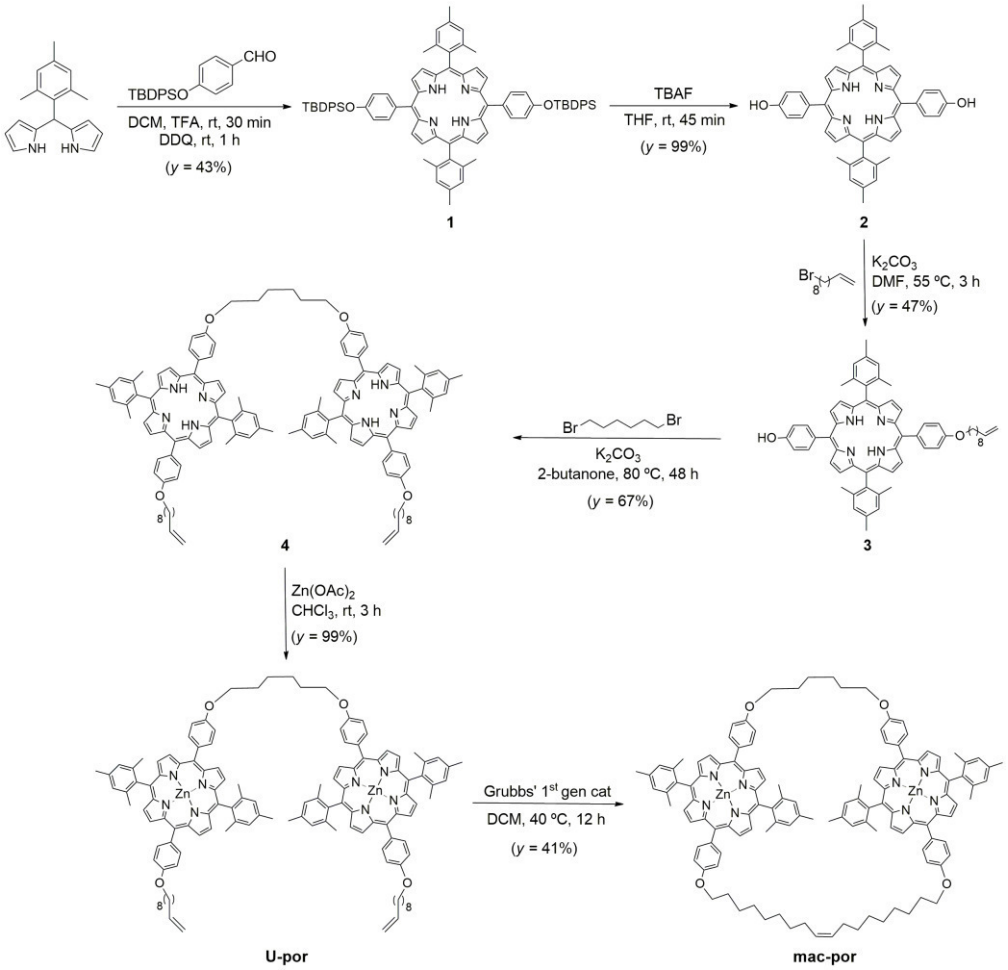

Scheme 1. General scheme of synthesis of **U-por** and **mac-por**.

First, it is important to note that the sterically demanding 2,4,6-trimethylphenyl moiety present as a substituent of the bis(1*H*-pyrrole)methane was deliberately chosen due to its ability to afford *meso* substituted porphyrins without scrambling, thus avoiding the formation of a complicated mixture of porphyrins. This 5-(mesityl)dipyrrylmethane was condensed with 4-((tert-butyldiphenylsilyl)oxy)benzaldehyde, previously synthesized, to get the starting porphyrin **1**. After quantitative deprotection of the two phenol groups, a

monoalkylation reaction takes place by a Williamson's etherification from the dihydroxyphenyl porphyrin **2**, providing the porphyrin with an alkenyl chain **3**. These recognition units were then linked together through a hexamethylene spacer, which provides flexibility to template the macrocyclization around SWCNTs, getting the linear precursor **4**. The last step was the metalation of the porphyrin with zinc acetate, in order to avoid problems in the synthesis of the macrocycle with Grubbs' catalyst, obtaining the final U-shaped porphyrin (**U-por**). The porphyrin-macrocycle (**mac-por**) was synthesized by ring-closing metathesis (RCM) of the terminal alkenes of the **U-por**. The synthetic details and full characterization of each molecule is describe in the Experimental Section.

We then explored the formation of **MINT-por** through templated RCM of **U-por** in the presence of (6,5)-enriched SWCNTs. The diameter of the latter is 0.75 nm, which is a good fit for the cavity of **mac-por**, as shown by the energy-minimized molecular structure (HF-3c)[48] shown in Figure 1B. SWCNTs (2 mg) were suspended in tetrachloroethane (TCE, 2 mL) through sonication and mixed with **U-por** (4.2 mM) and Grubbs' 2nd generation catalyst at room temperature (rt) for 72 hours.

[48] R. Sure, S. Grimme, *J. Comput. Chem.* **2013**, *34*, 1672-1685.

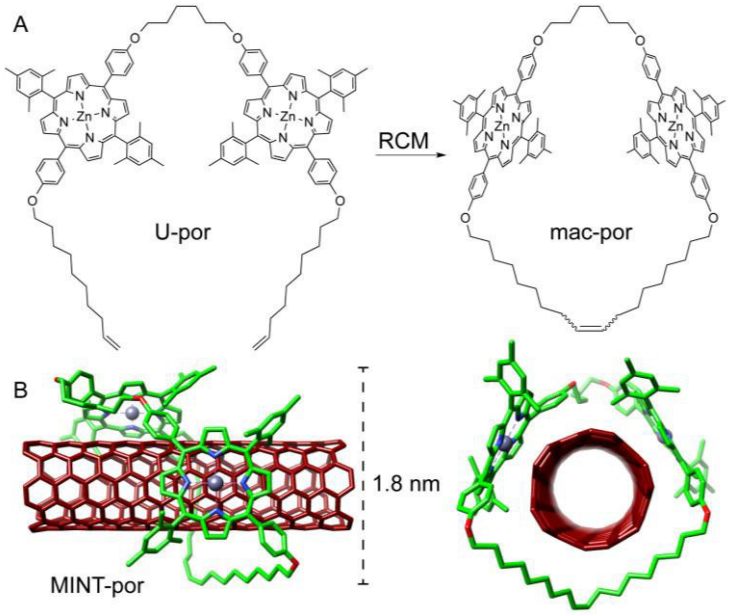

Figure 1. (A) Chemical structures of **U-por** and **mac-por**. (B) Side and front view of the energy-minimized structure (HF-3c) of **MINT-por**, showing the diameter of the macrocycle. C atoms in green (**mac-por**) or dark red (SWCNT), N in blue, O in red, Zn in metallic gray. H atoms omitted for clarity.

Next, the suspension was filtered through a polytetrafluoroethylene membrane with a pore size of 0.2 µm and washed with dichloromethane (DCM) to remove non-threaded macrocycles, catalyst and any remaining linear precursors. Three resuspension-filtration iterations complete the purification. Hereafter, the samples were dried and subjected to thermogravimetric analysis (TGA) to quantify the degree of functionalization. TGA showed a weight loss of 24% at around 340 °C, corresponding to the porphyrinic material (Figure 2A). We performed experiments in which the concentration of **U-por** was varied between 1.06 and 8.4 mM to modulate the degree of functionalization. The product formed at the lowest concentration of the U-shaped precursor showed a loss of 10% at 340 °C, whereas

a weight loss of 26% was observed for the highest concentration (Figure 2B).[49] In addition, the derivative of the TGA data features a single peak for the porphyrinic material, confirming that oligomers of **U-por** adsorbed onto SWCNTs are absent in **MINT-por**.[43,50,51]

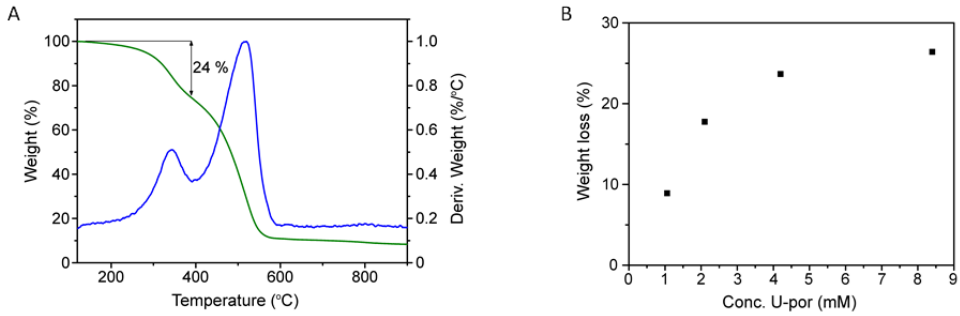

Figure 2. (A) TGA (air, 10 °C min^{-1}) of **MINT-por**. Note that the derivative shows a single peak for the porphyrinic material, indicating little or no participation of oligomers in the functionalization. (B) Degree of functionalization of **MINT-por** samples from TGA: relative weight loss versus concentration of linear precursor.

To test the stability of **MINT-por**, we heated the samples for 30 min under reflux in TCE (bp = 147 °C), followed by a thorough rinse with DCM. TGA of the resulting samples showed a subtle decrease of 3% in functionalization confirming the MINT stability.

[49] A plot of the degree of functionalization *vs.* [**U-por**]$_0$ shows that the degree of functionalization does not have a linear relationship with the concentration of linear precursor, but instead shows a square hyperbolic shape, reminiscent of a 1:1 binding isotherm, reaching a maximum at about 30%. Control experiments in which we mixed **U-por** with (6,5)-SWCNTs without Grubbs' catalyst, under otherwise identical conditions to the MINT reaction, yielded much lower functionalization (7%).

[50] A. de Juan, M. M. Bernal, E. M. Pérez, *ChemPlusChem* **2015**, *80*, 1153-1157.

[51] These data taken together further prove that the supramolecular functionalization of the nanotubes by **U-por**, **mac-por** and/or linear oligomers formed *in situ* is minoritary.

Investigations of **MINT-por** by means of atomic force microscopy (AFM) and transmission electron microscopy (TEM) corroborate the presence of rotaxane-type species. Figure 3A shows a typical AFM topographic image of a spin-casted TCE suspension of **MINT-por**. Individualized SWCNTs with heights around 0.8 nm decorated with objects that are consistently around 2.0 nm high, are in sound agreement with **mac-por** around a SWCNT (Figure 1B). Macrocycles adsorbed onto SWCNTs rather than threaded by SWCNTs are expected to show a significantly smaller height.

Aberration corrected-high resolution TEM (AC-HRTEM) images further confirm the rotaxane-like structure of **MINT-por**. They were drop-casted from an isopropanol suspension onto copper grids and reveal mostly bundled SWCNTs with functionalized sidewalls. These co-exist, however, with isolated SWCNTs of 0.8 nm diameter, in which single circular objects of a size of *ca.* 1.8 nm are discernable. A representative AC-HRTEM micrograph of **MINT-por** with close to atomic resolution is shown in Figure 3B, which shows a SWCNT with a diameter of 0.85 nm, surrounded by a macrocycle that shows a diameter of 1.77 nm. In contrast to our previous MINTs, in which we observed macrocycle-like rings around SWCNTs,[40] the large dimensions of the porphyrins, in the range of 1.4-1.8 nm, comparable to the diameter of the macrocycle, confer the macrocycles a box-like shape. We note that the distances between the macrocycle and the SWCNT sidewalls correspond to very close van der Waals contacts (< 0.4 nm). Finally, from the difference in contrast between the SWCNT walls we conclude that **mac-por** is threaded by SWCNTs rather than physisorbing on them. We note that, even under these low voltage conditions, the sample is eventually damaged under the e-beam, most likely starting with the

more sensitive C-H bonds of the alkyl chain,[52] but eventually damaging even the SWCNT wall (see Figure 4).

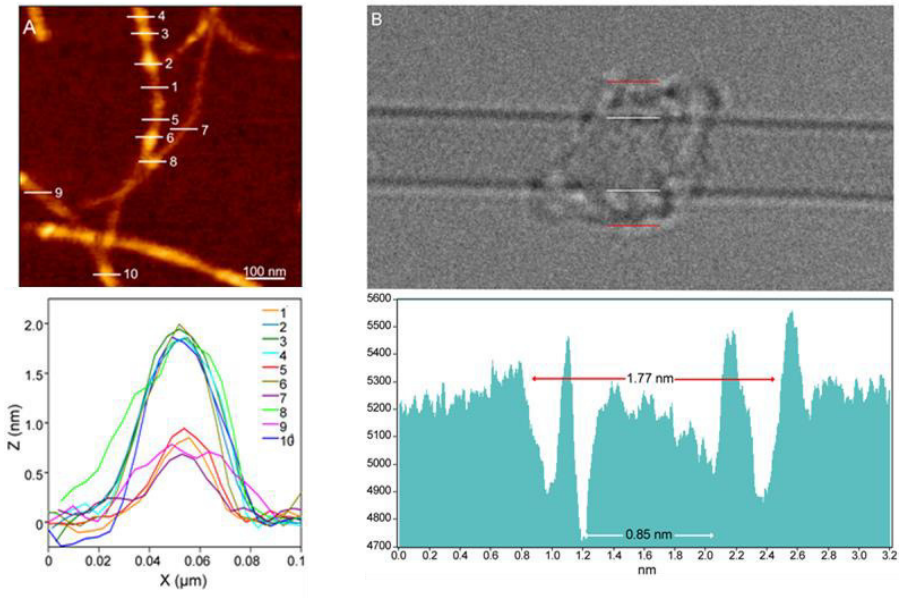

Figure 3. (A) AFM topographic image of a suspension of **MINT-por** in TCE and corresponding height profiles along the lines marked in the topographic image. (B) AC-HRTEM image of an individual SWCNT functionalized by a single macrocycle in **MINT-por** and corresponding profiles (white lines and arrows mark SWCNT diameter, red lines and arrows mark **mac-por** diameter).

[52] S. T. Skowron, T. W. Chamberlain, J. Biskupek, U. Kaiser, E. Besley, A. N. Khlobystov, *Acc. Chem. Res.* **2017**, *50*, 1797-1807.

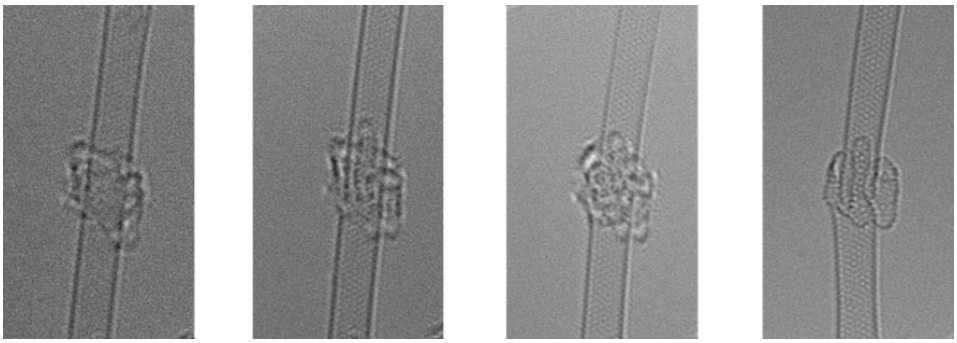

Figure 4. Modification of **mac-por**, and even the SWCNT wall, during TEM imaging due to the impact of the e-beam (60 kV).

To gain insights into the electronic properties of **MINT-por**, we carried out UV-vis-NIR, fluorescence and Raman spectroscopy measurements. Steady state absorption spectra (D_2O/SDBS (1 wt%, rt)) of (6,5)-enriched SWCNTs (black) and the corresponding MINTs (red) are compared in Figure 5A. In the **MINT-por** sample, the Soret-band absorption of the porphyrins is evident at 430 nm. As far as the absorption spectra of (6,5)-enriched SWCNTs are concerned, S_{22} transitions are noted in the visible region, while the S_{11} transitions dominate the nIR region. In particular, (6,5)-SWCNT related maxima appear at 570 and 981 nm. Features of (7,5)-SWCNTs are seen at 649 and 1022 nm, whereas those of (7,6)-SWCNTs evolve at 664 and 1136 nm. In **MINT-por**, all of the aforementioned features are red-shifted to 572, 982, 652, 1022, 664 and 1137 nm, on one hand, and broadened, on the other hand. From the aforementioned we conclude weak electronic interactions between SWCNTs and the porphyrin in the ground state. When turning to the porphyrin absorption spectrum, the Soret-band absorption maximizes at 429 nm in DMF for **MINT-por** as well as for **U-por** (Figures 5B and S1 in the Experimental Section).[53]

[53] In DMF rather than D_2O/SDBS a blue-shift of the S_{11} transitions for **MINT-por** relative to SWCNTs indicates a better debundling of SWCNTs.

To probe the chirality selectivity during the MINT formation,[47] the relative absorption intensities in dispersions of pristine SWCNTs and **MINT-por** are inspected. A look at, for example, the (6,5)-SWCNTs features in the nIR region reveals that the relative intensity is higher for SWCNTs than for **MINT-por**. The trend is reversed for (7,5)-SWCNTs. Implicit is a chiral selectivity of the MINT formation based on different SWCNT diameters.

To shed light on the excited state interactions in **MINT-por**, the SWCNT fluorescence was analyzed in the nIR-region (Figures 5C and D). In spectra of SWCNT and **MINT-por**, characteristic fluorescence features of (8,3), (6,5), (7,5), (8,4) and (7,6)-SWCNTs are present. At first glance, the fluorescence features of pristine SWCNTs at 967, 988, 1031, 1127 and 1130 nm are, in line with the steady state absorption measurements, red-shifted in **MINT-por**; the new maxima are at 967, 993, 1034, 1130 and 1132 nm. A closer look at the fluorescence spectra shown in Figure S2 in the Experimental Section reveals quenching, which is stronger for small diameter SWCNTs, that is, (8,3)-, (6,5)- and (7,5)-SWCNT, than for larger diameter SWCNTs, that is, (8,4)- and (7,6)-SWCNT. A possible rationale is a higher degree of functionalization in the case of smaller diameter SWCNTs in comparison to their larger diameter analogues. Quenching, although moderate in nature, was also observed for the porphyrin fluorescence (Figure S1 in the Experimental Section). Quenching in **MINT-por** is likely to stem from deactivation pathways such as energy or electron transfer, which compete with the fluorescent decay.

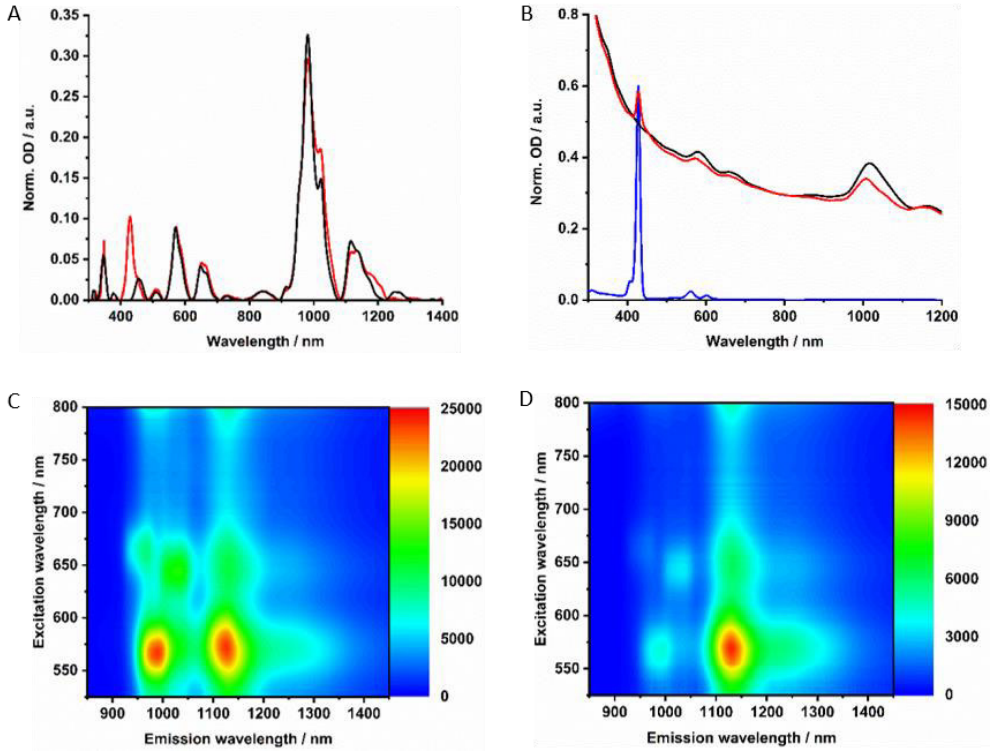

Figure 5. Normalized absorption spectra of (6,5)-enriched SWCNTs (black), **MINT-por** (red) and **U-por** (blue) in (A) D_2O/SDBS (1 wt%, rt), baseline-corrected and normalized to the (7,6)-SWCNT absorption at 1136 nm and (B) DMF (rt). 3D nIR fluorescence spectra of (C) (6,5)-enriched SWCNTs and (D) **MINT-por**, in D_2O/SDBS (1 wt%, rt) with OD of 0.21 at 570 nm.

Electronic interactions as seen in the excited state might also impact the Raman features. To this end, about 1000 Raman spectra were taken for each sample (Figure 6). They show small up-shifts of the D-, G- and 2D-modes from 1298, 1584 and 2589 cm^{-1} for (6,5)-enriched SWCNTs to 1302, 1590 and 2595 cm^{-1} for **MINT-por**. For **MINT-por** the up-shifts indicate weak charge-transfer interactions, which relate to a donating of charge density from the porphyrin to the SWCNTs.

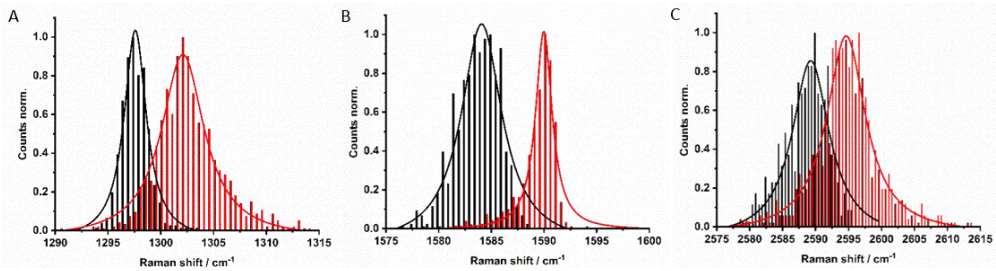

Figure 6. Raman histograms of (A) D-mode, (B) G-mode, and (C) 2D-mode of drop-casted SWCNTs (black) and **MINT-por** (red) from methanol, with 633 nm laser excitation.

Raman spectroscopy is also a powerful tool to investigate chiral selectivity. To this end, the focus was on the low frequency radial breathing modes (RBM), which are unique for each SWCNT chirality (see Figure S3 in the Experimental Section). Here, signals appear at about 255, 282 and 303 cm^{-1}, which stem from (7,6)-, (7,5)- and (6,5)-SWCNTs, respectively. Well in line with the results from absorption and fluorescence measurements, the relative intensity of (7,5)-SWCNTs is higher in **MINT-por** than in the pristine sample of SWCNTs. Important is the fact that no significant changes were noted in the I_D/I_G ratios when comparing (6,5)-enriched SWCNTs (0.12) with **MINT-por** (0.14). This confirms the absence of defect introduction during the functionalization.

Notable quenching in the fluorescence measurements prompted us to perform femtosecond transient absorption measurements (Figures 7 and S4 in the Experimental Section). At first glance, the spectra of (6,5)-enriched SWCNTs and **MINT-por** are dominated by an immediate ground state bleaching of SWCNTs in the nIR-region. Hereby, the nIR bleachings mirror image the steady state absorption spectra. In stark contrast, contributions from the porphyrins in **MINT-por** in the visible region are not discernable as they are masked by the much stronger SWCNT features. A closer look reveals that for (6,5)-enriched SWCNTs minima evolve at 568, 648, 667, 983 and 1121 nm, while maxima appear at 484, 531, 612, 927, 1073, 1211

and >1300 nm. In **MINT-por**, the same features are discernable but red-shifted to 569, 650, 669, 986 and 1121 nm in the case of the minima and to 490, 535, 617, 927, 1076, 1215 and >1300 nm in the case of the maxima. A three exponential fitting procedure of the ground state recovery of (6,5)-, (7,5)-, (8,4)- and (7,6)-SWCNTs yielded three different lifetimes, which differ for each SWCNT chirality (Table S1 in the Experimental Section). In SWCNTs, the long-lived component relates to radiative exciton recombination, while the two short-lived components stem from interband- and intertube relaxations. In **MINT-por**, all lifetimes are markedly shorter. Interestingly, smaller diameter (6,5)- and (7,5)-SWCNTs, which are subjective to the strongest fluorescence quenching, give rise to the fastest recovery. The long-lived component is decreased in, for example, (6,5)-SWCNTs by 32% and by 52% for (7,5)-SWCNTs. In stark contrast, in larger diameter (8,4)- and (7,6)-SWCNTs the decrease of the long-lived component is only 15% and 12%, respectively.[54] We conclude that charge separation in **MINT-por** with 5 ps for (6,5)-SWCNT and 4 ps for (7,5)-SWCNT is followed by charge recombination with 78 and 81 ps, respectively. In the case of larger diameter SWCNTs, both charge separation and recombination are less favored: the corresponding lifetimes are 4 and 72 ps for (8,4)- as well as 3 and 52 ps for (7,6)- SWCNTs.

[54] Notably, we lack unambiguous proofs for the formation of the one-electron oxidized porphyrin, but we presume, as a sum of all spectroscopic evidence, charge transfer in small diameter SWCNTs. Here, the low intensity porphyrin transients, on one hand, and the strong SWCNT transients, on the other hand, are largely responsible for the lack of detection.

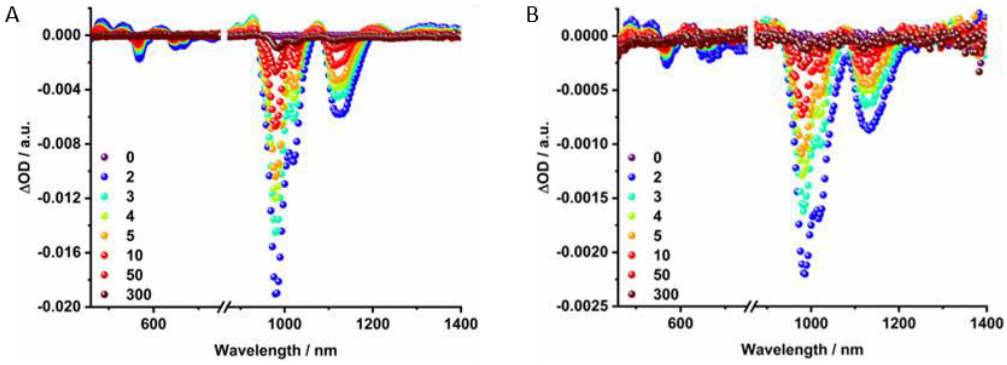

Figure 7. Differential absorption spectra of (A) (6,5)-enriched SWCNTs and (B) **MINT-por** obtained upon femtosecond pump probe experiments following 420 nm laser excitation in D_2O/SDBS (1 wt%, rt) at several time delays between 0 and 300 ps.

3.3. Conclusions

In the current study, we have documented the interfacing of porphyrin chromophores and SWCNTs *via* mechanical interlocking, through the synthesis of rotaxane-type architectures. Formation of MINTs is confirmed *via* adequate control experiments, analytical, spectroscopic and microscopic techniques. Besides TGA, the threading of the macrocycles with SWCNTs to form MINTs without introducing SWCNT defects was confirmed by means of AFM, AC-HRTEM and Raman spectroscopy. Moreover, from Raman and steady state absorption spectroscopy we concluded the selective functionalization of smaller diameter SWCNTs. In line with chiral selectivity, electronic interactions, which are intense between the porphyrin rings and SWCNTs of smaller diameters, are probably the most important factor. Transient absorption spectroscopy proved also to be very important to detect charge separation and recombination in **MINT-por** and to dissect the underlying dynamics. We are currently exploring the consequences that this entirely novel

approach to connect porphyrins and SWCNTs has on applications such as catalysis, magnetism and sensing.[55,56]

3.4. Experimental Section

General. All solvents were dried according to standard procedures. Reagents were used as purchased. All air-sensitive reactions were carried out under argon atmosphere. Column chromatography was performed using silica gel (Scharlau 60, 70-230 mesh) or aluminium oxide (Merck 90, standardized). Analytical thin layer chromatographies (TLC) were performed using aluminium-coated Macherey-Nagel silica gel 60 F254 plates or aluminium-coated Macherey-Nagel aluminium oxide F254 plates. NMR spectra were recorded on a BrukerAvance 400 (^{1}H: 400 MHz; ^{13}C: 101 MHz) spectrometer at 298 K, unless otherwise stated, using partially deuterated solvents as internal standards. Coupling constants (*J*) are denoted in Hz and chemical shifts (δ) in ppm. Multiplicities are denoted as follows: s = singlet, d = doublet, t = triplet, m = multiplet, b = broad. Fast atom bombardment (FAB) and matrix-assisted laser desorption ionization (coupled to a Time-Of-Flight analyser) (MALDI-TOF) experiments were recorded on a VG AutoSpec spectrometer and a Bruker REFLEX spectrometer, respectively. Thermogravimetric analyses (TGA) were performed using a TA Instruments TGAQ500 with a ramp of 10 °C/min under air from 100 to 1000 °C. UV-vis-NIR spectra were performed using a Cary 5000 spectrometer (Varian) and 10x10 mm quartz cuvettes. Photoluminescence excitation intensity maps (PLE) were obtained with a FluoroLog 3 spectrometer from HORIBA Yobin Yvon using a 450 W Xenon lamp and a Symphony InGaAs array in combination with an iHR320 imaging spectrometer. For the visible range, a

[55] V. Sgobba, G. M. A. Rahman, D. M. Guldi, N. Jux, S. Campidelli, M. Prato, *Adv. Mater.* **2006**, *18*, 2264-2269.
[56] D. M. Guldi, V. Sgobba, *Chem. Commun.* **2011**, *47*, 606-610.

Fluoromax3 spectrometer from HORIBA Yobin Yvon was used. Femtosecond transient absorption measurements were performed with the transient absorption pump probe system HELIOS from Ultrafast Systems. For the generation of laser pulses with a pulse width of 150 fs a CPA-2110 titanium:sapphire laser system from Clark-MXR Inc was used (output 775 nm, 1 kHz). The 420 nm excitation pulses were generated by using a noncollinear optical parametric amplifier (NOPA, Clark MXR). All pump probe measurements were carried out in 2 mm OS quartz cuvettes. Raman spectra were acquired with a WiTec alpha300r confocal Raman microscope. Samples were deposited onto silica wafers by drop casting. A HeNe laser with an output of 633 nm was used for sample excitation. Atomic force microscopy (AFM) images were obtained with JPK NanoWizard II instrument, coupled to an inverted optical microscope Nikon Eclipse Ti-U. High resolution-transmission electron microscopy (HR-TEM) images were obtained in an imaging aberration corrected microscope JEM GRAND ARM300cF JEOL, operating at 60 kV in order to minimize the electron beam damage. Images were recorded on a slow-CCD camera GATAN Oneview. The optimized structure of **MINT-por** has been obtained using the Grimme's 3-corrected Hartree-Fock method (HF-3c). A quantum chemical method based on a Hartree-Fock calculation with a small Gaussian AO basis set present. This methodology has been developed to apply HF calculation to large systems. The main idea is to correct for some of the systematic deficiencies of a small basis Hartree-Fock calculation (instead of approximating HF) and use as a very fast QM method. It is also in many ways a better alternative to a minimal basis DFT method as there is no numerical integration involved. HF-3c has been defined for elements H-Xe with ECPs automatically used for the heavier elements.[48]

Synthetic details and characterization

Synthesis of compound **1**. 5-(mesityl)dipyrrylmethane (300 mg, 1.14 mmol) and 4-((tert-butyldiphenylsilyl)oxy)benzaldehyde (409 mg, 1.14 mmol) were dissolved in DCM (120 mL), and then TFA (163 µL, 2.12 mmol) was added slowly. The reaction was stirred at room temperature. After 30 min, DDQ (258 mg, 1.14 mmol) was added, and the reaction mixture was stirred at room temperature for a further 1 h. The complete reaction mixture was poured onto a pad of alumina and eluted with DCM until the eluting solution was pale brown. The solvent was removed under vacuum to give a dark solid which was dissolved in toluene (30 mL) and heated under reflux for 1 h in the presence of DDQ (258 mg, 1.14 mmol) to oxidize any remaining chlorin. After cooling to room temperature, the solvent was removed under vacuum and the crude product was purified by column chromatography (aluminium oxide, hexane/toluene 7:3). Removal of the solvent under vacuum gave a purple solid. The compound **1** (296 mg, 43%) was characterized by ^{1}H, ^{13}C -NMR, MALDI and UV/vis.

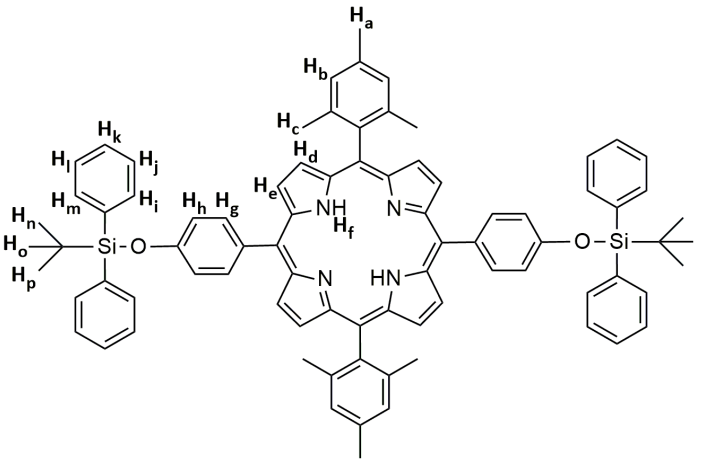

Compound **1**. ^{1}H NMR (400 MHz, $CDCl_3$) δ 8.74 (d, *J* = 4.7 Hz, 4H, H_e), 8.67 (d, *J* = 4.7 Hz, 4H, H_d), 7.95 – 7.92 (m, 12H, $H_{i,j,g}$), 7.54 – 7.48 (m, 12H, $H_{k,l,m}$), 7.29 (s, 4H, H_b), 7.14 (d, *J* = 8.6 Hz, 4H, H_h), 2.65 (s, 6H, H_a), 1.83 (s, 12H, H_c), 1.29 (s, 18H, $H_{n,o,p}$), -2.66 (s, 2H, H_f). ^{13}C NMR (101 MHz, $CDCl_3$) δ 155.6, 139.5, 138.6, 137.7, 135.8, 135.3, 134.9, 133.1, 130.1, 127.9, 127.7, 119.1, 118.3, 118.0, 29.7, 26.7, 21.6, 19.7. MS m/z: calculated for $C_{82}H_{78}N_4O_2Si_2[M+H]^+$ 1207.6, found MALDI 1207.6. λ_{abs} ($CHCl_3$) 421, 518, 553, 593, 648 nm.

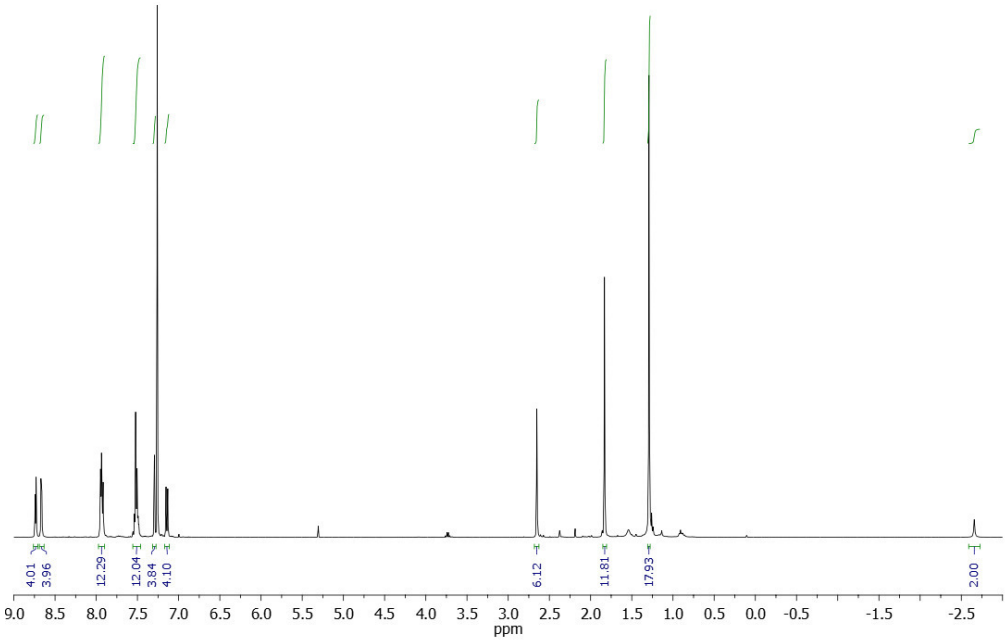

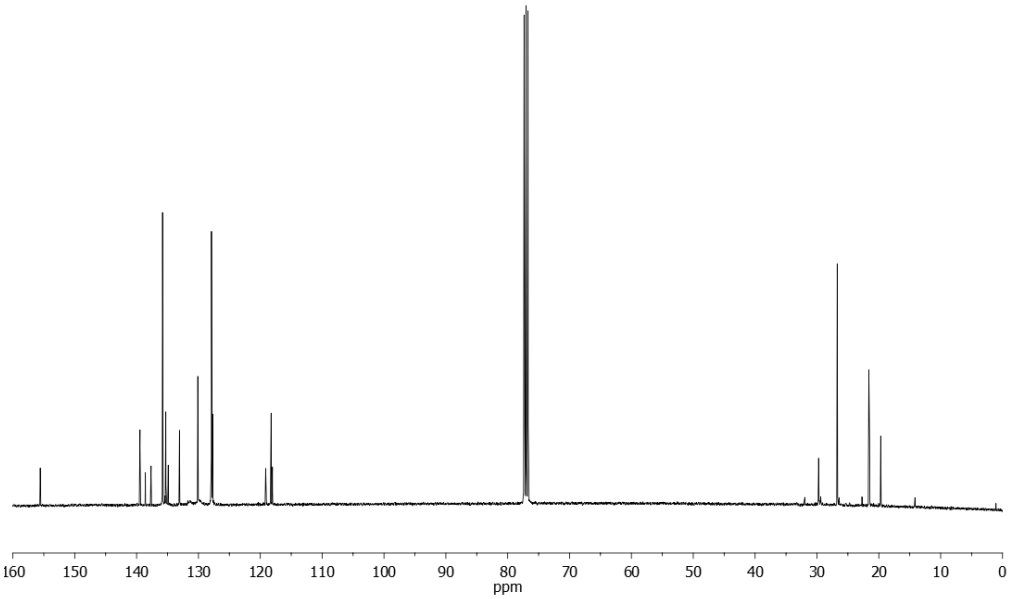
160
150
140
130
120
110
100
90
80
70
60
50
40
30
20
10
0
ppm

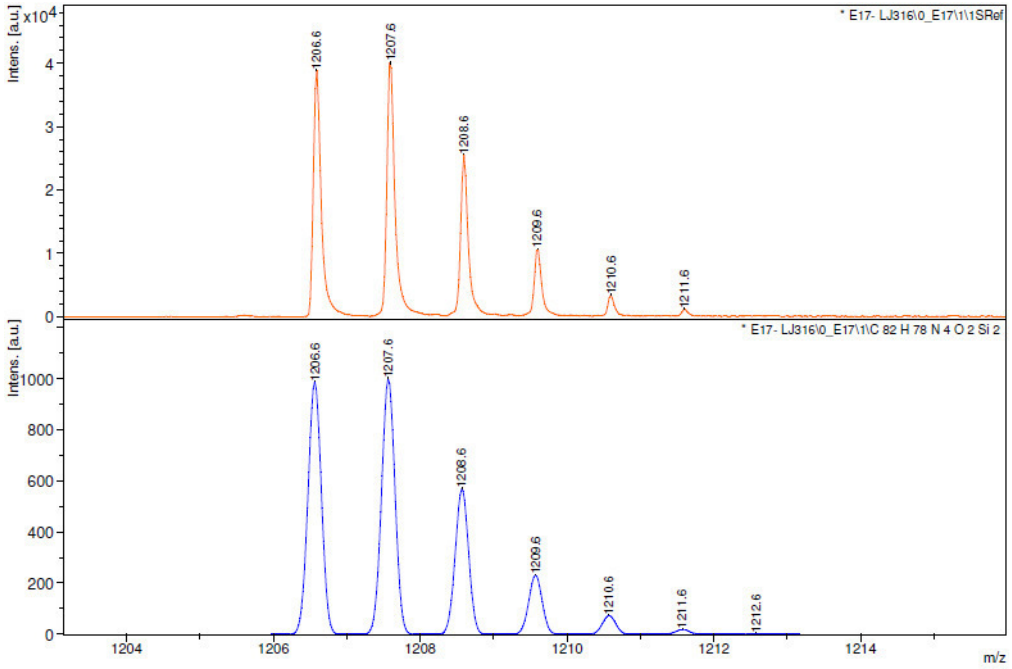
Intens. [a.u.]
x10^4
4
3
2
1
0
1206.6
1207.6
1208.6
1209.6
1210.6
1211.6
* E17- LJ316\0_E17\1\1SRef
Intens. [a.u.]
1000
800
600
400
200
0
1206.6
1207.6
1208.6
1209.6
1210.6
1211.6
1212.6
* E17- LJ316\0_E17\1\C 82 H 78 N 4 O 2 Si 2
1204
1206
1208
1210
1212
1214
m/z

Synthesis of compound **2**. Compound **1** (292 mg, 0.24 mmol) was dissolved in THF (100 mL), and tetrabutylammonium fluoride (1.0 M in THF) (350 µL, 1.21 mmol) was added at room temperature. After completion of the reaction, the solution was hydrolyzed with water and extracted with DCM. The organic phase was washed with brine, dried over $MgSO_4$, filtered and solvents were removed by evaporation under vacuum. The crude was washed with cold hexane and filtered getting a purple solid. The compound **2** (177 mg, 99%) was characterized by ^{1}H, ^{13}C -NMR, FAB and UV/vis.

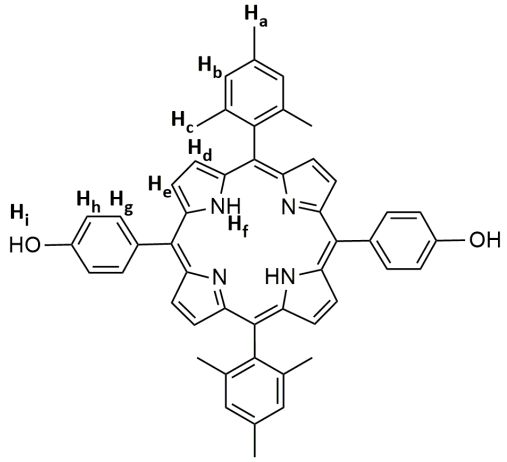

Compound **2**. ^{1}H NMR (400 MHz, DMSO-d_6) δ 9.93 (s, 2H, H_i), 8.84 (d, *J* = 4.7 Hz, 4H, H_e), 8.61 (d, *J* = 4.7 Hz, 4H, H_d), 8.00 (d, *J* = 8.6 Hz, 4H, H_g), 7.35 (s, 4H, H_b), 7.18 (d, *J* = 8.6 Hz, 4H, H_h), 2.59 (s, 6H, H_a), 1.76 (s, 12H, H_c), -2.72 (s, 2H, H_f). ^{13}C NMR (126 MHz, DMSO-d_6) δ 157.9, 138.9, 138.3, 137.9, 136.8, 135.9, 134.9, 129.6, 128.7, 128.3, 127.9, 120.1, 117.9, 114.4, 27.0, 21.6, 19.7. MS m/z: calculated for $C_{50}H_{42}N_4O_2[M]^+$ 730.3, found FAB+ 730.9. λ_{abs} (DMSO) 422, 518, 554, 595, 650 nm.

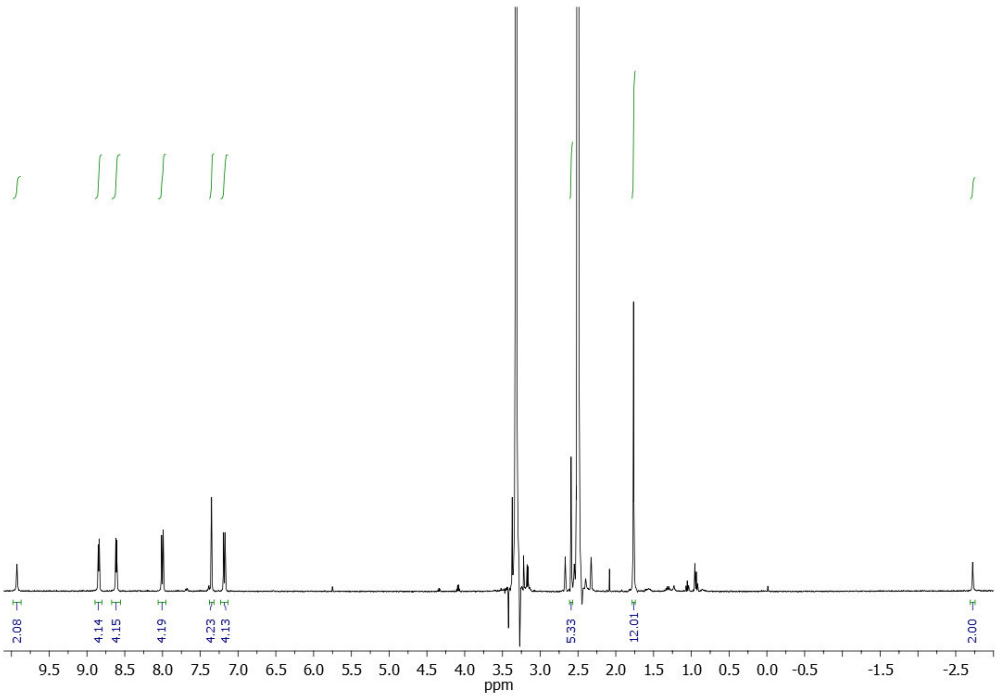
2.08
4.14
4.15
4.19
4.23
4.13
5.33
12.01
2.00
9.5 9.0 8.5 8.0 7.5 7.0 6.5 6.0 5.5 5.0 4.5 4.0 3.5 3.0 2.5 2.0 1.5 1.0 0.5 0.0 -0.5 -1.5 -2.5
ppm

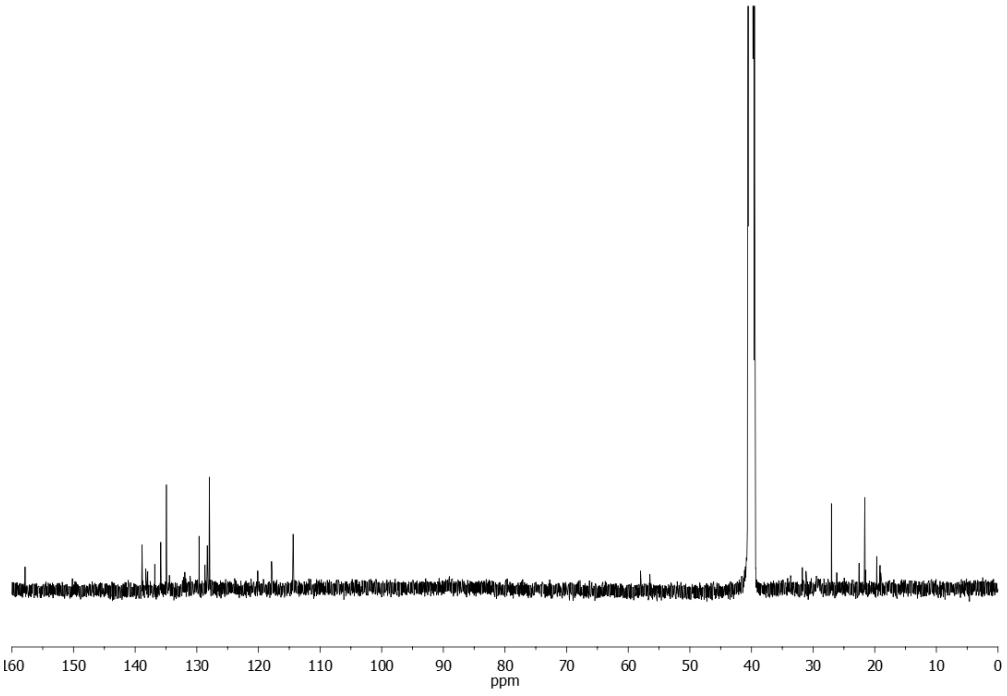
160 150 140 130 120 110 100 90 80 70 60 50 40 30 20 10 0
ppm

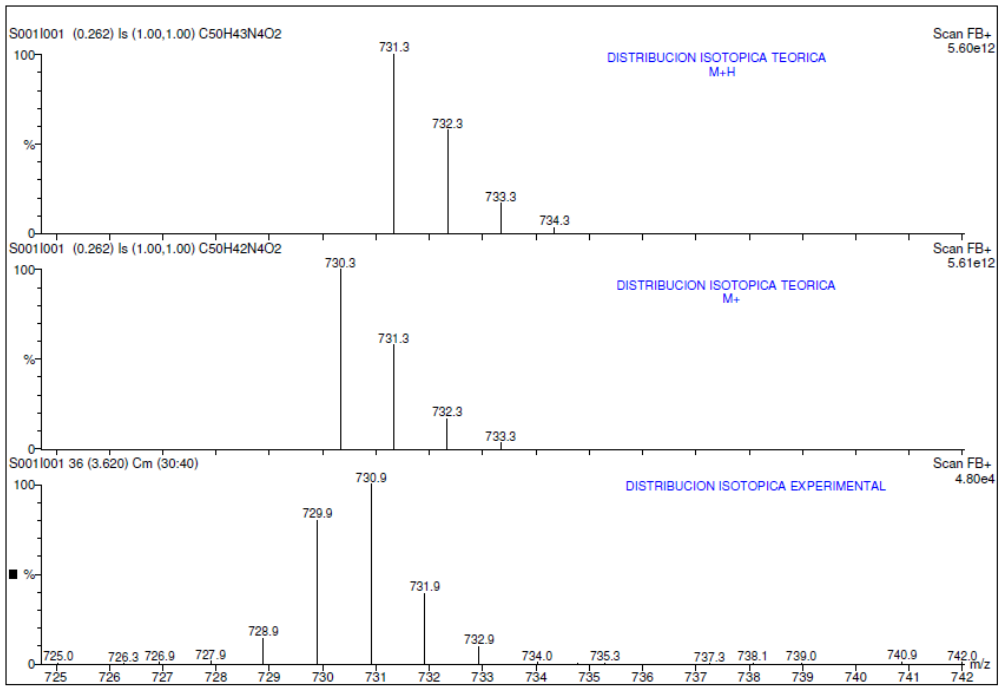

Synthesis of compound **3**. Compound **2** (411 mg, 0.56 mmol) was dissolved in dry DMF (110 mL) under Ar, and dry K_2CO_3 (934 mg, 6.76 mmol) was added at room temperature. The reaction was then heated at 55 °C and a solution of 10-bromo-1-decene (23 µL, 0.11 mmol) in dry DMF (4.5 mL) was added dropwise. After 10 min stirring, 0.11 mmol more of 10-bromo-1-decene in dry DMF were added, and the resulting mixture was stirred at 55 °C for 3 h. The complete reaction was poured onto cold HCl 1M, the solid was removed by filtration and dissolved in $CHCl_3$, and the filtrate was also extracted with $CHCl_3$ to collect all possible product. The organic phases were washed with brine, dried over $MgSO_4$ and filtered. The solvent was removed under vacuum and the crude product was purified by column chromatography (silica gel, $CHCl_3$). The compound **3** (91 mg, 47%) was characterized by ^{1}H, ^{13}C -NMR, MALDI and UV/vis.

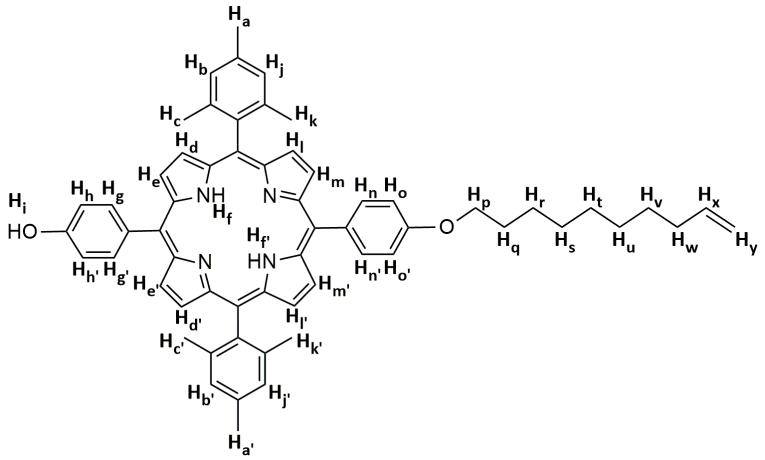

Compound **3**. ^{1}H NMR (400 MHz, $CDCl_3$) δ 8.83 (d, *J* = 4.7 Hz, 2H, $H_{e,e'}$), 8.79 (d, *J* = 4.7 Hz, 2H, $H_{m,m'}$), 8.67 (dd, *J* = 4.7 Hz, 4H, $H_{d,d',l,l'}$), 8.09 (d, *J* = 8.6 Hz, 2H, $H_{g,g'}$), 8.01 (d, *J* = 8.4 Hz, 2H, $H_{n,n'}$), 7.25 – 7.20 (m, 6H, $H_{h,h',b,b',j,j'}$), 7.06 (d, *J* = 8.4 Hz, 2H, $H_{o,o'}$), 5.89 – 5.79 (m, 1H, H_x), 5.05 – 4.93 (m, 2H, H_y), 4.21 (t, *J* = 6.5 Hz, 2H, H_p), 2.61 (s, 6H, $H_{a,a'}$), 2.11 – 2.05 (m, 2H, H_w), 1.98 – 1.91 (m, 2H, H_q), 1.83 (s, 12H, $H_{c,c',k,k'}$), 1.64 – 1.56 (m, 2H, H_v), 1.45 – 1.39 (m, 6H, $H_{r,s,t}$), 0.92 – 0.85 (m, 2H, H_u), -2.60 (bs, 2H, $H_{f,f'}$). ^{13}C NMR (101 MHz, $CDCl_3$) δ 159.0, 155.5, 139.5, 139.3, 138.6, 137.7, 135.6, 135.5, 134.5, 134.2, 127.8, 119.3, 119.0, 118.2, 114.3, 113.7, 112.8, 68.4, 33.9, 29.8, 29.5, 29.2, 29.0, 26.3, 21.7, 21.5. MS m/z: calculated for $C_{60}H_{60}N_4O_2[M]^+$ 868.5, found MALDI 868.5. λ_{abs} ($CHCl_3$) 421, 517, 553, 593, 649 nm.

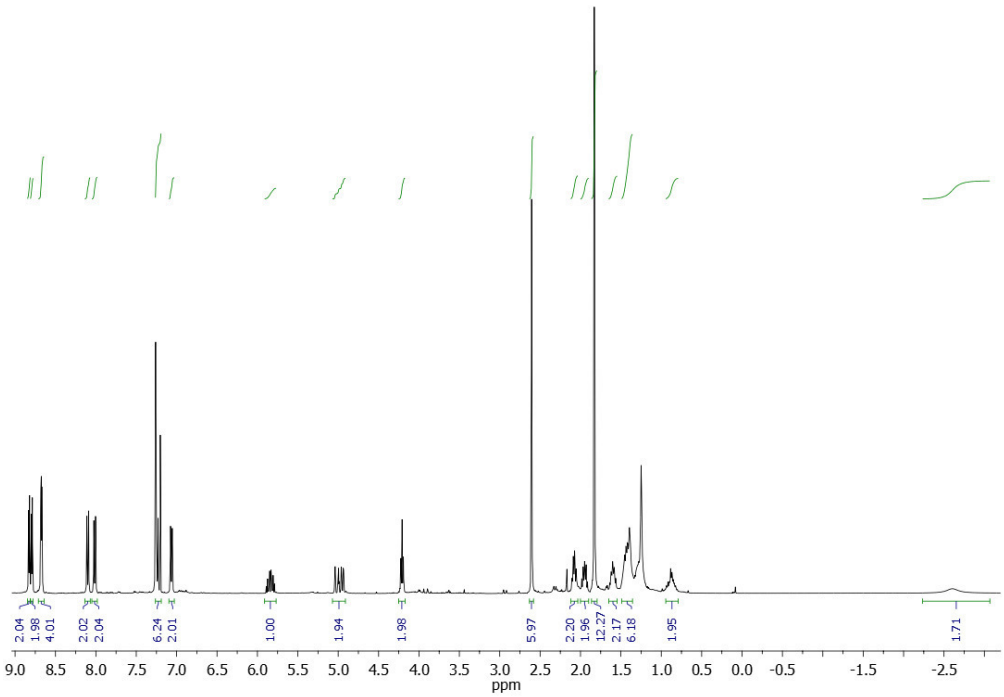
2.04
1.98
4.01
2.02
2.04
6.24
2.01
1.00
1.94
1.98
5.97
2.20
1.96
12.27
2.17
6.18
1.95
1.71
9.0 8.5 8.0 7.5 7.0 6.5 6.0 5.5 5.0 4.5 4.0 3.5 3.0 2.5 2.0 1.5 1.0 0.5 0.0 -0.5 -1.5 -2.5
ppm

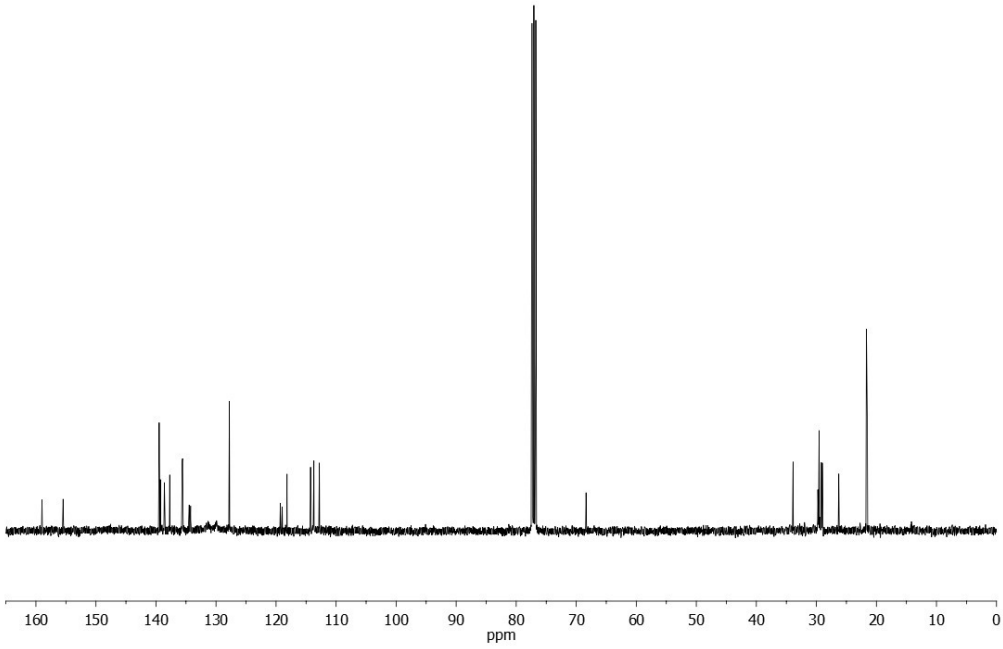
160 150 140 130 120 110 100 90 80 70 60 50 40 30 20 10 0
ppm

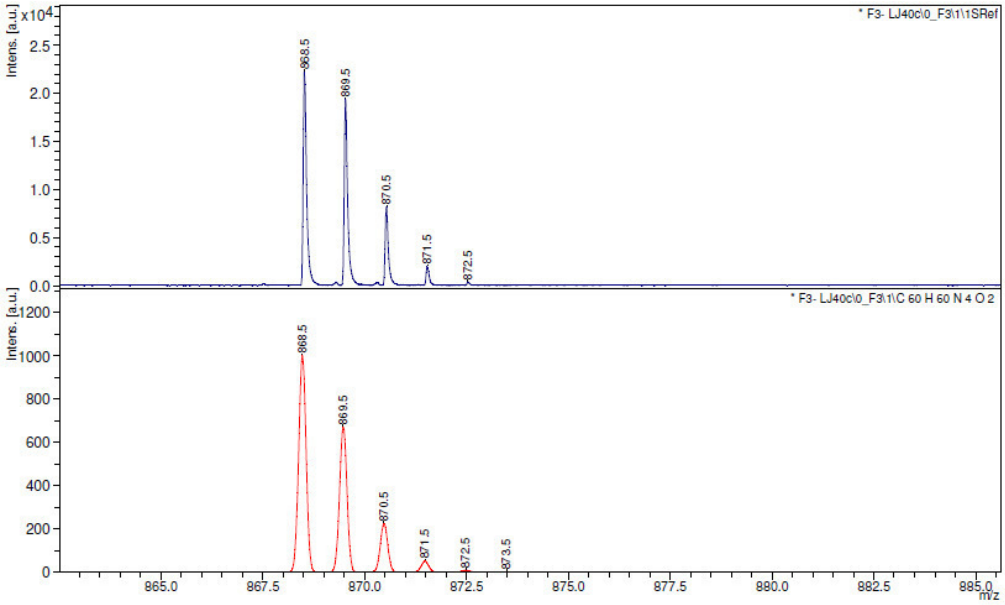

Synthesis of compound **4**. Compound **3** (116 mg, 0.13 mmol) was dissolved in dry 2-butanone (20 mL) under Ar. Dry K_2CO_3 (184 mg, 1.33 mmol) and 1,6-dibromohexane (5 µL, 0.033 mmol) were added, and the resulting mixture was stirred under reflux for 48 h. The reaction was quenched with water and extracted with $CHCl_3$. The organic phase was washed with brine, dried over $MgSO_4$ and the solvent was removed under vacuum. The crude product was purified by column chromatography (silica gel, DCM/hexane 2:3) and the purple product **4** (40 mg, 67%) was characterized by ^1H, ^{13}C -NMR, MALDI and UV/vis.

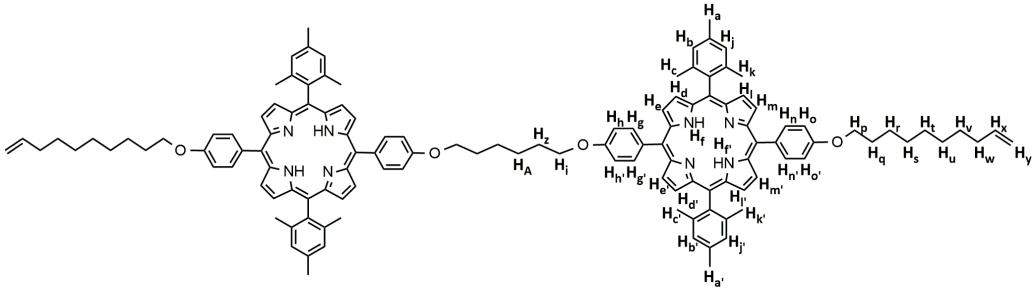

Compound **4**. ^{1}H NMR (400 MHz, $CDCl_3$) δ 8.85 (d, *J* = 4.7 Hz, 2H, $H_{e,e'}$), 8.83 (d, *J* = 4.7 Hz, 2H, $H_{m,m'}$), 8.68 (t, 4H, $H_{d,d',l,l'}$), 8.14 (d, *J* = 8.6 Hz, 2H, $H_{g,g'}$), 8.11 (d, *J* = 8.4 Hz, 2H, $H_{n,n'}$), 7.32 (d, *J* = 8.6 Hz, 2H, $H_{h,h'}$), 7.27 (s, 4H, $H_{b,b',j,j'}$), 7.26 – 7.25 (m, 2H, $H_{o,o'}$), 5.91 – 5.81 (m, 1H, H_x), 5.06 – 4.95 (m, 2H, H_y), 4.35 (t, *J* = 6.3 Hz, 2H, H_i), 4.25 (t, *J* = 6.5 Hz, 2H, H_p), 2.62 (s, 6H, $H_{a,a'}$), 2.14 – 2.07 (m, 2H, H_w), 2.02 – 1.95 (m, 4H, $H_{q,z}$), 1.84 (s, 12H, $H_{c,c',k,k'}$), 1.67 – 1.59 (m, 2H, H_v), 1.49 – 1.41 (m, 4H, $H_{r,A}$), 0.77 – 0.70 (m, 6H, $H_{s,t,u}$), -2.59 (s, 2H, $H_{f,f'}$). ^{13}C NMR (101 MHz, $CDCl_3$) δ 159.0, 139.4, 139.3, 138.6, 137.7, 135.6, 135.5, 134.3, 134.2, 127.7, 119.2, 119.1, 118.1, 114.2, 112.8, 112.7, 68.3, 68.2, 33.9, 32.0, 29.7, 29.5, 29.4, 29.2, 29.0, 26.3, 22.7, 21.7, 21.5. MS m/z: calculated for $C_{126}H_{130}N_8O_4[M]^+$ 1820.0, found MALDI 1819.9. λ_{abs} ($CHCl_3$) 421, 517, 553, 594, 649 nm.

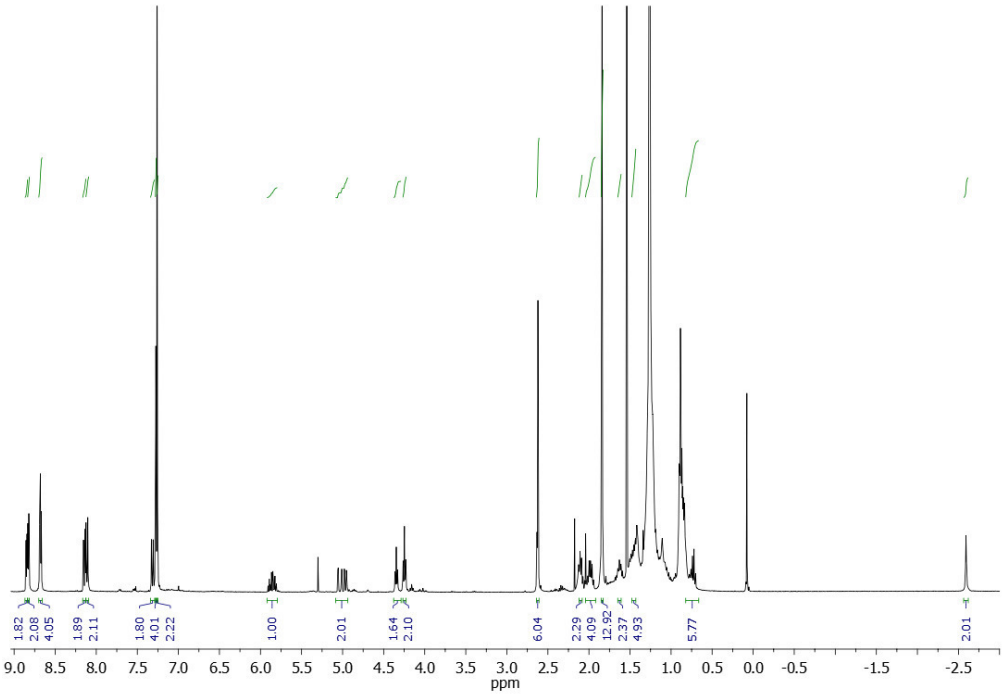

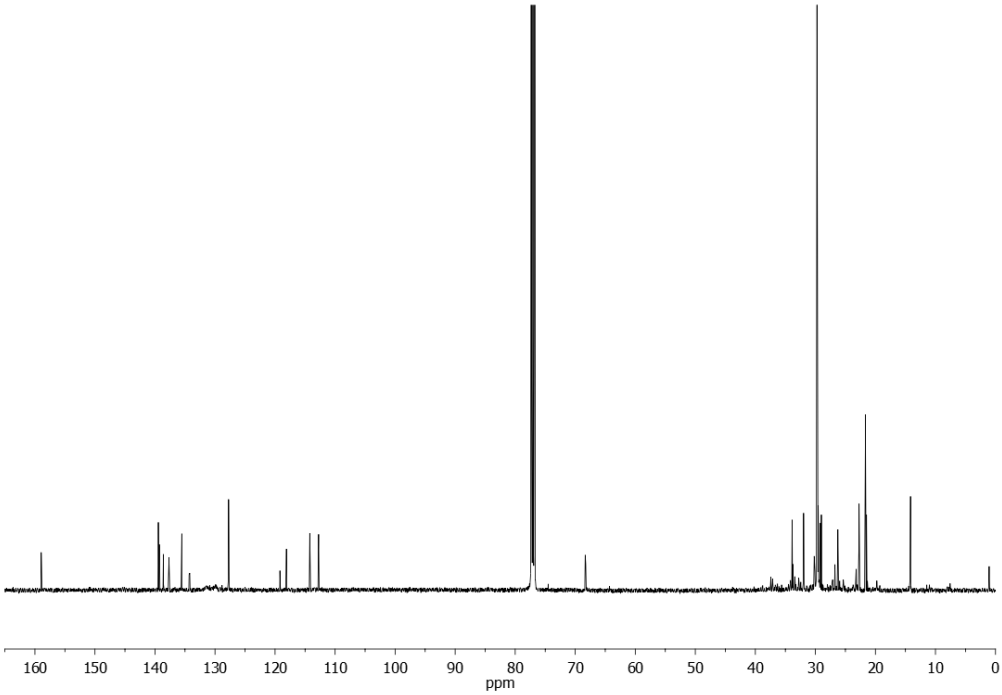
160
150
140
130
120
110
100
90
80
70
60
50
40
30
20
10
0
ppm

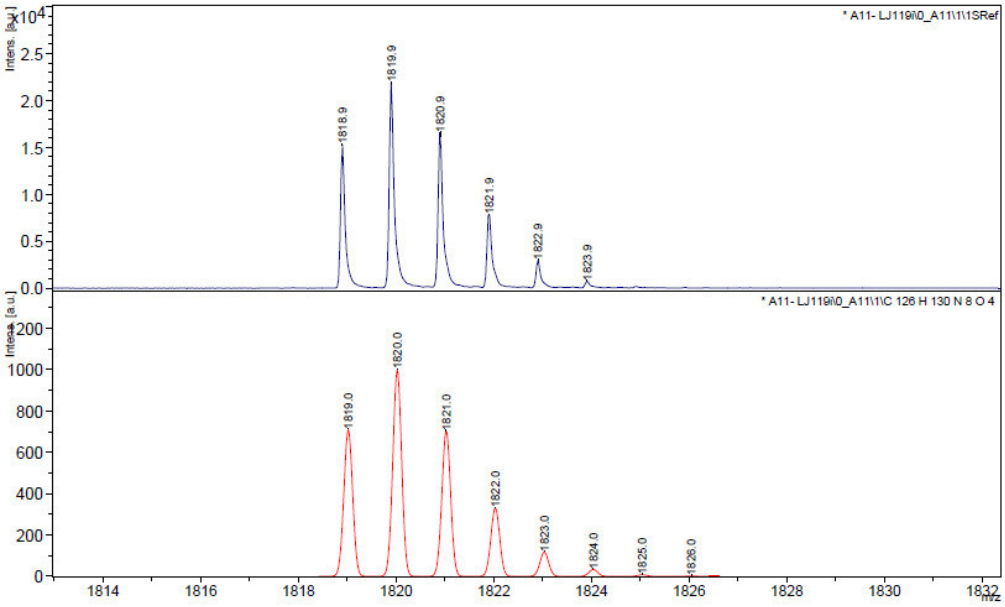
* A11- LJ119\0_A11\1\1SRef
1818.9
1819.9
1820.9
1821.9
1822.9
1823.9
Intens. [a.u.]
* A11- LJ119\0_A11\1\C 126 H 130 N 8 O 4
1819.0
1820.0
1821.0
1822.0
1823.0
1824.0
1825.0
1826.0
1814
1816
1818
1820
1822
1824
1826
1828
1830
1832
m/z

Synthesis of **U-por**. Compound **4** (44 mg, 0.024 mmol) was dissolved in $CHCl_3$ (10 mL) and a solution of zinc acetate (14 mg, 0.078 mmol) in methanol (0.5 mL) was added. The resulting mixture was stirred at room temperature. After completion of the reaction, the solvent was removed under vacuum, and the product was dissolved in $CHCl_3$ and extracted with water several times. The combined organic phases were washed with brine, dried over $MgSO_4$ and the solvent was removed under vacuum. The **U-por** (46 mg, 99%) was characterized by ^{1}H, ^{13}C -NMR, MALDI and UV/vis.

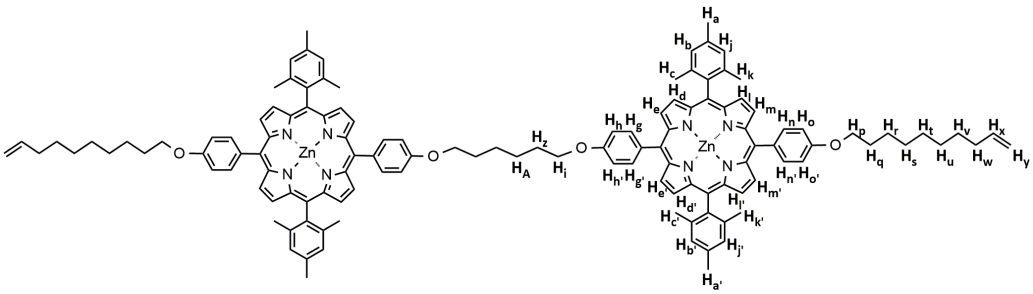

U-por. ^{1}H NMR (400 MHz, $CDCl_3$) δ 8.96 (d, *J* = 4.7 Hz, 2H, $H_{e,e'}$), 8.94 (d, *J* = 4.7 Hz, 2H, $H_{m,m'}$), 8.78 (t, 4H, $H_{d,d',l,l'}$), 8.17 (d, *J* = 8.6 Hz, 2H, $H_{g,g'}$), 8.14 (d, *J* = 8.4 Hz, 2H, $H_{n,n'}$), 7.32 (d, *J* = 8.6 Hz, 2H, $H_{h,h'}$), 7.28 – 7.26 (m, 6H, $H_{b,b',j,j',o,o'}$), 5.92 – 5.82 (m, 1H, H_x), 5.07 – 4.95 (m, 2H, H_y), 4.34 (t, *J* = 6.3 Hz, 2H, H_i), 4.25 (t, *J* = 6.5 Hz, 2H, H_p), 2.63 (s, 6H, $H_{a,a'}$), 2.12 – 2.08 (m, 2H, H_w), 2.03 – 1.95 (m, 4H, $H_{q,z}$), 1.85 (s, 12H, $H_{c,c',k,k'}$), 1.67 – 1.60 (m, 2H, H_v), 1.50 – 1.43 (m, 4H, $H_{r,A}$), 0.92 – 0.85 (m, 6H, $H_{s,t,u}$). ^{13}C NMR (101 MHz, $CDCl_3$) δ 158.8, 150.5, 149.9, 139.3, 139.2, 139.1, 137.4, 135.5, 135.4, 135.1, 135.0, 132.4, 130.6, 127.7, 120.1, 119.1, 114.2, 112.7, 112.6, 68.3, 33.9, 32.0, 29.8, 29.5, 29.2, 29.0, 26.3, 22.7, 21.7, 21.5. MS m/z: calculated for $C_{126}H_{126}N_8O_4Zn_2$ $[M+H]^+$ 1946.8, found MALDI 1946.8. λ_{abs} ($CHCl_3$) 424, 554, 599 nm.

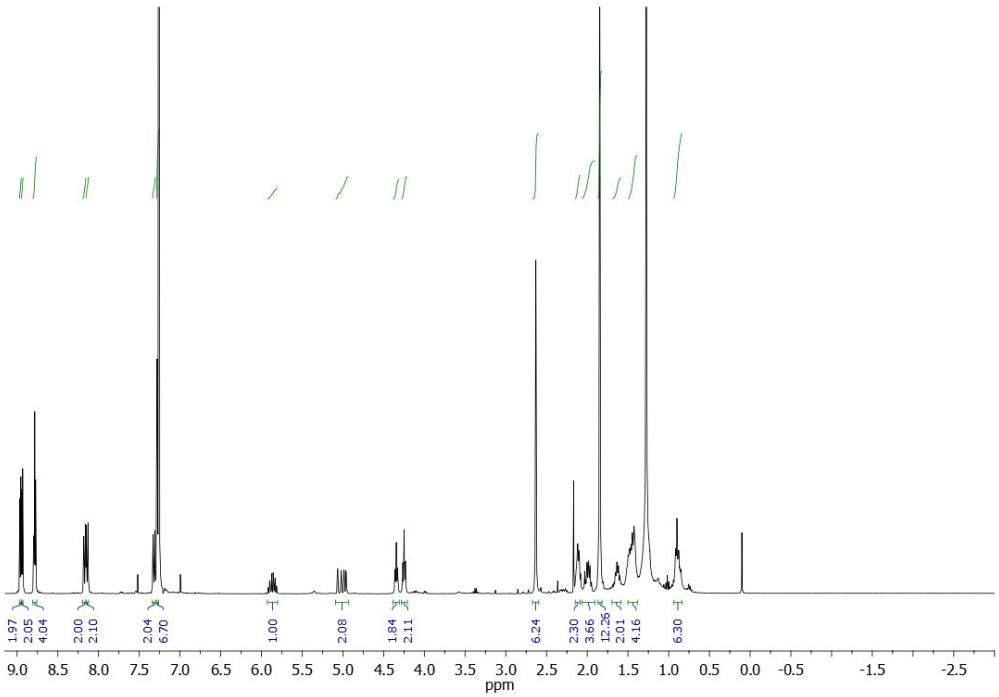
1.97
2.05
4.04
2.00
2.10
2.04
6.70
1.00
2.08
1.84
2.11
6.24
2.30
3.66
12.26
2.01
4.16
6.30
9.0 8.5 8.0 7.5 7.0 6.5 6.0 5.5 5.0 4.5 4.0 3.5 3.0 2.5 2.0 1.5 1.0 0.5 0.0 -0.5 -1.5 -2.5
ppm

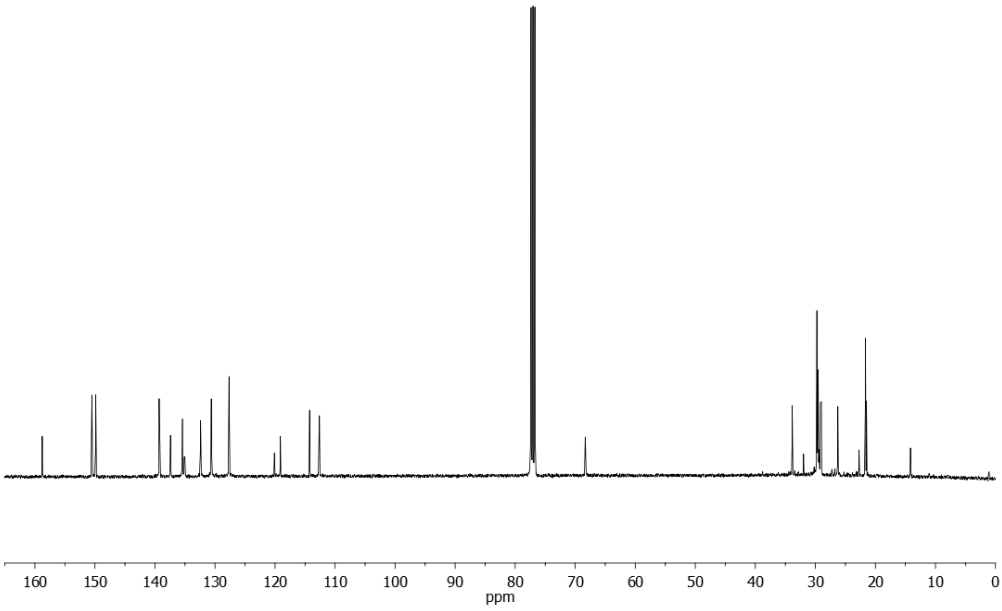
160 150 140 130 120 110 100 90 80 70 60 50 40 30 20 10 0
ppm

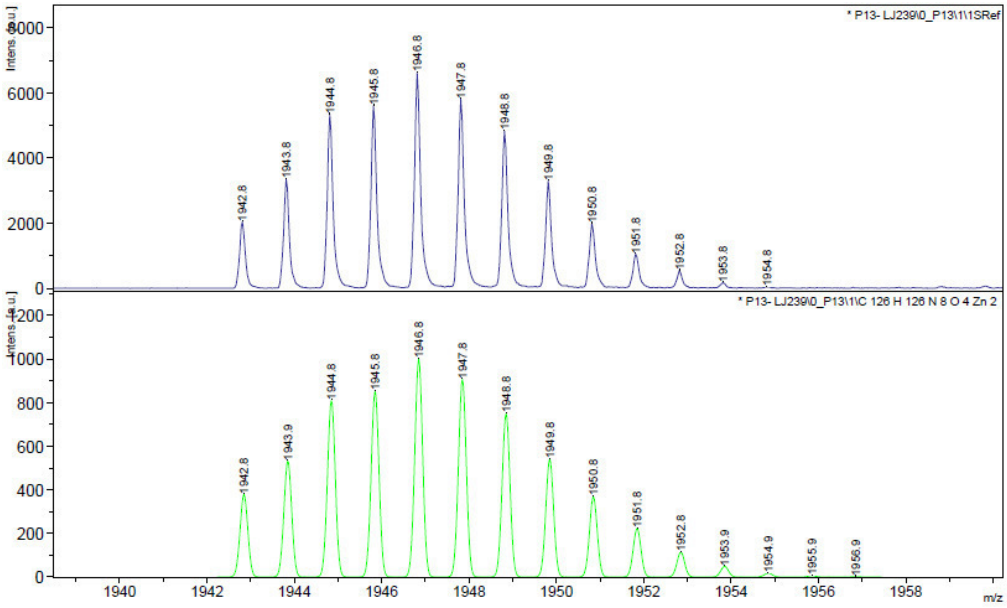

Synthesis of **mac-por**. **U-por** (19 mg, 0.0097 mmol) was dissolved in dry DCM (97 mL) and degassed for 30 min. Grubbs' 1st generation catalyst (1.6 mg, 0.0019 mmol) was added and the solution was stirred under reflux overnight. The progress of the reaction was monitored by TLC (hexane/EtOAc 8:2). The reaction was then stopped, filtered through a pad of celite and the solvent evaporated under reduced pressure. The crude product was purified by column chromatography (silica gel, hexane/EtOAc 9:1) and the purple **mac-por** (7.6 mg, 41%) was characterized by ^{1}H NMR, MALDI and UV/vis.

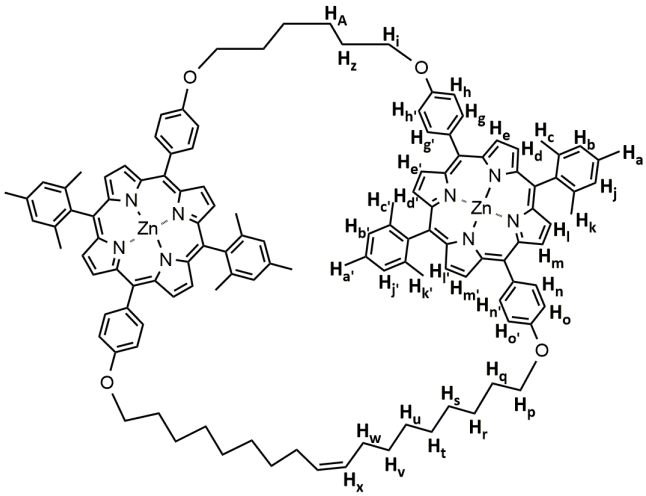

mac-por. ^{1}H NMR (400 MHz, $CDCl_3$) δ 8.79 – 8.72 (m, 8H, $H_{e,e',m,m'}$, cis/trans isomers), 8.52 – 8.49 (m, 8H, $H_{d,d',l,l'}$, cis/trans isomers), 7.97 – 7.93 (m, 8H, $H_{g,g',n,n'}$, cis/trans isomers), 7.29 – 7.26 (m, 4H, $H_{h,h'}$, cis/trans isomers), 7.18 – 7.15 (m, 4H, $H_{o,o'}$, cis/trans isomers), 6.87 (s, 8H, $H_{b,b',j,j'}$, cis/trans isomers), 5.44 – 5.37 (m, 2H, H_x, cis/trans isomers), 4.41 – 4.39 (m, 4H, H_i, cis/trans isomers), 4.23 – 4.19 (m, 4H, H_p, cis/trans isomers), 2.33 (s, 6H, $H_{a,a'}$), 2.11 – 2.07 (m, 4H, $H_{w,q}$), 1.97 – 1.93 (m, 4H, $H_{z,v}$), 1.42 (s, 12H, $H_{c,c',k,k'}$), 1.24 – 1.19 (m, 4H, $H_{r,A}$), 0.91 – 0.85 (m, 6H, $H_{s,t,u}$). MS m/z: calculated for $C_{124}H_{122}N_8O_4Zn_2[M+H]^+$ 1918.8, found MALDI 1918.8. λ_{abs} ($CHCl_3$) 421, 553, 598 nm.

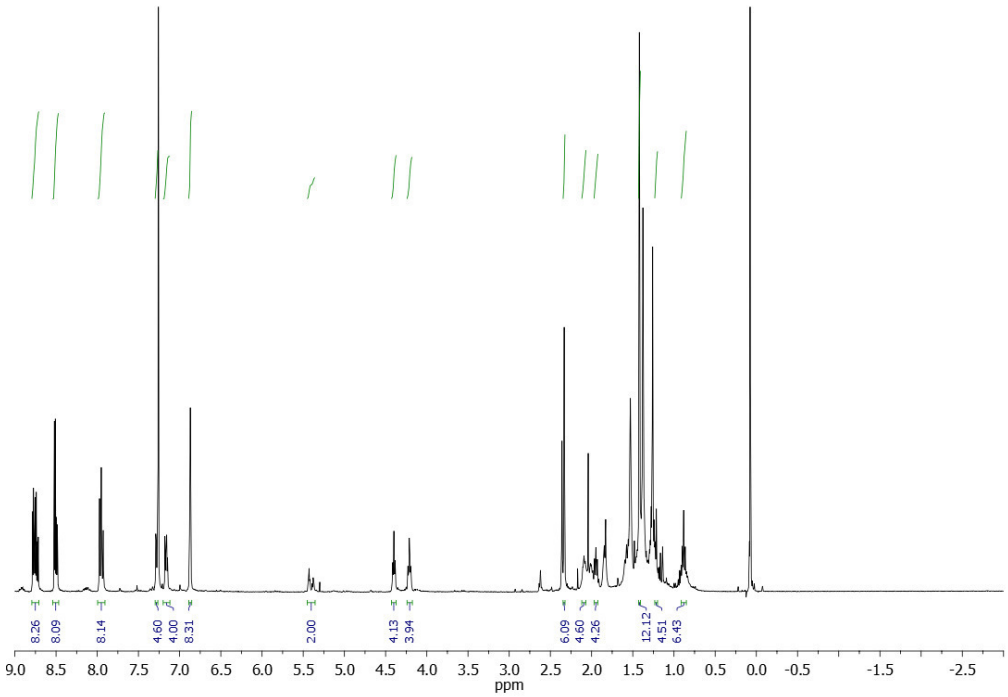
8.26
8.09
8.14
4.60
4.00
8.31
2.00
4.13
3.94
6.09
4.60
4.26
12.12
4.51
6.43
9.0 8.5 8.0 7.5 7.0 6.5 6.0 5.5 5.0 4.5 4.0 3.5 3.0 2.5 2.0 1.5 1.0 0.5 0.0 -0.5 -1.5 -2.5
ppm

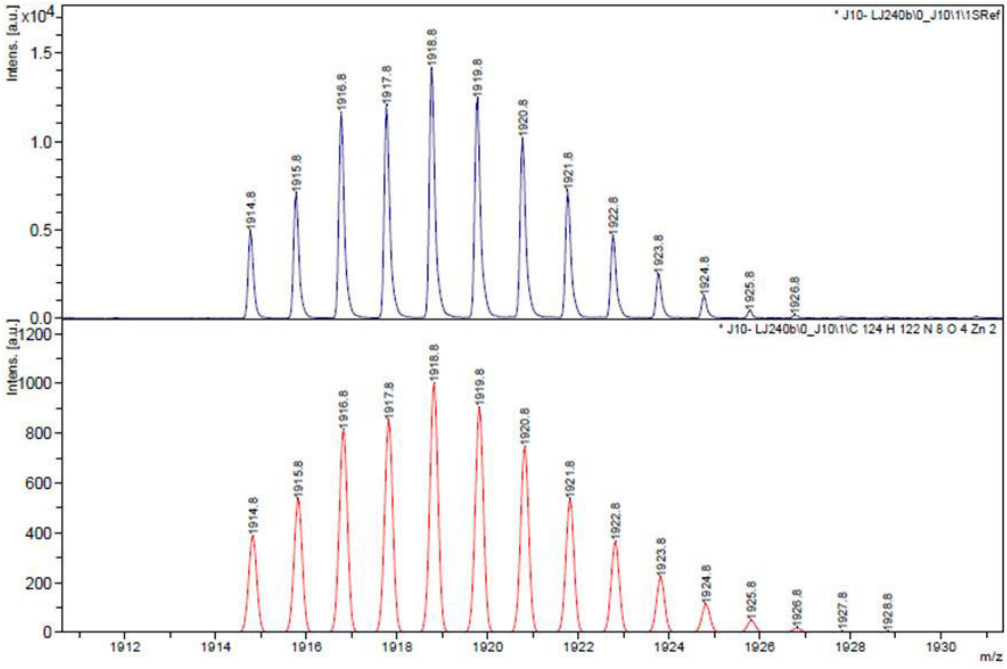
Intens. [a.u.]
x10^4
1.5
1.0
0.5
0.0
* J10- LJ240b\0_J10\1\1SRef
1914.8
1915.8
1916.8
1917.8
1918.8
1919.8
1920.8
1921.8
1922.8
1923.8
1924.8
1925.8
1926.8
Intens. [a.u.]
1200
1000
800
600
400
200
0
* J10- LJ240b\0_J10\1\C 124 H 122 N 8 O 4 Zn 2
1914.8
1915.8
1916.8
1917.8
1918.8
1919.8
1920.8
1921.8
1922.8
1923.8
1924.8
1925.8
1926.8
1927.8
1928.8
1912 1914 1916 1918 1920 1922 1924 1926 1928 1930
m/z

General procedure for SWCNTs functionalization

The (6,5)-enriched SWCNTs purchased from Sigma Aldrich Co. were purified previously. 50 mg of (6,5)-enriched SWCNTs were suspended in 34 mL of 35% HCl and sonicated for 15 min. The mixture was poured onto milliQ water and filtered through a polycarbonate membrane of 0.2 µm pore size. The solid was washed with water to neutral pH and then dried in an oven at 350 °C for 30 min.

The SWCNTs (2 mg) were suspended in tetrachloroethane (TCE, 2 mL) through sonication for 10 min and mixed with **U-por** (16.3 mg, 0.0084 mmol) and Grubbs' 2nd generation catalyst (7.2 mg, 0.0084 mmol) at room temperature for 72 hours. After this time, the suspension was filtered through a polytetrafluoroethylene membrane with a pore size of 0.2 µm, and the solid was washed profusely with DCM. The solid was re-suspended in 20 mL of DCM through sonication (10 min) and filtered through a PTFE membrane of 0.2 µm pore size again. This purification step was repeated three times.

General procedure for SWCNTs functionalization (varying the relative concentration of U-por with respect to SWCNTs)

The SWCNTs were suspended in TCE (1 mg/mL) through sonication for 10 min and mixed with **U-por** (1.06 mM, 2.1 mM, 4.2 mM or 8.4 mM), and Grubbs' 2nd generation catalyst at room temperature for 72 hours. After this time, the suspension was filtered through a PTFE membrane with a pore size of 0.2 µm, and the solid was washed profusely with DCM. The solid was re-suspended in 20 mL of DCM through sonication (10 min) and filtered through a PTFE membrane of 0.2 µm pore size again. This purification step was repeated three times.

General procedure for SWCNTs functionalization (control experiments)

The SWCNTs (2 mg) were suspended in tetrachloroethane (TCE, 2 mL) through sonication for 10 min and mixed with **U-por** (16.3 mg, 0.0084 mmol) at room temperature for 72 hours. After this time, the suspension was filtered through a PTFE membrane with a pore size of 0.2 μm, and the solid was washed profusely with DCM. The solid was re-suspended in 20 mL of DCM through sonication (10 min) and filtered through a PTFE membrane of 0.2 μm pore size again. This purification step was repeated three times.

General procedure for de-threading functionalized SWCNTs

The functionalized nanotubes (1.1 mg) were suspended in 2.8 mL of TCE by sonication for 5 min and then heated to reflux (bp = 147 °C) for 30 min. The suspension was filtered through a PTFE membrane of 0.2 μm pore size, and the solid was washed profusely with DCM.

General procedure for dispersion preparation of (6,5)-enriched SWCNTs and MINT-por

The pristine or functionalized nanotubes (0.4 mg) were suspended in 4 mL of methanol, DMF or D_2O/SDBS (1 wt%) by sonication for 1 h (20 min for DMF), followed by 10 min of centrifugation at 5 kG and subsequent sonication for 2 min. The centrifugation and short sonication steps were repeated 3 times.

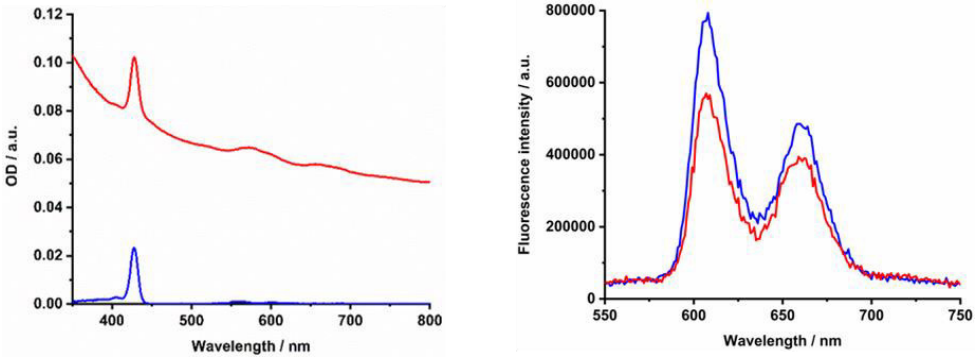

Figure S1. Absorption spectra (left) of diluted **MINT-por** (red) and **U-por** (blue) in DMF at room temperature, and the respective fluorescence (right), excited at 428 nm.

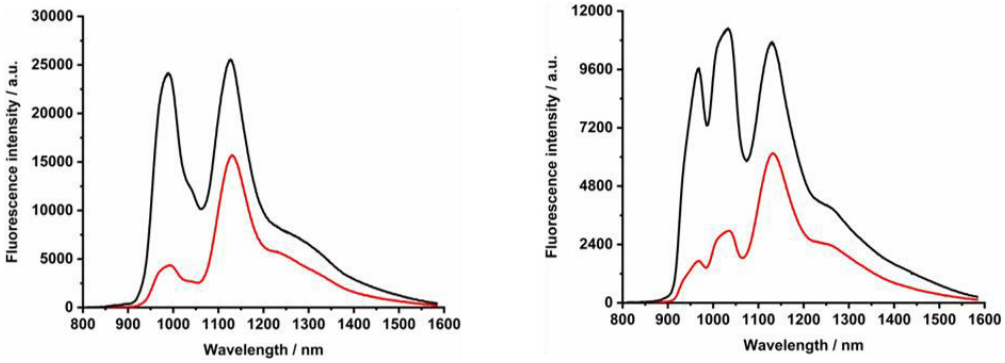

Figure S2. nIR fluorescence spectra of (6,5)-enriched SWCNTs (black) and **MINT-por** (red) in D_2O/SDBS (1 wt%) at room temperature, measured with an OD of 0.21 at 570 nm, with an excitation wavelength of 570 (left) and 660 nm (right).

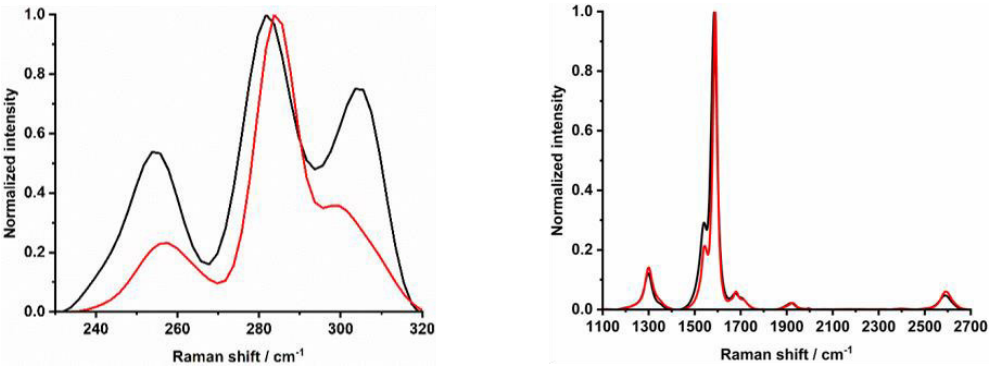

Figure S3. Radial breathing modes (left), and D, G and 2D modes (right) of drop-casted SWCNTs (black) and **MINT-por** (red) from methanol, with 633 nm laser excitation, normalized to (7,5).

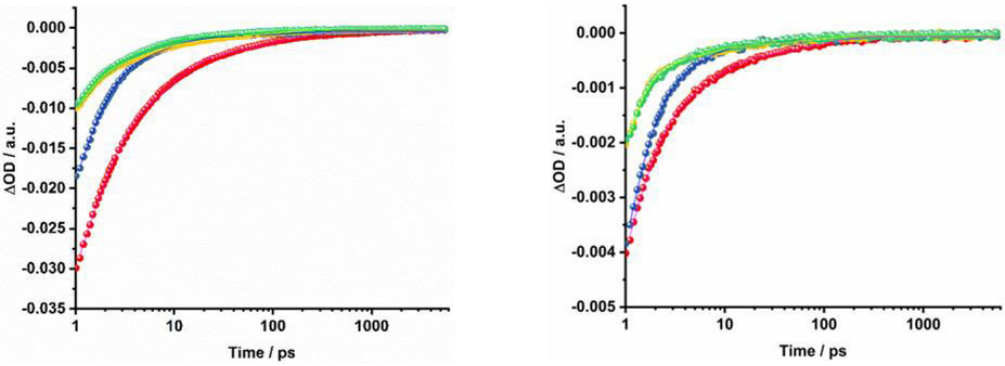

Figure S4. Time absorption profiles and the respective three exponential fits following 420 nm laser excitation of (6,5)-enriched SWCNTs (left) and **MINT-por** (right) in D_2O/SDBS (1 wt%) at 983 (red, (6,5)), 1021 (blue, (7,5)), 1118 (yellow, (8,4)) and 1139 nm (green, (7,6)).

Table S1. Lifetimes from three exponential fitting of the respective time absorption profiles.

(6,5)-enriched SWCNTs			
6,5	7,5	8,4	7,6
1.08 ± 0.03	0.88 ± 0.01	0.65 ± 0.02	0.63 ± 0.03
7.38 ± 0.27	6.03 ± 0.21	5.41 ± 0.21	4.15 ± 0.15
113.32 ± 5.27	168.21 ± 11.50	85.03 ± 3.89	58.55 ± 2.89

MINT-por			
6,5	7,5	8,4	7,6
0.79 ± 0.03	0.72 ± 0.03	0.50 ± 0.03	0.43 ± 0.03
5.20 ± 0.30	3.99 ± 0.32	4.35 ± 0.52	3.02 ± 0.30
77.62 ± 4.80	80.52 ± 11.71	71.91 ± 8.44	51.72 ± 5.81

4. REVERSIBLE DISPERSION AND RELEASE OF CARBON NANOTUBES *VIA* COOPERATIVE CLAMPING INTERACTIONS WITH HYDROGEN-BONDED NANORINGS

4. Reversible dispersion and release of carbon nanotubes *via* cooperative clamping interactions with hydrogen-bonded nanorings

Due to their outstanding electronic and mechanical properties, single-walled carbon nanotubes (SWCNTs) are promising nanomaterials for the future generation of optoelectronic devices and composites. However, their scarce solubility limits their application in many technologies that demand solution-processing of high-purity SWCNT samples. Although some non-covalent functionalization approaches have demonstrated their utility in extracting SWCNTs into different media, many of them produce short-lived dispersions or ultimately suffer from contamination by the dispersing agent. Here, we introduce an unprecedented strategy that relies on a cooperative clamping process. When mixing (6,5)SWCNTs with a dinucleoside monomer that is able to self-assemble in nanorings via Watson-Crick base-pairing, a synergic relationship is established. On one hand, the H-bonded rings are able to associate intimately with SWCNTs by embracing the tube sidewalls, which allows for an efficient SWCNT debundling and for the production of long-lasting SWCNT dispersions of high optical quality along a broad concentration range. On the other, nanoring stability is enhanced in the presence of SWCNTs, which are suitable guests for the ring cavity and contribute to the establishment of multiple cooperative noncovalent interactions. The inhibition of these reversible interactions, by just adding, for instance, a competing solvent for hydrogen-bonding, proved to be a simple and effective method to recover the pristine nanomaterial with no trace of the dispersing agent.

Chem. Sci. **2018**, *9*, 4176-4184.

4.1. Introduction

Carbon nanotubes (CNTs) are nanomaterials with impressive electronic and mechanical properties and are considered as strong candidates for the next generation of transistors, photovoltaics and (bio)chemical sensors.[1,2,3] However, they are insoluble in most solvents and infusible at any temperature, due to strong bundling caused by numerous van der Waals interactions, which hampers many of their applications.[4,5] Covalent and noncovalent surface modification with molecules, leading to homogeneous CNT dispersions in various solvents or bulk materials, is now common practice to facilitate their processing and to attach specific functions.[6,7,8,9] The covalent approach grants more stable dispersions, but the modification of the π-conjugated CNT surface with grafted molecules has a detrimental impact on their (semi)conducting and mechanical properties. That is the reason why noncovalent strategies, achieved by promoting strong interactions between CNT sidewalls and π-conjugated or apolar moieties in adequate solvents, are often considered more suitable.[9,10,11]

However, the weak and dynamic nature of supramolecular interactions frequently produces less durable dispersions of individual CNTs because bundling, which ultimately leads to CNT reprecipitation, remains as a strongly competing

[1] E. S. Snow, F. K. Perkins, E. J. Houser, S. C. Badescu, T. L. Reinecke, *Science* **2005**, *307*, 1942-1945.
[2] Q. Cao, H.-S. Kim, N. Pimparkar, J. P. Kulkarni, C. Wang, M. Shim, K. Roy, M. A. Alam, J. A. Rogers, *Nature* **2008**, *454*, 495-500.
[3] A. D. Franklin, *Science* **2015**, *349*, aab2750.
[4] S. H. Munson-McGee, *Phys. Rev. B* **1991**, *43*, 3331-3336.
[5] M. Cadek, J. N. Coleman, K. P. Ryan, V. Nicolosi, G. Bister, A. Fonseca, J. B. Nagy, K. Szostak, F. Beguin, W. J. Blau, *Nano Lett.* **2004**, *4*, 353-356.
[6] A. Hirsch, *Angew. Chem. Int. Ed.* **2002**, *41*, 1853-1859.
[7] D. Tasis, N. Tagmatarchis, A. Bianco, M. Prato, *Chem. Rev.* **2006**, *106*, 1105-1136.
[8] P. Singh, S. Campidelli, S. Giordani, D. Bonifazi, A. Bianco, M. Prato, *Chem. Soc. Rev.* **2009**, *38*, 2214-2230.
[9] N. Karousis, N. Tagmatarchis, D. Tasis, *Chem. Rev.* **2010**, *110*, 5366-5397.
[10] D. Britz, A. Khlobystov, *Chem. Soc. Rev.* **2006**, *35*, 637-659.
[11] Y.-L. Zhao, J. F. Stoddart, *Acc. Chem. Res.* **2009**, *42*, 1161-1171.

supramolecular process in solution. Bundling can be reduced by increasing the number of surface-binding functions in the dispersing agent and, importantly, by inducing wrapping interactions around single CNT cylinders (interaction mode II in Figure 1a below). A large number of composites with π-conjugated polymers,[12,13] DNA,[14,15,16] synthetic peptides,[17,18,19,20] or, in general, oligomers featuring multiple aromatic units[21,22,23,24] have been tested to stabilize CNTs selectively in solution by specific helical wrapping conformations around the tube.

A main drawback that originates from such a robust marriage is that polymer desorption *via* washing processes is often difficult to achieve, and CNTs purified or processed in this way may remain contaminated with the dispersing agent.[25,26] In order to address this issue, recent strategies have been reported that

[12] D. Tuncel, *Nanoscale* **2011**, *3*, 3545-3554.
[13] P. Bilalis, D. Katsigiannopoulos, A. Avgeropoulos, G. Sakellariou, *RSC Adv*. **2014**, *4*, 2911-2934.
[14] M. Zheng, A. Jagota, M. S. Strano, A. P. Santos, P. Barone, S. G. Chou, B. A. Diner, M. S. Dresselhaus, R. S. McLean, G. B. Onoa, G. G. Samsonidze, E. D. Semke, M. Usrey, D. Walls, *Science* **2003**, *302*, 1545-1548.
[15] M. Zheng, A. Jagota, E. D. Semke, B. A. Diner, R. S. McLean, S. R. S. Lustig, S. E. Richardson, N. G. Tassi, *Nat. Mater.* **2003**, *2*, 338-342.
[16] H. Cathcart, V. Nicolosi, J. M. Hughes, W. J. Blau, J. M. Kelly, S. J. Quinn, J. N. Coleman, *J. Am. Chem. Soc.* **2008**, *130*, 12734-12744.
[17] G. R. Dieckmann, A. B. Dalton, P. A. Johnson, J. Razal, J. Chen, G. M. Giordano, E. Muñoz, I. H. Musselman, R. H. Baughman, R. K. Draper, *J. Am. Chem. Soc.* **2003**, *125*, 1770-1777.
[18] A. B. Dalton, A. Ortiz-Acevedo, V. Zorbas, E. Brunner, W. M. Sampson, S. Collins, J. M. Razal, M. M. Yoshida, R. H. Baughman, R. K. Draper, I. H. Musselman, M. Jose-Yacaman, G. R. Dieckmann, *Adv. Funct. Mater.* **2004**, *14*, 1147-1151.
[19] A. Ortiz-Acevedo, H. Xie, V. Zorbas, W. M. Sampson, A. B. Dalton, R. H. Baughman, R. K. Draper, I. H. Musselman, G. R. Dieckmann, *J. Am. Chem. Soc.* **2005**, *127*, 9512-9517.
[20] J. Montenegro, C. Vázquez-Vázquez, A. Kalinin, K. E. Geckeler, J. R. Granja, *J. Am. Chem. Soc.* **2014**, *136*, 2484-2491.
[21] J. K. Sprafke, S. D. Stranks, J. H. Warner, R. J. Nicholas, H. L. Anderson, *Angew. Chem. Int. Ed*. **2011**, *50*, 2313-2316.
[22] G. Liu, F. Wang, S. Chaunchaiyakul, Y. Saito, A. K. Bauri, T. Kimura, Y. Kuwahara, N. Komatsu, *J. Am. Chem. Soc*. **2013**, *135*, 4805-4814.
[23] G. Clavé, G. Delport, C. Roquelet, J.-S. Lauret, E. Deleporte, F. Vialla, B. Langlois, R. Parret, C. Voisin, P. Roussignol, B. Jousselme, A. Gloter, O. Stephan, A. Filoramo, V. Derycke, S. Campidelli, *Chem. Mater*. **2013**, *25*, 2700-2707.
[24] I. Hijazi, T. Bourgeteau, R. Cornut, A. Morozan, A. Filoramo, J. Leroy, V. Derycke, B. Jousselme, S. Campidelli, *J. Am. Chem. Soc.* **2014**, *136*, 6348-6354.
[25] A. Nish, J. Hwang, J. Doig, R. Nicholas, *Nat. Nanotechnol.* **2007**, *2*, 640-646.
[26] P. Imin, M. Imit, A. Adronov, *Macromolecules* **2012**, *45*, 5045-5050.

focus mainly on: (1) switching between tightly and loosely bound polymer conformations,[27,28,29] which can be triggered thermally, photochemically[27] or by a change in solvent[28] or pH,[29] and on (2) inducing depolymerization processes,[30,31,32,33,34] which can also be made reversible by introducing supramolecular[32,33,34] or dynamic covalent bonds[35] along the polymer main chain.

Here, we introduce a novel approach that is instead based on clamping discrete self-assembled nanorings around the tube cross-section to efficiently and reversibly produce durable dispersions of individual single-walled CNTs (SWCNTs) in organic solvents. The encapsulation of SWCNTs within well-defined macrocycles,[19,36,37,38,39,40,41] forming rotaxane-type ensembles, has been recently explored using covalent cyclization reactions. The strategy followed by us relied on two extended aromatic binding sites to promote the supramolecular association of U-shaped molecules to SWCNTs, followed by "clipping" through ring-closing

[27] T. Umeyama, K. Kawabata, N. Tezuka, Y. Matano, Y. Miyato, K. Matsushige, M. Tsujimoto, S. Isoda, M. Takano, H. Imahori, *Chem. Commun.* **2010**, *46*, 5969-5971.
[28] Z. Zhang, Y. Che, R. A. Smaldone, M. Xu, B. R. Bunes, J. S. Moore, L. Zang, *J. Am. Chem. Soc.* **2010**, *132*, 14113-14117.
[29] S. Liang, Y. Zhao, A. Adronov, *J. Am. Chem. Soc.* **2014**, *136*, 970-977.
[30] W. Z. Wang, W. F. Li, X. Y. Pan, C. M. Li, L.-J. Li, Y. G. Mu, J. A. Rogers, M. B. Chan-Park, *Adv. Funct. Mater.* **2011**, *21*, 1643-1651.
[31] F. Lemasson, J. Tittmann, F. Hennrich, N. Sturzl, S. Malik, M. M. Kappes, M. Mayor, *Chem. Commun.* **2011**, *47*, 7428-7430.
[32] A. Llanes-Pallas, K. Yoosaf, H. Traboulsi, J. Mohanraj, T. Seldrum, J. Dumont, A. Minoia, R. Lazzaroni, N. Armaroli, D. Bonifazi, *J. Am. Chem. Soc.* **2011**, *133*, 15412-15424.
[33] I. Pochorovski, H. Wang, J. I. Feldblyum, X. Zhang, A. L. Antaris, Z. Bao, *J. Am. Chem. Soc.* **2015**, *137*, 4328-4331.
[34] F. Toshimitsu, N. Nakashima, *Nat. Commun.* **2014**, *5*, 5041.
[35] T. Lei, X. Chen, G. Pitner, H. S. P. Wong, Z. Bao, *J. Am. Chem. Soc.* **2016**, *138*, 802-805.
[36] E. Martínez-Periñán, A. de Juan, Y. Pouillon, C. Schierl, V. Strauss, N. Martín, A. Rubio, D. M. Guldi, E. Lorenzo, E. M. Pérez, *Nanoscale* **2016**, *8*, 9254-9264.
[37] A. López-Moreno, B. Nieto-Ortega, M. Moffa, A. de Juan, M. M. Bernal, J. P. Fernández-Blázquez, J. J. Vilatela, D. Pisignano, E. M. Pérez, *ACS Nano* **2016**, *10*, 8012-8018.
[38] S. Leret, Y. Pouillon, S. Casado, C. Navio, A. Rubio, E. M. Pérez, *Chem. Sci.* **2017**, *8*, 1927-1935.
[39] A. López-Moreno, E. M. Pérez, *Chem. Commun.* **2015**, *51*, 5421-5424.
[40] A. de Juan, M. M. Bernal, E. M. Pérez, *ChemPlusChem* **2015**, *80*, 1153-1157.
[41] A. de Juan, Y. Pouillon, L. Ruiz-González, A. Torres-Pardo, S. Casado, N. Marín, A. Rubio, E. M. Pérez, *Angew. Chem. Int. Ed.* **2014**, *53*, 5394-5400.

metathesis to produce the mechanically interlocked species.[36,37,38,39,40,41] Depending on the chemical nature of the recognition motif, we have also observed the formation of oligomers that wrap around the SWCNTs.[38] The approach followed herein, in contrast, profits from a dynamic, strongly cooperative noncovalent macrocyclization process.

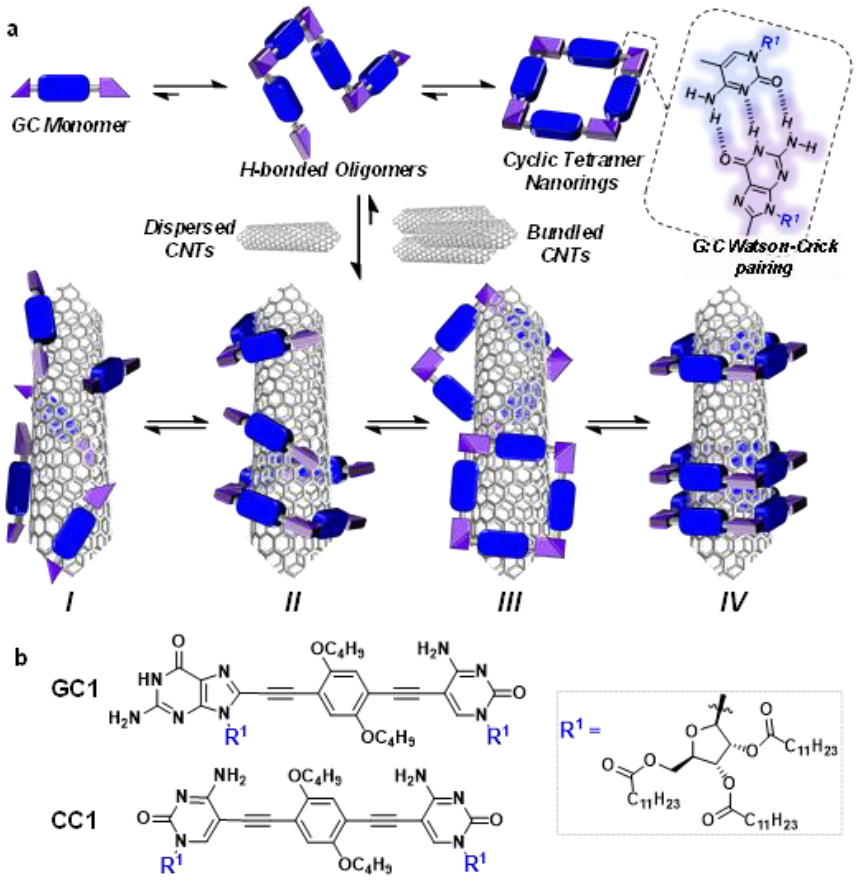

Figure 1. (a) Overall equilibria established between **GC** monomers and CNTs. Top: **GC** associates to yield a distribution of H-bonded supramolecular oligomers *via* Watson-Crick pairing, among which the cyclic tetramer is predominant due to a high chelate cooperativity. These species can in principle stabilize CNT dispersions through (I) monomer-CNT, (II) oligomer-CNT, (III) external nanoring-CNT, or (IV) threaded nanoring-CNT van der Waals interactions. (b) Structure of **GC1** and **CC1** monomers.

Our design focuses on a dinucleoside monomer (**GC1**; Figure 1b) that has been rationally designed and synthesized by González-Rodríguez's group to comply with these objectives. **GC1** structure consists of complementary guanosine (G) and cytidine (C) DNA bases connected by a rigid, linear central block. They demonstrated recently that related molecules self-assembled into cyclic tetramer species[42] through Watson-Crick G-C H-bonding interactions[43] exhibiting record chelate cooperativities,[44,45,46] which allow the nanorings to be formed quantitatively in nonpolar solvents within a wide concentration range.[47,48,49,50] The ribose groups in **GC1** feature multiple long alkyl chains that, upon cyclic assembly, would point in all directions towards the exterior medium, which should benefit individual CNT debundling and thus afford high solubility to the final composites. The monomer-CNT interaction strength is an additional key factor in our design. A π-conjugated dialkoxyarene central block with modest affinity for the CNT surface has been installed between the lipophilic bases. The idea is that stable dispersions would only be obtained if the rings are able to embrace the tube, so that its sidewalls can interact with several monomers in the nanoring cavity (mode IV in Figure 1), and not through external binding with sections of the rings (mode III) or with individual monomers or linear oligomers (modes I/II). We also explore herein the special synergy of the **GC1**-SWCNT marriage, which simultaneously brings an enhanced

[42] N. Bilbao, I. Destoop, S. De Feyter, D. González-Rodríguez, *Angew. Chem. Int. Ed.* **2016**, *55*, 659-663.
[43] J. Camacho-García, C. Montoro-García, A. M. López-Pérez, N. Bilbao, S. Romero-Pérez, D. González-Rodríguez, *Org. Biomol. Chem.* **2015**, *13*, 4506-4513.
[44] C. A. Hunter, H. L. Anderson, *Angew. Chem. Int. Ed.* **2009**, *48*, 7488-7499.
[45] G. Ercolani, L. Schiaffino, *Angew. Chem. Int. Ed.* **2011**, *50*, 1762-1768.
[46] M. J. Mayoral, N. Bilbao, D. González-Rodríguez, *ChemistryOpen* **2016**, *5*, 10-32.
[47] C. Montoro-García, J. Camacho-García, A. M. López-Pérez, N. Bilbao, S. Romero-Pérez, M. J. Mayoral, D. González-Rodríguez, *Angew. Chem. Int. Ed.* **2015**, *54*, 6780-6784.
[48] S. Romero-Pérez, J. Camacho-García, C. Montoro-García, A. M. López-Pérez, A. Sanz, M. J. Mayoral, D. González-Rodríguez, *Org. Lett.* **2015**, *17*, 2664-2667.
[49] C. Montoro-García, J. Camacho-García, A. M. López-Pérez, M. J. Mayoral, N. Bilbao, D. González-Rodríguez, *Angew. Chem. Int. Ed.* **2016**, *55*, 223-227.
[50] C. Montoro-García, M. J. Mayoral, R. Chamorro, D. González-Rodríguez, *Angew. Chem. Int. Ed.* **2017**, *56*, 15649-15653.

solubility to the nanotubes (when compared to a related molecule that cannot cyclize: **CC1**) and an increased stability to the macrocycles. This synergy originates from the cooperative action of G-C H-bonding and monomer-nanotube van der Waals interactions, so we reasoned that the disturbance of any of these distinct noncovalent interactions would cause collapse of the supramolecular ensemble, thus facilitating the recovery of the extracted CNTs.

4.2. Results and Discussion

Initial experiments and sample preparation

Prior to their combination with CNTs, we confirmed that this novel **GC1** monomer displayed a similar self-assembly process to the one already reported by González-Rodríguez's group with closely related dinucleosides (see the Experimental Section for further details).[47,50] NMR and optical spectroscopy experiments indicated that **GC1** tetrameric rings are indeed formed close to quantitatively in apolar chlorinated solvents within the 10^{-1} to 5 x 10^{-4} M concentration range. These cyclic assemblies are characterized by red-shifted and low intensity emission maxima at *ca.* 505 nm, and by the presence of a characteristic negative Cotton effect, with maxima at 340 and 387 and a minimum at 428 nm. At lower concentrations, they dissociate gradually into monomeric species, which display distinct emission maxima at 421 and 445 nm and null circular dichroism (CD) signals (*vide infra*). The addition of polar cosolvents that can compete for H-bonding, like DMSO or DMF, also results in monomer dissociation. The ^{1}H NMR spectra of **GC1** recorded by modifying the $CDCl_3$: DMF-D_7 volume ratio (Figure S1 in the Experimental Section) revealed a strong all-or-nothing behavior: no significant participation of any other H-bonded oligomer but the tetrameric macrocycle is

detected in solution. This is in agreement with the formation of stable ring species with remarkably high chelate cooperativities, as determined in their previous work.

An initial theoretical study using DFT calculations (see below and the Experimental Section for further details) served to properly design the interacting ring-tube system and experimental measurements. We decided to use (6,5)-enriched SWCNTs because they should fit adequately within the **GC1** nanoring cavity. These SWCNTs present a mean diameter of 0.7 nm and very narrow polydispersity, as we note in photoluminescence experiments (Figure 2c). In their Raman spectrum we can observe the strongest features of (6,5)SWCNTs (Figure 2a): the G-band at 1591 cm^{-1}, corresponding with the stretching of the C-C bond, common to all sp^2 carbon systems; the D-band at 1301 cm^{-1} and the 2D-band at 2600 cm^{-1}, due to one- and two-phonon, respectively, second-order Raman scattering processes; and the radial breathing modes (RBM) around 290 cm^{-1}, characteristic for this SWCNT chirality. Regarding the absorption spectrum of these nanotubes, S_{22} transitions are shown in the visible region, while the S_{11} transitions appear in the nIR region, with maxima at 572 and 988 nm (Figure 2b).

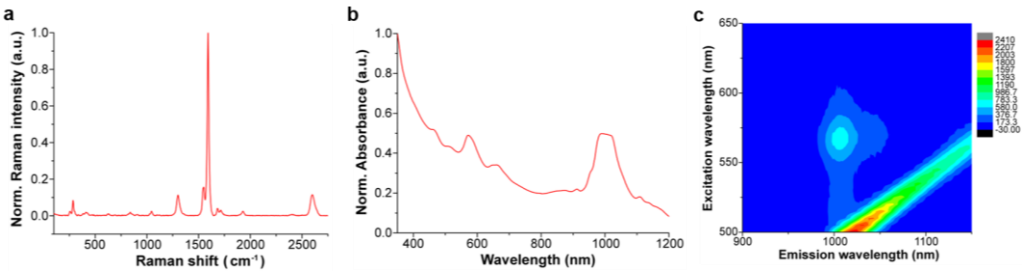

Figure 2. (a) Raman spectrum (λ_{exc} = 633 nm), (b) absorption spectrum (D_2O, 1% SDS, 298 K), and (c) PLE intensity map (λ_{exc} = 572 nm) (D_2O, 1% SDS, 298 K) of pristine (6,5)-enriched SWCNTs. All spectroscopic data support a sample which is nearly exclusively semiconducting, with (6,5) as the main chirality present, as stated by the provider.

Thus, a dispersion of (6,5)SWCNTs in $CHCl_3$ (0.2 mg mL^{-1}) was produced first by ultrasonication followed by centrifugation, in order to remove large SWCNT bundles and any other carbonaceous impurities. These non-stabilized dispersions are rather short-lived and significant precipitation of (6,5)SWCNTs was clearly observed after a few hours (see central image in Figure 3a). Immediately after centrifugation, **GC1** (or **CC1**) solutions in $CHCl_3$ (different concentrations were tested, from 5.0 x 10^{-4} to 10^{-6} M) were added to the supernatant (6,5)SWCNT dispersion and the mixtures were stirred at room temperature. The (6,5)SWCNT-**GC1** suspensions produced (right image in Figure 3a) were kept under dark and checked at different periods of time. A few spectroscopic changes were observed within the first hours after mixing, but after *ca.* 12 hours spectral properties remained constant for weeks and are reproducible.

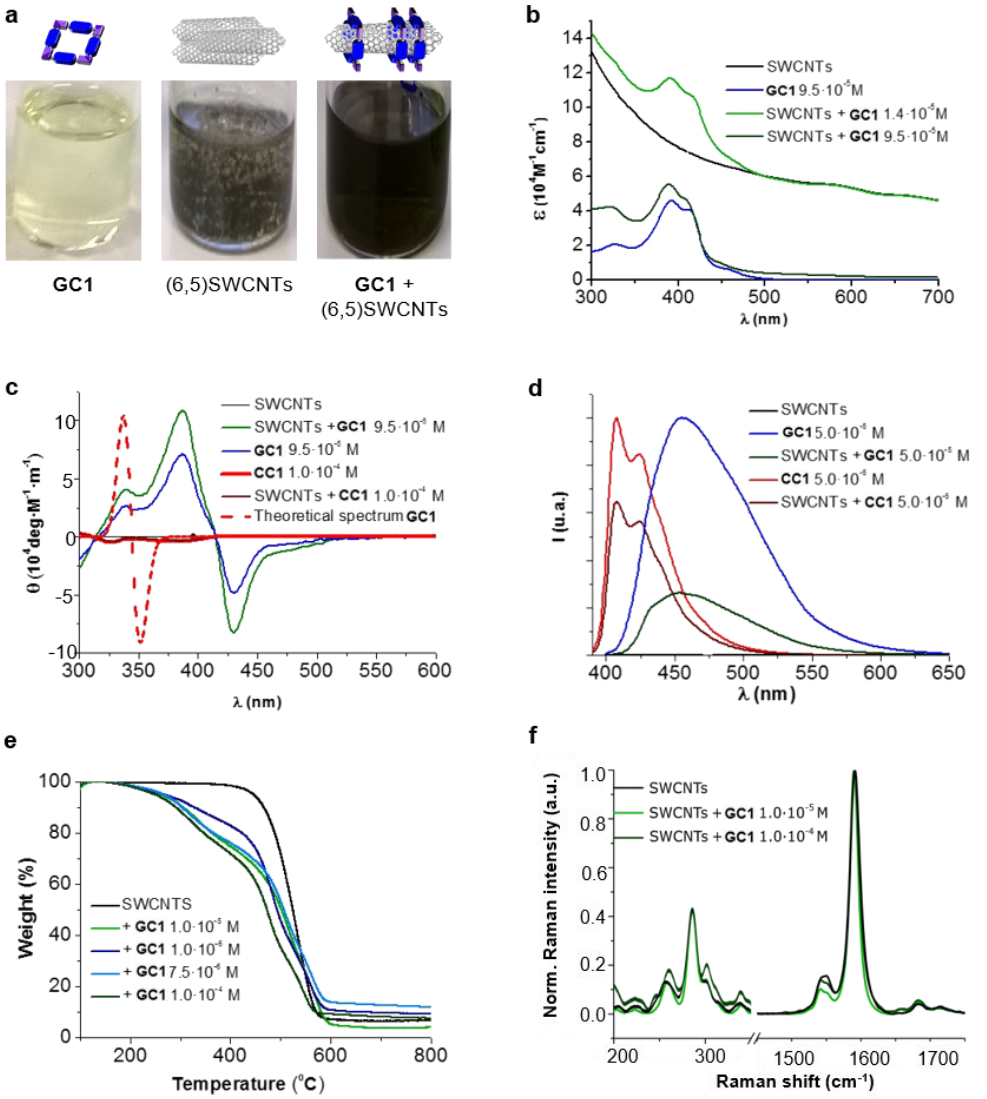

Figure 3. (a) From left to right: image of the solutions/dispersions containing **GC1** (9.5 x 10^{-5} M), (6,5)SWCNTs (0.2 mg mL^{-1}) and their mixture in $CHCl_3$. (b-f) Absorption (b), CD (c), and emission spectra (λ_{exc} = 380 nm) (d), TGA analyses (air, 50 °C min^{-1}) (e), and Raman spectra (λ_{exc} = 633 nm) (f) of samples containing **GC1**/**CC1**, pristine (6,5)SWCNTs, or the products formed by their mixture at different concentrations.

Spectroscopic and thermogravimetric measurements

The (6,5)SWCNT-**GC1**/**CC1** composites were analyzed by absorption, CD, Raman and emission spectroscopies and by TGA, and compared with pristine (6,5)SWCNTs and **GC1**/**CC1** in the same conditions (Figure 3). The absorption spectra (Figure 3b) showed the typical features of both components in the mixture and only minor deviations in absorption maxima were noted. The typical scattering phenomena, evidenced by a baseline rise, was notorious in the original (6,5)SWCNT dispersions and in mixtures with low **GC1** content. However, as the **GC1**/(6,5)SWCNTs ratio is increased, scattering is concomitantly reduced until it is no longer perceptible in the absorption spectrum, which underlines the high dispersing power of this agent. As a matter of fact, the **GC1**-(6,5)SWCNTs mixtures produced are clear suspensions (Figure 3a) that show no evidence for nanotube precipitation along several weeks.

CD can be considered as one of the most powerful techniques for stereochemical analysis: it is sensitive to the absolute configuration as well as to conformational features, which are often completely obscured in ordinary absorption spectra.[51] Regarding this, the CD spectral shape of **GC1**-(6,5)SWCNTs composites does not exhibit important differences with **GC1** in the same conditions (Figure 3c). This is a strong indication that the cyclic tetramer structure is preserved in the presence of (6,5)SWCNTs, and no dissociation or structural change in the H-bonded assembly was noted. In order to obtain additional proof from a theoretical perspective, we calculated the CD spectrum for the optimized structure of c**GC1**$_4$ (see Figure 4g below), which is displayed as a dotted red line in Figure 3c. Our calculations revealed a strong dependency of the CD spectra with the symmetry of the macrocycle. Only when the C_4 axis was maintained in the c**GC1**$_4$ ring structure, we obtain a good match between the experimental and the theoretical results (with

[51] N. Berova, K. Nakanishi, R. Woody, *Circular Dichroism: Principles and Applications*, Wiley, **2000**.

the exception of the vibronic structure of the positive Cotton effect). If the C_4 symmetry axis is lost, due for instance to other binding modes of **GC1** to the CNT sidewalls, the CD spectrum is significantly perturbed. As an example, we show in Figure S2 in the Experimental Section the structure and calculated spectrum for a c**GC1**$_4$ structure, which is close in energy, but has lost the C_4 symmetry. We can therefore conclude that this C_4 symmetry is conserved upon the formation of (6,5)SWCNT-c**GC1**$_4$ conjugates, which is a strong indication that the SWCNT is inside the cavity of c**GC1**$_4$ ring.

Another important proof that demonstrates **GC1**-(6,5)SWCNTs interactions came from comparing the emission spectra (Figure 3d) with and without CNTs. As a matter of fact, **GC1** fluorescence is considerably quenched in the presence of (6,5)SWCNTs. This is very characteristic in noncovalent SWCNT assemblies[22] and is presumably caused by an energy transfer process between the dinucleoside π-conjugated system and the SWCNT when they are in close contact.

On the other hand, TGA studies showed that macrocycle loading increases with **GC1** concentration, to yield 17% and 28% loading at 10^{-6} and 10^{-4} M **GC1** initial concentration, respectively (Figure 3e). Finally, no significant (6,5)SWCNT electronic perturbance was noted in Raman experiments when **GC1** or **CC1** were added (Figure 3f), which is a good indication of the formation of noncovalently bound composites.

Structural analysis: microscopy and DFT

Exploration of the **GC1**-SWCNT suspensions under atomic force microscopy (AFM) was consistent with a picture in which the SWCNTs are encapsulated within **GC1** macrocycles. AFM images were obtained upon spin-coating the SWCNT suspensions on mica, and show individualized SWCNTs decorated with objects of about 2 nm in height (Figures 4a and b), in full accord with the DFT-modelled size of

the **GC1** tetramer (Figure 4h). We also explored our samples under transmission electron microscopy (TEM), where we observe mostly re-bundled SWCNTs, most likely due to sample preparation issues. However, wherever individualized SWCNTs were located, they showed heavily functionalized sidewalls (Figures 4c and d). Unfortunately, and in contrast to covalently linked macrocycles,[41] attempts at obtaining higher resolution TEM images were precluded by the instability of the H-bonded organic macrocycle in the conventional transmission electron microscope at 200 kV. High resolution images were obtained in an aberration corrected microscope at 60 kV (Figures 4e and f). We observe structures of around 2.0 nm surrounding the SWCNTs that are consistent with the picture provided by spectroscopy, but even under low voltage (see also Figure S4 in the Experimental Section),[52,53,54] the macrocycles were observed to quickly reorganize and eventually decompose under the electron beam irradiation, probably due to radiolysis damage associated to hydrogen.

Further theoretical studies were performed in order to gain a deeper insight into the structure and interactions in the (6,5)SWCNT-c**GC1**$_4$ composites. As explained above, the optimized geometry of c**GC1**$_4$ belongs to the C_4 point group of symmetry and is depicted in Figure 4g. The inner cavity has a mean diameter of 2.1 nm and the central aromatic moieties are bent at an angle of 30°, so that planarity is not conserved, allowing the carbon nanotube to maintain a stronger interaction with the ring. In order to have a second proof of the arrangement between the two moieties, we additionally calculated the intensity of the interaction between SWCNTs and c**GC1**$_4$ ring with close π-π contacts in the range of 3.2-3.5 Å. Among the

[52] T. W. Chamberlain, J. Biskupek, S. T. Skowron, P. A. Bayliss, E. Bichoutskaia, U. Kaiser, A. N. Khlobystov, *Small* **2015**, *11*, 622-629.
[53] E. Nakamura, *Angew. Chem. Int. Ed.* **2013**, *52*, 236-252.
[54] T. W. Chamberlain, J. Biskupek, S. T. Skowron, A. V. Markevich, S. Kurasch, O. Reimer, K. E. Walker, G. A. Rance, X. Feng, K. Müllen, A. Turchanin, M. A. Lebedeva, A. G. Majouga, V. G. Nenajdenko, U. Kaiser, E. Besley, A. N. Khlobystov, *ACS Nano* **2017**, *11*, 2509-2520.

different possible configurations (see Figure S3 in the Experimental Section), we observed that the (6,5)SWCNT and the c**GC1**$_4$ tetramer interact strongly (E_{int} = -22.7 kcal mol^{-1}) when the macrocycles are clamping the nanotube and the macrocycle tilts slightly with respect to the tube axis, in order to maximize non-covalent interactions (interaction mode IV in Figure 1). In contrast, all external binding modes investigated (interaction mode III in Figure 1), result in positive (*i.e.* disfavorable) interaction energies ranging between +0.7 and +42.0 kcal mol^{-1}. The geometry of the lowest energy configuration is shown in Figure 4h.

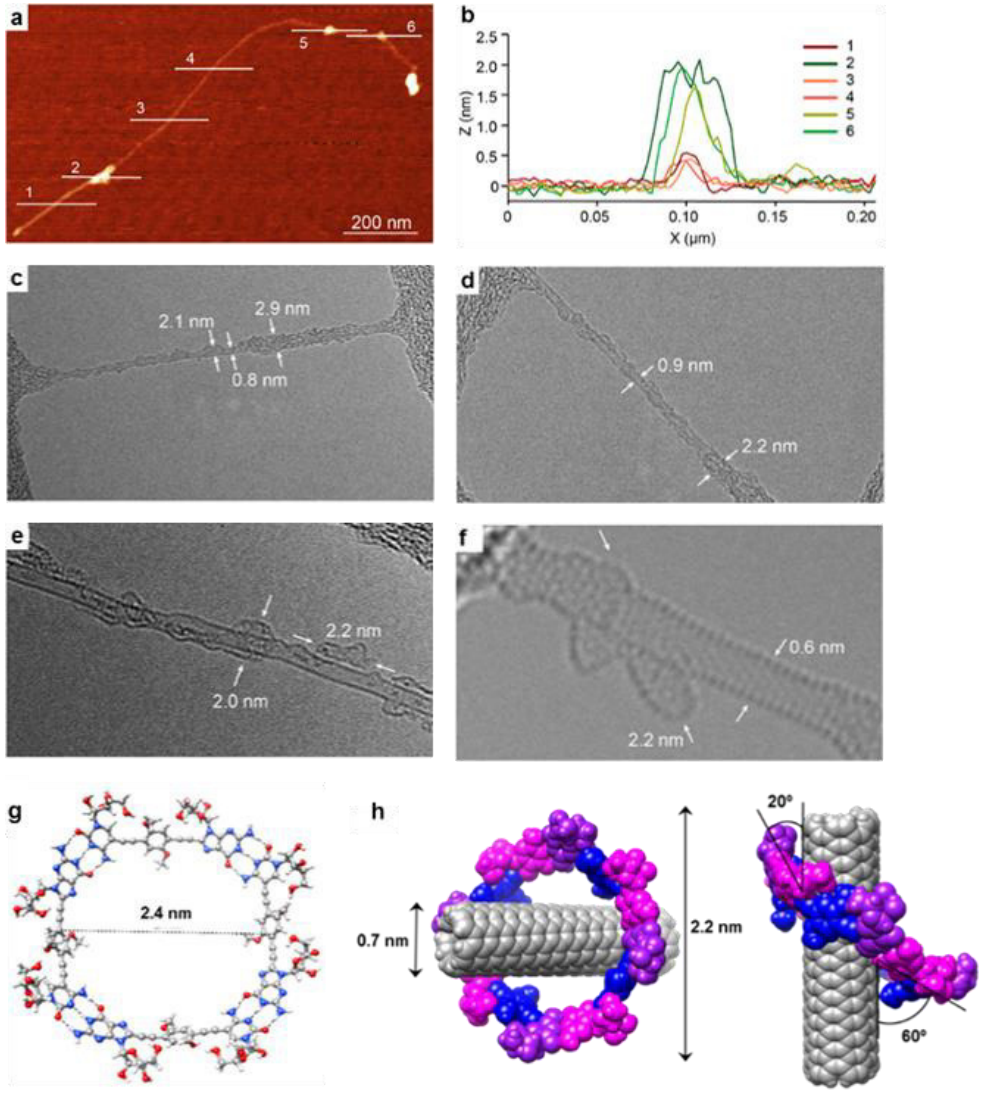

Figure 4. (a) Representative AFM topographic image of a suspension of the product formed by the mixture of (6,5)SWCNTs with **GC1** in TCE. (b) Height profiles along the lines marked in (a) show individualized SWCNT (0.7 nm) decorated with objects that are consistently 2 nm high. (c-f) Representative TEM images of an individual SWCNT. Note that the sidewalls are functionalized symmetrically by a low-contrast addend that shows a total diameter of 2-3 nm, consistent with encapsulation by the **GC1** macrocycles. (g) DFT-optimized structure of a c**GC1**$_4$ ring. (h) Lowest energy configuration of the (6,5)SWCNT-c**GC1**$_4$ composite, showing diverse geometric parameters.

Analysis of the synergistic interactions

Concentration-dependent experiments, where we recorded absorption, CD and emission spectra, provided a deeper understanding of the mutual interaction between CNTs and H-bonded nanorings. Two parallel dilution measurements were conducted from **GC1** $CHCl_3$ solutions: one in the absence (Figures 5a and c) and the other one in the presence of (6,5)SWCNTs (Figures 5b and d). The spectral changes with concentration were monitored from 4.0 x 10^{-4} M (blue lines) down to 3.0 x 10^{-6} M (CD) or down to 2.0 x 10^{-7} M (emission) (red lines). The trends obtained from both techniques are compared in Figure 5i.

A first experimental observation that came from comparison of both dilution experiments is that the presence of (6,5)SWCNTs preserved the characteristic cyclic tetramer features along a wider concentration range. This is unambiguously observed in the evolution of the CD spectra as a function of concentration. While **GC1** CD features readily disappear below *ca.* 10^{-5} M (Figure 5a), indicating cyclic tetramer dissociation,[47,48,49,50] they remain distinct down to 3 x 10^{-6} M in the presence of (6,5)SWCNTs (Figure 5b). The degree of cyclotetramerization, that is, the molar fraction of **GC1** molecules associated as cyclic tetramers (horizontal equilibria in Figure 1a), can be calculated from each dilution experiment by integrating CD intensity. The comparison of both trends, represented with solid blue and green circles in Figure 5i, suggests that **GC1** nanorings are significantly stabilized when mixed with (6,5)SWCNTs. Fitting these data to cyclotetramerization processes (blue and green lines in Figure 5i) afforded cyclotetramerization constants (K_T) in the order of K_T = 3.2 x 10^{14} M^{-3} for **GC1** and K_T = 4.0 x 10^{16} M^{-3} for **GC1** + (6,5)SWCNTs. That is, chelate cooperativity greatly benefits from the presence of SWCNTs and nanoring stability is considerably increased.

We then turned our attention to the evolution of the fluorescence features in these dilutions experiments. The emission spectra were analyzed in two different ways, attending to: (1) their relative intensity, which can be correlated to the fraction of CNT-bound molecules (vertical equilibrium in Figure 1a), or (2) the spectral shape and emission wavelength, which reports again on the degree of cyclotetramerization (horizontal equilibria in Figure 1a). In the first case, we compared **GC1** emission intensity in the 400-650 nm range in the absence (I_{GC}) or presence ($I_{GC\text{-}CNT}$) of (6,5)SWCNTs at each concentration (see Figure S5A in the Experimental Section). The degree of emission quenching, defined as 1 - $I_{GC\text{-}CNT}/I_{GC}$, was then calculated and plotted as red squares in Figure 5i. Since energy transfer from the photoexcited dinucleoside molecules to the CNT is close to quantitative when they are closely interacting, as determined from the fully quenched emission of the samples at high concentration, these curves actually reveal the molar fraction of **GC1** that is bound to (6,5)SWCNTs at each concentration. Our results show that **GC1**-(6,5)SWCNTs association is virtually quantitative at concentrations above 10^{-4} M and then falls in the 10^{-4} to 10^{-6} M range. This nonlinear trend suggests a cooperative **GC1**-(6,5)SWCNT interaction that seems to be coupled to the cyclotetramerization equilibrium. In order to compare our **GC** monomer with a related dispersing agent that does not associate in cyclic systems, we carried out another set of parallel dilution experiments with **CC1** in the absence and presence of (6,5)SWCNTs. The degree of emission quenching was likewise calculated at each concentration and the results are shown as orange squares in Figure 5i (see also Figure S5B in the Experimental Section). The **CC1**-(6,5)SWCNTs association is clearly weaker and no longer detected below 10^{-5} M, a concentration where *ca.* half of the **GC1** molecules are still bound to CNTs.

In the second case, the degree of cyclotetramerization was estimated by analysing the shape of each normalized fluorescence spectra during the dilution measurements shown in Figures 5c and d, as we described in previous works.[47,50] As

commented above, when the monomeric species, showing emission maxima at 421 and 445 nm in $CHCl_3$ (see red spectra in Figures 5c and d), associate in cyclic tetramers, a red-shift to >500 nm and a reduction in emission intensity is noted. The results obtained at each concentration are also included in Figure 5i as solid green and blue triangles for the **GC1** samples without and with CNTs, respectively. The cyclic tetramer association trends calculated by CD and fluorescence spectroscopy (green circles and triangles) display a quite decent correlation for **GC1**. That is not the case when (6,5)SWCNTs are present (please compare blue circles and triangles), and this is because CD and emission spectroscopy are not reporting on the same **GC1** population. Whereas the measured CD spectra is representative of all **GC1** molecules in solution, the emission spectra primarily provide information of the fraction of molecules that are not bound to the CNTs, since the emission of the **GC1** molecules that are bound is strongly quenched. As a consequence, the shape evolution of the emission spectra when the CNTs are present exhibits again a strong coupling between the horizontal cyclotetramerization and vertical **GC1**-(6,5)SWCNT association equilibria in Figure 1a. At concentrations above 10^{-4} M most **GC1** molecules are bound to the CNTs and the residual emission recorded is extremely weak in intensity and representative of the cyclic tetramer in shape and emission wavelength (see blue spectrum in Figure 5d as an example). However, when **GC1**-(6,5)SWCNT association is no longer quantitative in the 10^{-4} to 10^{-6} M range, the emission spectra becomes rapidly dominated by the fraction of **GC1** molecules that are not bound to CNTs, which have stronger monomer-like features (red spectrum in Figure 5d) because their actual concentration is lower. This is reflected in a very sharp transition around 10^{-4} M in the blue-triangle trend in Figure 5i. In other words, in the 10^{-4} to 10^{-6} M range, the shape of the emission spectrum is more shifted to the monomer features in the presence of CNTs, since the actual concentration of emissive **GC1** molecules (*i.e.* not bound to CNTs) is lower than in the absence of CNTs. Only when the **GC1**-(6,5)SWCNT interactions become no longer important,

below 10^{-6} M, samples with and without CNTs display similar emission intensity and shape (see also Figure S5A in the Experimental Section).

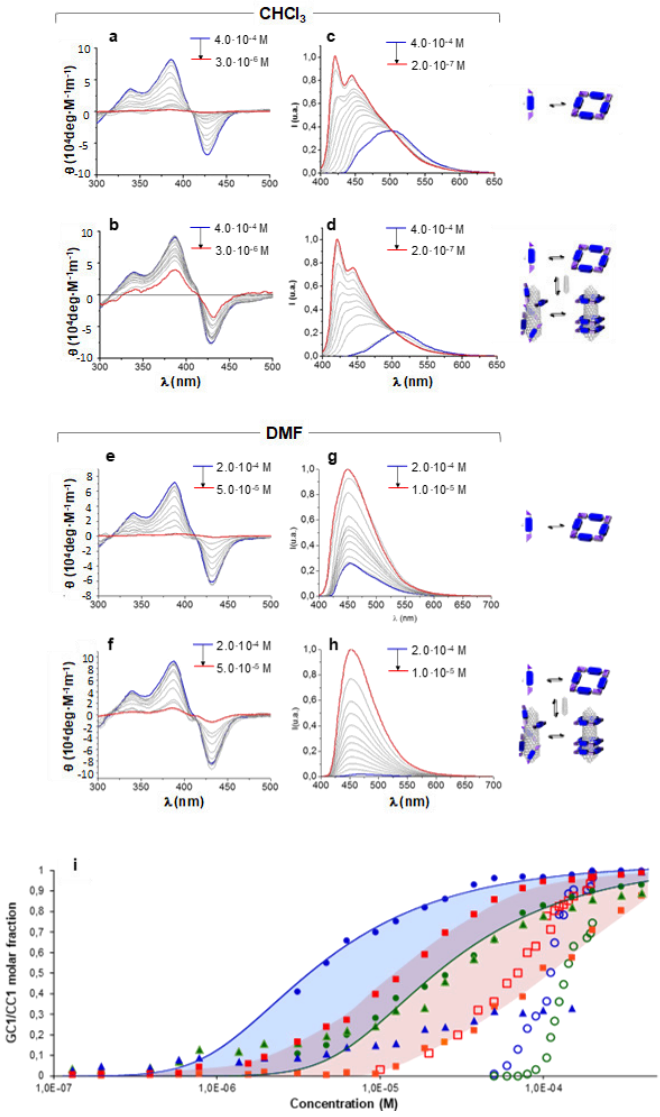

Figure 5. CD (a, b, e and f) and normalized emission (c, d, g and h) spectra of **GC1** in the absence (a, c, e and g) or presence (b, d, f and h) of (6,5)SWCNTs recorded at different concentrations in dilution experiments with $CHCl_3$ (top panel) or DMF (bottom panel). Initial and final concentrations are indicated in blue and red, respectively. (i) Representation of: (1) the molar fraction of **GC1** molecules that are assembled as cyclic tetramers, as determined by CD (circles) or emission spectroscopy (triangles) in the absence (green) or presence (blue) of (6,5)SWCNTs, or (2) the molar fraction of **GC1** (red squares) or **CC1** (orange squares) molecules that are bound to (6,5)SWCNTs, as estimated from the degree of emission quenching. Dilution experiments were made in $CHCl_3$ (solid shapes) or DMF (open shapes). The CD trends in $CHCl_3$ were fitted to cyclotetramerization models (blue and green lines).

We believe the graph in Figure 5i provides a rather faithful description of the self-assembly of this two-component mixture in solution as a function of concentration. The results gathered from these dilution experiments in $CHCl_3$ clearly indicate that each species benefits synergistically from the presence of the other, as it is schematically represented in Figure 6. On one hand, the nanorings are more stable in the presence of nanotubes, a gain that is represented by the blue area in Figure 5i. On the other, the nanotubes can host a higher number of dispersing agent molecules and thus enjoy enhanced solubility along a broader concentration range when the monomer cyclizes, a gain that is represented by the red area in Figure 5i when comparing **GC1** and **CC1**. In short, H-bonding between complementary bases and van der Waals dispersion forces between monomer and the π-conjugated CNT sidewalls are noncovalent interactions that work here cooperatively to build strongly-associated **GC1**-(6,5)SWCNTs composites. It is interesting to note that smaller nanorings, where the nucleobases are directly connected by a triple bond (see **GC3** in the Experimental Section), whose cavities cannot host (6,5)SWCNTs, do not exhibit the same synergic effects as **GC1**, but rather behave as a regular dispersing agent, like **CC1**. On the other hand, **GC1** cannot solubilize as efficiently multi-walled nanotubes of larger diameter. Both observations are in agreement with the clamping interaction mode IV, shown in Figures 1a and 6, being the most likely and abundant in $CHCl_3$ solutions (Figure 1a). We should nonetheless consider that, when the nanorings are assembled around the tube, local concentration effects may occur, so that a rearrangement into linear polymers may take place when several rings coincide locally. However, these ring-to-chain rearrangements should lead to a reduction in CD intensity at high concentrations that we did not observe, so we can discard this is a relevant situation. As we reduce concentration, these effects are even less likely to occur, because the rings are favoured entropically.

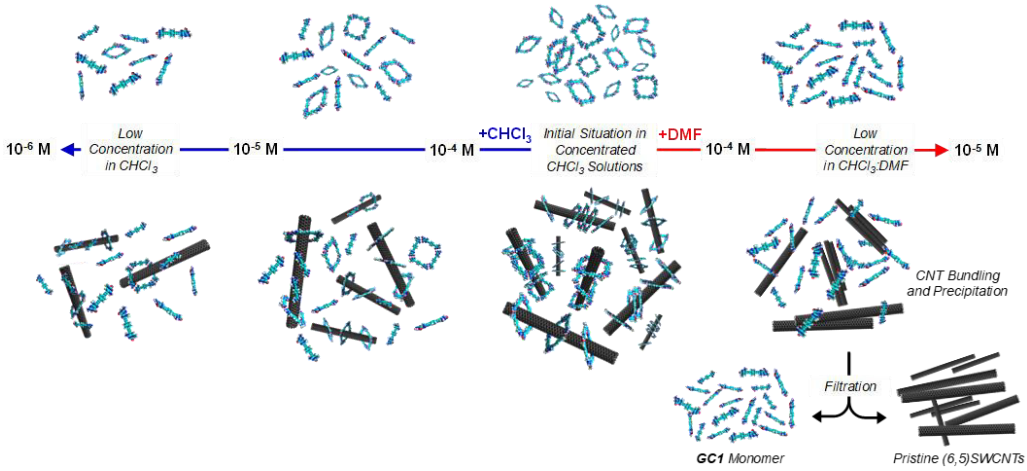

Figure 6. Schematic representation of the dilution processes in $CHCl_3$ (left) and DMF (right) without (top) and with (6,5)SWCNTs (bottom). At high concentrations in $CHCl_3$, **GC1** ring assemblies are formed quantitatively and establish strong interactions with the CNTs. Upon dilution with $CHCl_3$ the cyclic tetramers gradually dissociate, but such dissociation occurs to a lower extent when CNTs are present, due to the stronger (6,5)SWCNT-c**GC1**$_4$ clamping interactions. On the contrary, upon dilution with DMF, the c**GC1**$_4$ rings are fully dissociated at relatively high concentrations, which eventually produces CNT precipitation due to the weaker interaction of **GC1** monomers with the (6,5)SWCNTs. In this last situation, a simple filtration and washing protocol allows to separate efficiently the (6,5)SWCNTs from the **GC1** monomer.

Recovery of the pristine SWCNTs

At this point we reasoned that the whole assembly could be demolished by addressing just one of the supramolecular interactions, which could be a simple and straightforward strategy for pristine (6,5)SWCNTs recovery. For instance, an increase in solvent polarity should disrupt H-bonding interactions without strongly affecting monomer-(6,5)SWCNTs van der Waals interactions. In order to prove this, we performed now the same dilution experiments from **GC1** samples with and without CNTs by gradual addition of DMF instead of $CHCl_3$, and recorded again nanoring dissociation by CD (Figures 5e and f; open green and blue circles,

respectively, in Figure 5i), and the degree of emission quenching by fluorescence spectroscopy (Figures 5g and h; open red squares in Figure 5i).

In line with the previous observations, the cycles are more stable and the CD features resist a higher amount of DMF when (6,5)SWCNTs are present (please compare open blue and green circles). Together with the disappearance of the CD signals, **GC1** monomer emission was recovered in a narrower concentration range when the parent **GC1**-(6,5)SWCNTs dispersion was diluted with DMF instead of $CHCl_3$ (please compare solid and open red squares), which suggests much weaker interactions with the CNTs in this polar solvent. Interestingly, after several minutes after DMF addition a clear precipitate emerged from the original dispersion that, after washing, showed no residual **GC1** spectroscopic features. Despite the strong association and remarkable endurance of the **GC1**-(6,5)SWCNTs solutions in $CHCl_3$, which can last for several weeks maintaining the original optical quality, CNT rebundling and precipitation occurred rapidly in DMF, likely due to the lower efficiency of the dissociated monomer as a dispersing agent (see Figure 6). It is also interesting to note that c**GC1**$_4$ dissociation can also be induced by increasing the temperature in $CHCl_3$ or $CHCl_2CHCl_2$ solutions. After being subjected to a heating-cooling cycle the spectra of the initial and final samples differed considerably and clear precipitation of the CNTs was noted. However, the results are highly dependent on the concentration and not as reproducible and efficient as the addition of DMF to release and recover the pristine (6,5)SWCNTs.

4.3. Conclusions

In conclusion, we have explored herein an unprecedented approach to solubilize SWCNTs in apolar solvents that relies on dynamic macrocycle clamping around the nanotube sidewalls, which allows for efficient SWCNT debundling, and

on cooperative noncovalent interactions, which supplies the required reversibility to simply and effectively recover the pristine material. The combination of theoretical DFT-based methodologies, spectroscopic techniques, as well as AFM and TEM microscopies, provide solid evidence for a preferred association mode where the H-bonded nanorings are embracing the tube (mode IV in Figure 1). Furthermore, a comparison between dilution experiments performed on **GC1** in the absence or presence of (6,5)SWCNTs provided a deep insight into the mutual benefits offered by the combination of these two species. On one hand, nanoring stability is unambiguously enhanced in the presence of the CNTs, likely due to the interaction of more than one **GC1** monomer with the tube sidewalls. On the other, the **GC1** molecule exhibited an extraordinary solubilizing power, in comparison with a regular dispersing agent that cannot cyclize, like **CC1**. When comparing these two monomers, we observe dramatic differences in terms of the quality of the dispersions produced (that only show very low scattering in the case of **GC1**; see Figure 3b), their durability (the dispersions produced from **CC1** show a CNT precipitate after a few days, while those from **GC1** were seen to resist for many weeks), and the resistance of the monomer-SWCNT interaction to dilution (as determined from the experiments shown in Figure 5). We believe that these remarkable differences, which are translated in the generation of clear, long-lasting (6,5)SWCNTs dispersions along a broad concentration range, can only be explained if the dispersing agent is able to surround individual nanotubes, as in mode IV in Figure 1.

Future efforts will be directed to study if our self-assembled nanorings can selectively extract CNTs as a function of diameter and chirality.

4.4. Experimental Section

General. UV-visible experiments were conducted using a JASCO V-660 apparatus. Emission spectra were recorded in a JASCO FP-8600 equipment using excitation and emission bandwidths of 5 nm in both cases, and a 50 ms response. CD spectra were recorded with a JASCO V-815 equipment. The slit width was set at 1000 µm and a DIT of 2 s was used. In all these three instruments the temperature was controlled using a JASCO Peltier thermostatted cell holder with a range of 263-383 K, adjustable temperature slope, and accuracy of ± 0.1 K. Raman spectra were acquired with a Bruker Senterra confocal Raman microscopy instrument, equipped with 532, 633 and 785 nm lasers. Thermogravimetric analyses (TGA) were performed using a TA Instruments TGAQ500 with a ramp of 50 °C/min under air from 100 to 1000 °C. Transmission electron microscopy (TEM) images were obtained with a JEOL-JEM 2100F (2.5 Å resolution) instrument operating at 200 kV. Aberration corrected HR-TEM images were obtained with a GRAND ARM300cf JEOL instrument operating at 60 kV. Atomic force microscopy (AFM) images were obtained with JPK NanoWizard II instrument, coupled to an inverted optical microscope Nikon Eclipse Ti-U.

Monomer structure

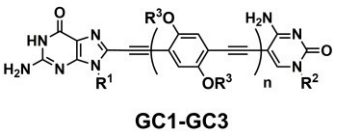

GC1-GC3

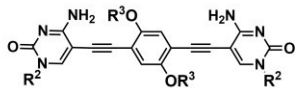

CC1

	R^1	R^2	R^3
GC1 (n=1)	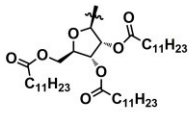	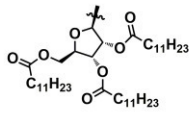	C_4H_9
GC2 (n=1)	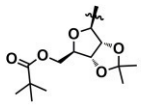	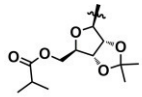	C_4H_9
GC3 (n=0)	C_2H_5	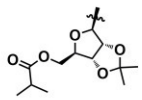	
CC1 (n=1)		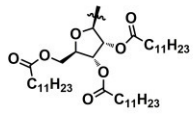	C_4H_9

Monomers **GC1** and **CC1** were rationally designed and synthesized by R. Chamorro to comply with our objectives. Monomers **GC2** and **GC3** had been synthesized previously,[47] also by González-Rodríguez's group.

Preliminary study of the self-assembly behavior of GC1

Prior to its combination with CNTs we wanted to confirm that the new **GC1** monomer followed a similar self-assembly process to the one already reported by González-Rodríguez's group with closely related dinucleosides.[47] 10^{-2}-10^{-5} M solutions of **GC1** in $CDCl_3$ or $CDCl_2CDCl_2$ displayed ^1H NMR spectra that are characteristic of quantitative G-C H-bonding, as confirmed by NOESY NMR (Figure

S1a), with G-H and C-H H-bonded protons appearing around 13.4 ppm and 10.0 ppm, respectively (see as an example the bottom spectrum in Figure S1b). In contrast to G-C supramolecular polymers or 1:1 mixtures of G and C mononucleosides, the shape and position of these two H-bonded signals do not change significantly with concentration, temperature or small solvent composition variations. This finding is already an indication that an especially stabilized H-bonded species are present in solution, whose size, estimated by DOSY NMR and ESI Q-TOF experiments in their previous work,[47] matches the one expected for a cyclic tetramer. Further corroboration was obtained by adding increasing amounts of a polar solvent that can compete for the H-bonding sites, like DMSO or DMF, which results in monomer dissociation. The ^{1}H NMR spectra recorded along these titrations (Figure S1b) is again markedly different to the one that would be expected for a H-bonded supramolecular polymerization and reveal a strong all-or-nothing behavior. Only monomer and cyclic tetramer species are detected in slow exchange at the NMR timescale, which is in agreement with the formation of a thermodynamically and kinetically stable ring species with high chelate cooperativity, as proven in their previous work.[47]

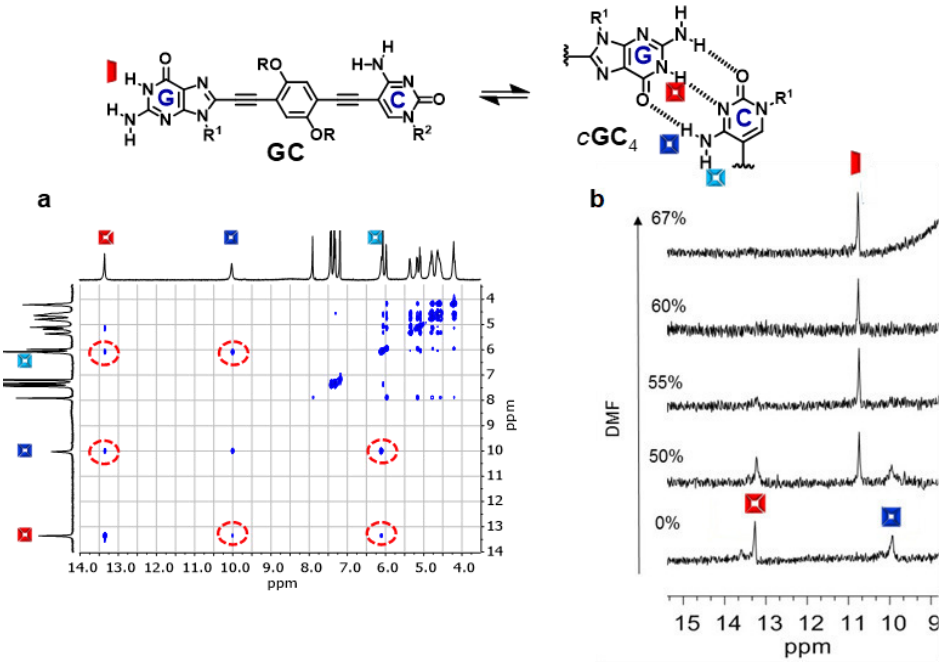

Figure S1. (a) Region of the NOESY NMR spectrum of **GC** in $CDCl_3$ (C = 1.0 x 10^{-2} M, T = 298 K), showing cross-peaks between the H-bonded G-amide and C-amine proton signals. (b) Evolution of the downfield region of the ^{1}H NMR spectra of **GC1** as the volume fraction of DMF-D_7 is increased in $CDCl_3$: DMF-D_7 mixtures at C = 3.0 x 10^{-3} M and T = 298 K. The cyclic tetramer in $CDCl_3$, showing the H-bonded G-amide (at *ca.* 13.4 ppm) and C-amine (at *ca.* 10.0 ppm) proton signals, is progressively dissociated into monomer species, that show a G-amide peak at *ca.* 10.8 ppm, as the DMF content is increased. Please note that the shape and position of each signal do not change significantly along these titrations, suggesting an equilibrium between two species (monomer and tetramer) in slow exchange at the NMR timescale, as determined in a previous work.[47]

The cyclotetramerization process can also be monitored by more sensitive techniques like absorption, emission and circular dichroism (CD) spectroscopy. **GC1** monomers display emission maxima at 421 and 445 nm and null CD signals. Compared to these features, **GC1** nanorings are spectroscopically characterized by red-shifted and low intensity emission maxima at 503 nm, and by the presence of a characteristic negative Cotton effect with maxima at 339 and 386 nm and a

minimum at 428 nm, which is originated by cyclic H-bonding assembly.[47] As in their previous work, a series of experiments performed as a function of sample concentration allowed us to estimate the degree of cyclotetramerization, that is, the molar fraction of **GC1** molecules assembled as cyclic tetramers in solution. In the case of the CD experiments, this is done by integrating the area of the CD spectra. For the emission experiments, this is carried out by analyzing the shape of the emission spectra. From our own experience in this and previous studies,[47] the best way to do this is to calculate the ratio between emission intensity above and below a chosen intermediate wavelength and correlate these values to those obtained with pure cyclic tetramer and pure monomer.

Altogether, NMR and optical spectroscopy experiments indicate that **GC1** cyclic tetramers are formed close to quantitatively in apolar chlorinated solvents at room temperature within the 10^{-2}-10^{-4} concentration range. At lower concentrations or upon addition of polar solvents, they dissociate gradually into monomeric species, a process that can be monitored spectroscopically giving rise to sigmoidal curves that can be fitted to a cyclotetramerization process.

Computational details

All theoretical calculations were carried out within the density functional theory (DFT) approach by using the C.01 revision of the Gaussian 09 program package.[55] Considering the two moieties of the final composites: (6,5)SWCNT and

[55] M. J. Frisch, G. W. Trucks, H. B. Schlegel, G. E. Scuseria, M. A. Robb, J. R. Cheeseman, G. Scalmani, V. Barone, B. Mennucci, G. A. Petersson, H. Nakatsuji, M. Caricato, X. Li, H. P. Hratchian, A. F. Izmaylov, J. Bloino, G. Zheng, J. L. Sonnenberg, M. Hada, M. Ehara, K. Toyota, R. Fukuda, J. Hasegawa, M. Ishida, T. Nakajima, Y. Honda, O. Kitao, H. Nakai, T. Vreven, J. A. Montgomery, J. E. Peralta, F. Ogliaro, M. Bearpark, J. J. Heyd, E. Brothers, K. N. Kudin, V. N. Staroverov, R. Kobayashi, J. Normand, K. Raghavachari, A. Rendell, J. C. Burant, S. S. Iyengar, J. Tomasi, M. Cossi, N. Rega, J. M. Millam, M. Klene, J. E. Knox, J. B. Cross, V. Bakken, C. Adamo, J. Jaramillo, R. Gomperts, R. E. Stratmann, O. Yazyev, A. J. Austin, R. Cammi, C. Pomelli, J. W. Ochterski, R. L. Martin, K. Morokuma, V. G. Zakrzewski, G. A. Voth,

GC1 tetrameric ring, we need to divide the modeling process in two stages. First, we investigate the stabilization of the **GC1** tetrameric ring by using the Coulomb-attenuated hybrid exchange-correlation functional (CAM-B3LYP). This functional was develop by Yanai et al.[56] which includes the Hartree-Fock and the Becke exchanges as a variable ratio depending of the intermolecular distance. It has been demonstrated that this method gives an improved description of long-range interactions and really good agreements between the experimental and theoretical circular dichroism spectra.[57,58,59] In the present study, we employed the CAM-B3LYP functional for the investigation of the stabilization and chiroptical properties of the **GC1** tetrameric ring. Electronic excitation energies of the **GC1** tetrameric ring were obtained by using the time-dependent DFT (TD-DFT) formalism[60,61] for which up to the 20 low-lying energy states were considered. Additionally, the **GC1** tetrameric ring was simplified by substituting -$OOCC_{11}H_{23}$ chains attached to the desoxyriboses by -OH. Also, the -OC_4H_9 chains attached to the benzene in the connector groups were reduced to -OCH_3, in order to reduce the computational cost. Secondly, the binding energy of (6,5)SWCNT-**GC1** composites was studied using the long-range corrected B97D density functional, which is able to incorporate the dispersion effects by means of a pair-wise London-type potential. The B97D[62] density functional has emerged as a robust and powerful density functional able to provide accurate structures in large supramolecular aggregates, specifically composites with

P. Salvador, J. J. Dannenberg, S. Dapprich, A. D. Daniels, O. Farkas, J. B. Foresman, J. V. Ortiz, J. Cioslowski, D. J. Fox, *Wallingford CT* **2009**.

[56] T. Yanai, D. P. Tew, N. C. Handy, *Chem. Phys. Lett.* **2004***, 393*, 51-57.

[57] B. Nieto-Ortega, J. Casado, J. T. L. Navarrete, G. Hennrich, F. J. Ramírez, *J. Chem. Theory Comput.* **2011***, 7*, 3314-3322.

[58] F. Di Meo, M. N. Pedersen, J. Rubio-Magnieto, M. Surin, M. Linares, P. Norman, *J. Phys. Chem. Lett.* **2015**, *6*, 355-359.

[59] P. Rivera-Fuentes, B. Nieto-Ortega, W. B. Schweizer, J. T. L. Navarrete, J. Casado, D. Diederich, *Chem. Eur. J.* **2011**, *17*, 3876-3885.

[60] E. Runge, E. K. U. Gross, *Phys. Rev. Lett.* **1984**, *52*, 997-1000.

[61] E. K. U. Gross, W. Kohn, *Advances in Quantum Chemistry*, L. Per-Olov, Academic Press, **1990**, *21*, 255-291.

[62] S. Grimme, *J. Comput. Chem.* **2006**, *27*, 1787-1799.

carbon nanotubes.[63,64,65] The Pople's 3-21G* basis set[66] was employed in both cases to reduce the computational cost.

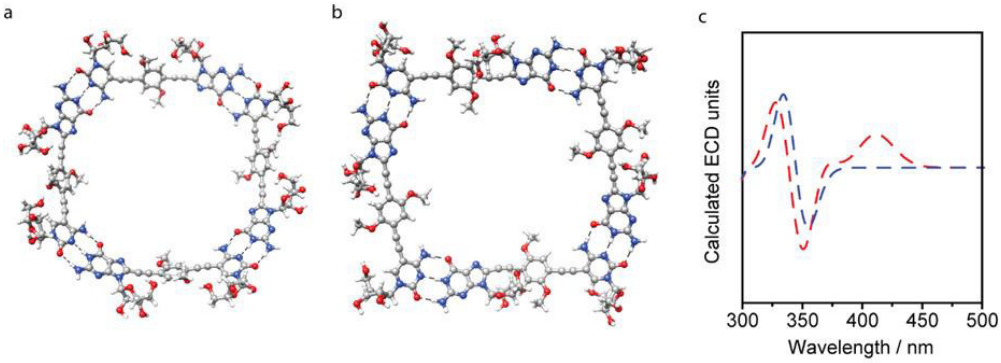

Figure S2. Optimized structure of (a) C_4-symmetric and (b) non-symmetric **GC1** tetrameric ring. (c) Circular dichroism spectra of both conformers: C_4-symmetric (blue) and non-symmetric (red) **GC1** tetrameric ring.

[63] S. Aljohani, A. I. Alrawashdeh, M. Z. H. Khan, Y. Zhao, J. B. Lagowski, *J. Phys. Chem. C* **2017**, *121*, 4692-4702.
[64] B. B. Shirvani, M. B. Shirvani, J. Beheshtian, N. L. Hadipour, *J. Iran. Chem. Soc.* **2011**, *8*, S110-S118.
[65] A. Joshi, C. N. Ramachandran, *Phys. Chem. Chem. Phys.* **2016**, *18*, 14040-14045.
[66] J. S. Binkley, J. A. Pople, W. J. Hehre, *J. Am. Chem. Soc.* **1980**, *102*, 939-947.

$$E_{int} = E_{(6,5)SWCNT-\boldsymbol{GC1}\ composite} - \left(E_{(6,5)SWCNT} - E_{\boldsymbol{GC1}\ tetrameric\ ring}\right)$$

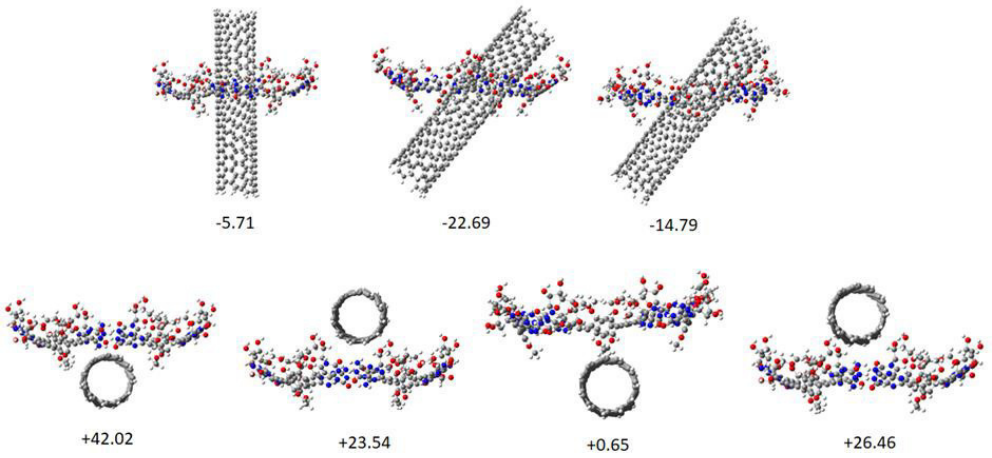

Figure S3. Different configurations of the (6,5)SWCNT-**GC1** composite. Definition of interaction energy (E_{int}) and energy parameters (kcal mol^{-1}) for the different configurations.

Characterization of the (6,5)SWCNT-GC1 conjugates by HR-TEM

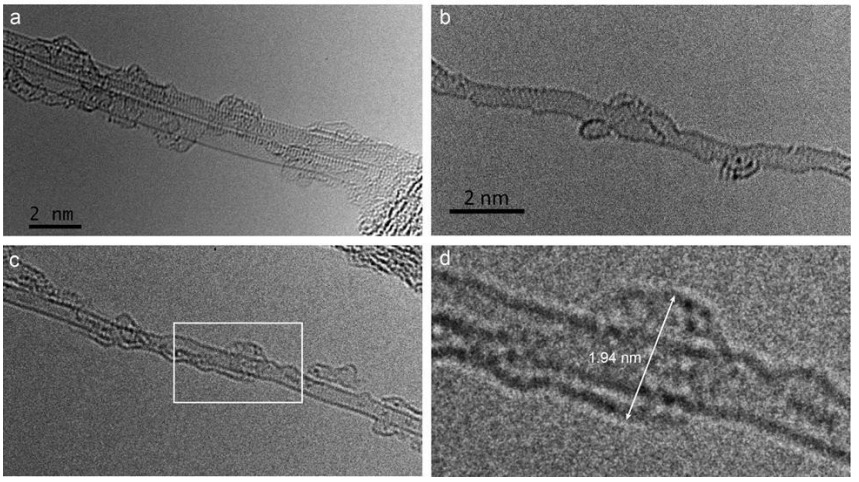

Figure S4. Representative aberration corrected HR-TEM images of SWCNT-**GC1** conjugates. Note that the walls of the SWCNTs are heavily functionalized (a) but the addends, and even the walls of the SWCNT are quickly damaged (b) under the e-beam. In some images, structures that could correspond to the **GC1** macrocycles are still visible (c and d).

Dilution experiments monitored by fluorescence spectroscopy

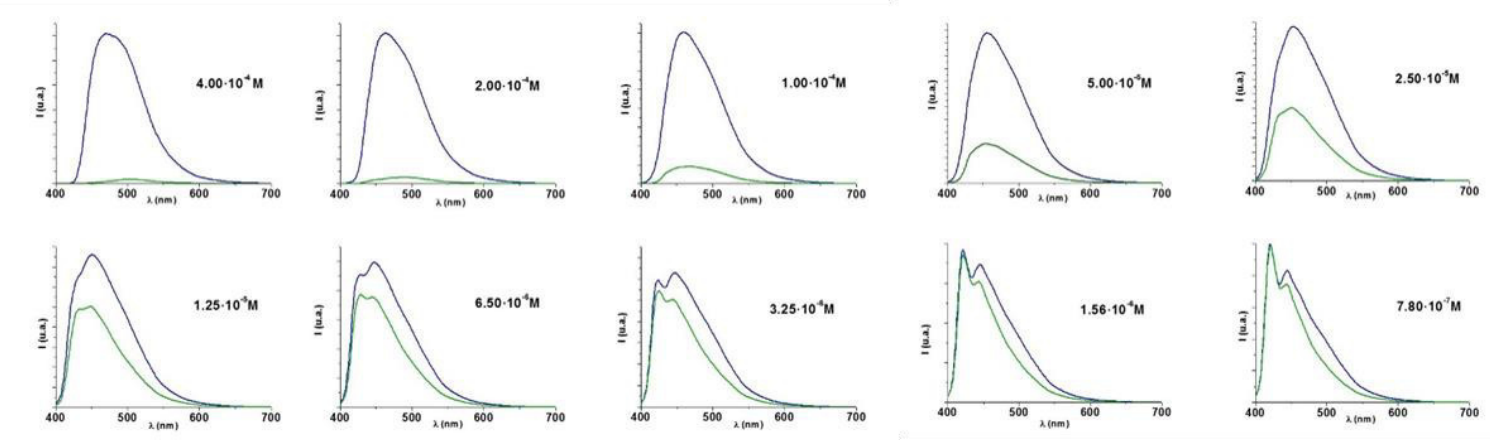

Figure S5A. Selected emission spectra (λ_{exc} = 380 nm) of **GC1** at different concentrations in $CHCl_3$ and in the absence (I_{GC}) (blue line) or presence ($I_{GC\text{-}CNT}$) of (6,5)SWCNTs (green line).

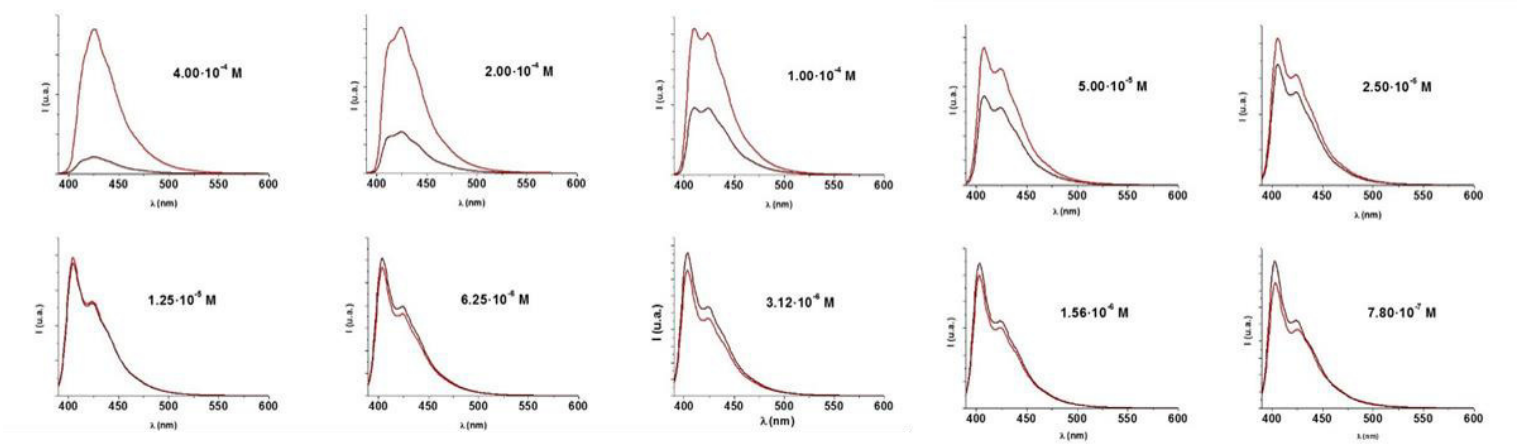

Figure S5B. Selected emission spectra (λ_{exc} = 380 nm) of **CC1** at different concentrations in $CHCl_3$ and in the absence (I_{CC}) (red line) or presence ($I_{CC\text{-}CNT}$) of (6,5)SWCNTs (brown line).

5. ENGINEERING THE OPTOELECTRONIC PROPERTIES OF MoS_2 PHOTODETECTORS THROUGH REVERSIBLE NONCOVALENT FUNCTIONALIZATION

5. Engineering the optoelectronic properties of MoS_2 photodetectors through reversible noncovalent functionalization

We present an easy noncovalent functionalization of MoS_2-based photodetectors that results in an enhancement of the photoresponse by about four orders of magnitude, reaching responsivities up to 100 A W^{-1}. The functionalization is technologically trivial, air-stable, fully reversible and reproducible, and opens the door to the combination of 2D-materials with molecular dyes for the development of high performance photodetectors.

Chem. Commun. **2016**, *52*, 14365-14368.

5.1. Introduction

Among the novel two-dimensional (2D) materials,[1,2,3,4,5,6,7,8] transition metal dichalcogenides (TMDCs)[9,10,11,12] show particularly promising electronic and

[1] A. K. Geim, K. S. Novoselov, *Nat. Mater.* **2007**, *6*, 183-191.
[2] P. Miro, M. Audiffred, T. Heine, *Chem. Soc. Rev.* **2014**, *43*, 6537-6554.
[3] M. Xu, T. Liang, M. Shi, H. Chen, *Chem. Rev.* **2013**, *113*, 3766-3798.
[4] Q. Tang, Z. Zhou, *Prog. Mater. Sci.* **2013**, *58*, 1244-1315.
[5] R. Mas-Balleste, C. Gomez-Navarro, J. Gomez-Herrero, F. Zamora, *Nanoscale* **2011**, *3*, 20-30.
[6] C. N. R. Rao, H. S. S. Ramakrishna Matte, U. Maitra, *Angew. Chem. Int. Ed.* **2013**, *52*, 13162-13185.
[7] G. Le Lay, E. Salomon, P. De Padova, J.-M. Layet, T. Angot, *Aust. J. Chem.* **2014**, *67*, 1370-1372.
[8] S. Z. Butler, S. M. Hollen, L. Cao, Y. Cui, J. A. Gupta, H. R. Gutiérrez, T. F. Heinz, S. S. Hong, J. Huang, A. F. Ismach, E. Johnston-Halperin, M. Kuno, V. V. Plashnitsa, R. D. Robinson, R. S. Ruoff, S. Salahuddin, J. Shan, L. Shi, M. G. Spencer, M. Terrones, W. Windl, J. E. Goldberger, *ACS Nano* **2013**, *7*, 2898-2926.
[9] R. Lv, H. Terrones, A. L. Elías, N. Perea-López, H. R. Gutiérrez, E. Cruz-Silva, L. P. Rajukumar, M. S. Dresselhaus, M. Terrones, *Nano Today* **2015**, *10*, 559-592.
[10] M. Chhowalla, Z. Liu, H. Zhang, *Chem. Soc. Rev.* **2015**, *44*, 2584-2586.
[11] R. Lv, J. A. Robinson, R. E. Schaak, D. Sun, Y. Sun, T. E. Mallouk, M. Terrones, *Acc. Chem. Res.* **2015**, *48*, 56-64.
[12] Q. H. Wang, K. Kalantar-Zadeh, A. Kis, J. N. Coleman, M. S. Strano, *Nat. Nanotechnol.* **2012**, *7*, 699-712.

optoelectronic properties.[13] In particular, their intrinsic bandgap within the visible part of the spectrum, makes them highly interesting materials for optoelectronic applications.[14] In fact, the presence of a bandgap has allowed for the construction of a wealth of prototype electronic devices based on TMDCs.[15,16,17,18,19,20,21,22,23,24] In the last few years, there has been a significant effort to modulate the optical properties of TMDCs in order to optimize the performance of the corresponding devices. Most of the strategies investigated so far have relied on physical methods, such as strain-engineering,[25,26] field-effect doping,[12,27] or artificial stacking of different 2D materials.[28,29] In comparison, the chemical modification of TMDCs is still rather underexplored, despite the appealing combination of low cost and high degree of control offered by synthetic chemistry.

[13] F. H. L. Koppens, T. Mueller, P. Avouris, A. C. Ferrari, M. S. Vitiello, M. Polini, *Nat. Nanotechnol.* **2014**, *9*, 780-793.
[14] H. Zeng, X. Cui, *Chem. Soc. Rev.* **2015**, *44*, 2629-2642.
[15] D. Jariwala, V. K. Sangwan, L. J. Lauhon, T. J. Marks, M. C. Hersam, *ACS Nano* **2014**, *8*, 1102-1120.
[16] K. Kang, S. Xie, L. Huang, Y. Han, P. Y. Huang, K. F. Mak, C.-J. Kim, D. Muller, J. Park, *Nature* **2015**, *520*, 656-660.
[17] M. Chen, H. Nam, H. Rokni, S. Wi, J. S. Yoon, P. Chen, K. Kurabayashi, W. Lu, X. Liang, *ACS Nano* **2015**, *9*, 8773-8785.
[18] Y. Cui, R. Xin, Z. Yu, Y. Pan, Z.-Y. Ong, X. Wei, J. Wang, H. Nan, Z. Ni, Y. Wu, T. Chen, Y. Shi, B. Wang, G. Zhang, Y.-W. Zhang, X. Wang, *Adv. Mater.* **2015**, *27*, 5230-5234.
[19] Y. Ma, B. Liu, A. Zhang, L. Chen, M. Fathi, C. Shen, A. N. Abbas, M. Ge, M. Mecklenburg, C. Zhou, *ACS Nano* **2015**, *9*, 7383-7391.
[20] C. C. Mayorga-Martinez, A. Ambrosi, A. Y. S. Eng, Z. Sofer, M. Pumera, *Adv. Funct. Mater.* **2015**, *25*, 5611-5616.
[21] M. M. Furchi, D. K. Polyushkin, A. Pospischil, T. Mueller, *Nano Lett.* **2014**, *14*, 6165-6170.
[22] B. W. H. Baugher, H. O. H. Churchill, Y. Yang, P. Jarillo-Herrero, *Nat. Nanotechnol.* **2014**, *9*, 262-267.
[23] J. S. Ross, P. Klement, A. M. Jones, N. J. Ghimire, J. Yan, D. G. Mandrus, T. Taniguchi, K. Watanabe, K. Kitamura, W. Yao, D. H. Cobden, X. Xu, *Nat. Nanotechnol.* **2014**, *9*, 268-272.
[24] B. Radisavljevic, A. Radenovic, J. Brivio, V. Giacometti, A. Kis, *Nat. Nanotechnol.* **2011**, *6*, 147-150.
[25] H. J. Conley, B. Wang, J. I. Ziegler, R. F. Haglund, S. T. Pantelides, K. I. Bolotin, *Nano Lett.* **2013**, *13*, 3626-3630.
[26] A. Castellanos-Gomez, R. Roldán, E. Cappelluti, M. Buscema, F. Guinea, H. S. J. van der Zant, G. A. Steele, *Nano Lett.* **2013**, *13*, 5361-5366.
[27] M. Buscema, D. J. Groenendijk, S. I. Blanter, G. A. Steele, H. S. J. van der Zant, A. Castellanos-Gomez, *Nano Lett.* **2014**, *14*, 3347-3352.
[28] C.-H. Lee, G.-H. Lee, A. M. van der Zande, W. Chen, Y. Li, M. Han, X. Cui, G. Arefe, C. Nuckolls, T. F. Heinz, J. Guo, J. Hone, P. Kim, *Nat. Nanotechnol.* **2014**, *9*, 676-681.
[29] M. M. Furchi, A. Pospischil, F. Libisch, J. Burgdörfer, T. Mueller, *Nano Lett.* **2014**, *14*, 4785-4791.

Examples of doping of TMDCs through surface charge-transfer using metal atoms,[30] gases,[31] and a few organic molecules has already been demonstrated.[32,33] Responsivities of just a few A W^{-1} have been reported for MoS_2 photodetectors functionalized with a rhodamine dye,[34] a rather modest value for MoS_2-based photodetectors.

Among the readily available organic dyes, perylenediimides (PDIs) and porphyrins show remarkable optical properties, including large molar absorptivity, *ca.* 10^5 M^{-1} cm^{-1} for PDIs and 10^6 M^{-1} cm^{-1} for porphyrins, and outstanding photostability under ambient conditions. These intrinsic properties have made them two of the most popular families of organic dyes, particularly in the frame of photovoltaics.[35,36,37,38,39,40,41,42,43,44] However, their use for the modulation of the optoelectronic properties of TMDC-based devices has not yet been described. Considering this, we decided to investigate the effects of noncovalent functionalization of MoS_2 photodetectors with PDI and tetraphenyl porphyrin (TPP) depicted in Chart 1. Here, we describe that supramolecular functionalization of mechanically exfoliated MoS_2-based photodetectors with PDI and TPP leads to an enhancement of photocurrent generation by over four orders of magnitude, making

[30] H. Fang, M. Tosun, G. Seol, T. C. Chang, K. Takei, J. Guo, A. Javey, *Nano Lett.* **2013**, *13*, 1991-1995.
[31] H. Fang, S. Chuang, T. C. Chang, K. Takei, T. Takahashi, A. Javey, *Nano Lett.* **2012**, *12*, 3788-3792.
[32] D. Kiriya, M. Tosun, P. Zhao, J. S. Kang, A. Javey, *J. Am. Chem. Soc.* **2014**, *136*, 7853-7856.
[33] D. M. Sim, M. Kim, S. Yim, M.-J. Choi, J. Choi, S. Yoo, Y. S. Jung, *ACS Nano* **2015**, *9*, 12115-12123.
[34] S. H. Yu, Y. Lee, S. K. Jang, J. Kang, J. Jeon, C. Lee, J. Y. Lee, H. Kim, E. Hwang, S. Lee, J. H. Cho, *ACS Nano* **2014**, *8*, 8285-8291.
[35] C. Huang, S. Barlow, S. R. Marder, *J. Org. Chem.* **2011**, *76*, 2386-2407.
[36] X. Zhan, A. Facchetti, S. Barlow, T. J. Marks, M. A. Ratner, M. R. Wasielewski, S. R. Marder, *Adv. Mater.* **2011**, *23*, 268-284.
[37] M. Urbani, M. Gratzel, M. K. Nazeeruddin, T. Torres, *Chem. Rev.* **2014**, *114*, 12330-12396.
[38] M. V. Martinez-Diaz, G. de la Torre, T. Torres, *Chem. Commun.* **2010**, *46*, 7090-7108.
[39] T. Higashino, H. Imahori, *Dalton Trans.* **2015**, *44*, 448-463.
[40] L.-L. Li, E. W.-G. Diau, *Chem. Soc. Rev.* **2013**, *42*, 291-304.
[41] C. B. Nielsen, S. Holliday, H.-Y. Chen, S. J. Cryer, I. McCulloch, *Acc. Chem. Res.* **2015**, *48*, 2803-2812.
[42] E. Kozma, M. Catellani, *Dyes Pigm.* **2013**, *98*, 160-179.
[43] C. Li, H. Wonneberger, *Adv. Mater.* **2012**, *24*, 613-636.
[44] M. M. Bernal, E. M. Perez, *Int. J. Mol. Sci.* **2015**, *16*, 10704-10714.

our functionalized devices highly sensitive (responsivities up to 100 A W^{-1}). The process is technologically trivial, air-stable, reproducible and fully reversible.

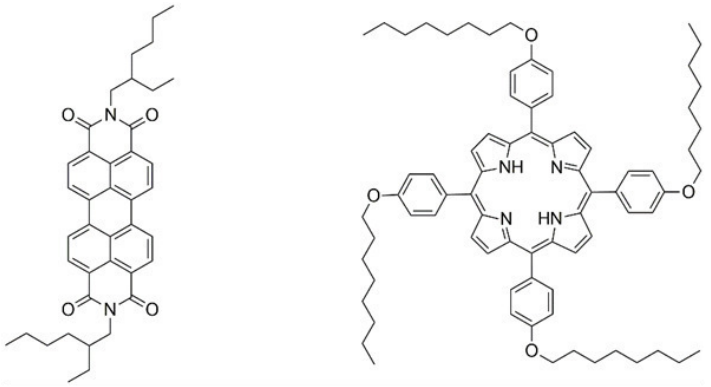

Chart 1. Chemical structure of the perylenediimide and tetraphenyl porphyrin investigated.

5.2. Results and Discussion

MoS_2 phototransistors are fabricated by deterministic transfer of mechanically exfoliated flakes onto pre-patterned drain and source electrodes fabricated by shadow mask evaporation of Ti/Au (5 nm/50 nm) onto a SiO_2 substrate (285 nm in thickness), thermally grown on a highly p-doped silicon chip.[45]

The heavily doped silicon is employed as a back gate electrode to tune the density of charge carriers by the electric field effect. Figure 1a-1 shows an artistic representation of a MoS_2-based field-effect transistor (FET) fabricated by transferring a MoS_2 flake bridging the drain and source electrodes. Figure 1b-1 shows an actual optical microscopy image of a fabricated device composed of a

[45] A. Castellanos-Gomez, M. Buscema, R. Molenaar, V. Singh, L. Janssen, H. S. J. van der Zant, G. A. Steele, *2D Mater.* **2014**, *1*, 011002.

multilayer (~10 layers) MoS_2 flake. Right after the fabrication, we perform the FET characterization of the device in air and under dark conditions by sweeping the drain-source voltage and measuring the current passing through the MoS_2 flake. Figure 1c-1 shows a set of current *vs.* drain-source voltage curves (*IV*s hereafter) acquired at different applied gate voltages. The *IV*s show a typical n-type FET behavior, *i.e.* the current increases with increasing back-gate voltage. The threshold voltage is ~0 V and the mobility is ~2 x 10^{-3} cm^2 V^{-1} s^{-1}, although this value is lower bound since we are measuring with two terminals and a correction, which usually yields higher mobility values (typically ranging from 3 to 100 cm^2 V^{-1} s^{-1}),[46,47,48,49,50] should be taken into account.

Once the pristine device is electronically characterized, we functionalize the surface of the MoS_2 device by drop-casting a CH_2Cl_2 saturated solution containing either PDI or TPP (Figure 1a-2, see the Experimental Section for details on the synthesis of the molecules). The drop is placed on the device, covering both the MoS_2 flake and the electrodes, and it is kept in air until the solvent evaporates, resulting in a uniform coverage of the device with crystallites (Figure 1b-2).

[46] N. R. Pradhan, D. Rhodes, Q. Zhang, S. Talapatra, M. Terrones, P. M. Ajayan, L. Balicas, *Appl. Phys. Lett.* **2013**, *102*, 123105.
[47] A. Castellanos-Gomez, M. Barkelid, A. M. Goossens, V. E. Calado, H. S. J. van der Zant, G. A. Steele, *Nano Lett.* **2012**, *12*, 3187-3192.
[48] H. Li, Z. Yin, Q. He, H. Li, X. Huang, G. Lu, D. W. H. Fam, A. I. Y. Tok, Q. Zhang, H. Zhang, *Small* **2012**, *8*, 63-67.
[49] M. S. Fuhrer, J. Hone, *Nat. Nanotechnol.* **2013**, *8*, 146-147.
[50] S. Ghatak, A. N. Pal, A. Ghosh, *ACS Nano* **2011**, *5*, 7707-7712.

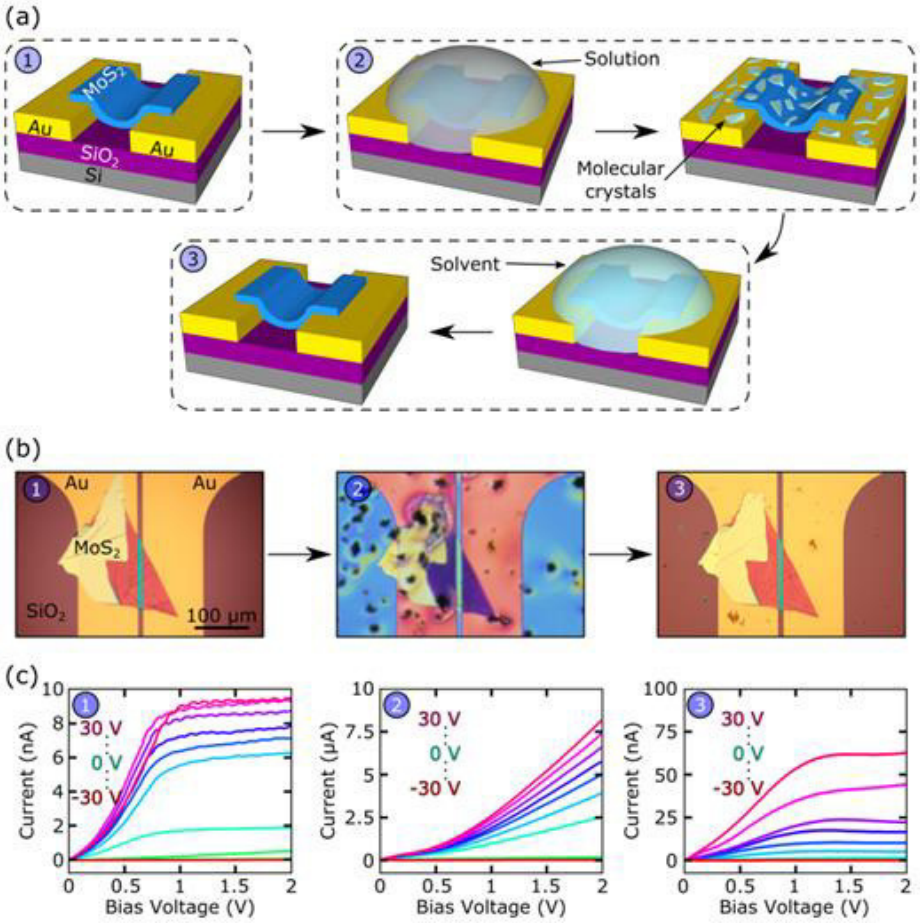

Figure 1. (a) Artistic representation of the fabrication of a MoS_2 phototransistor device subjected to one functionalization-cleaning cycle. (1) The pristine device is fabricated: a few-layer MoS_2 flake is placed bridging two Au electrodes *via* deterministic transfer. (2) Molecular crystals are deposited on the device by drop-casting. (3) The device is washed with solvent to remove the deposited molecules, resulting in a clean device with similar performance as the pristine one. (b) Optical microscopy images of the process described in (a): (1) pristine device; (2) the same device covered with a layer of molecules (TPP in this case); and (3) the same device after removing the molecules. (c) *IV*s of the device shown in (b) for different back-gate voltages (from -30 V to 30 V) at the different steps of the process. Remarkably, after deposition of molecules the current flowing through the device increases by three orders of magnitude.

After deposition of the dyes, the electronic characterization of the device is performed again in air and under dark conditions. Figure 1c-2 shows the *IV*s acquired for different back-gate voltages with the molecule-coated device. As shown, the current is increased with respect to the pristine device by almost three orders of magnitude due to the doping created by the molecules that donate electrons to the MoS_2 flake. Despite the typically electron-acceptor character of PDI, both molecules behave as electron donors when faced with MoS_2. A similar behavior has been observed even with positively charged (*i.e.* very strongly electron-accepting) organic molecules.[32] The result of this electron transfer process is an increase in the n-doping of the material, as can be seen from the shift in the threshold voltage in the current-gate voltage traces (Figure S1 in the Experimental Section). We find that the mobility of the device is also increased from 3 x 10^{-3} cm^2 V^{-1} s^{-1} in the pristine device up to ~1 cm^2 V^{-1} s^{-1} both in the TPP and PDI functionalized devices (more field-effect characteristics of the device are listed in Table S1 of the Experimental Section). The current and mobility enhancement can be also due to the reduction of the Schottky barrier assisted by the molecular doping, as previously reported for MoS_2 FETs doped with Cl, an electron donor, particularly taking into account the fact that we use a chlorinated solvent.[51] However, the difference in results obtained with each molecule, and most convincingly, the fact that we can return to the initial state by washing with CH_2Cl_2 (*vide infra*) unambiguously support a molecule-specific doping mechanism. It is important to note that in the coated devices, the molecules do not contribute significantly to the total current passing through the device (Figure 2). Finally, the device is washed with CH_2Cl_2 in order to remove the molecules, as illustrated in Figure 1a-3. The device almost recovers the initial characteristics (Figure 1b-3), although the current is still slightly enhanced (Figure 1c-3), probably due to the

[51] L. Yang, K. Majumdar, H. Liu, Y. Du, H. Wu, M. Hatzistergos, P. Y. Hung, R. Tieckelmann, W. Tsai, C. Hobbs, P. D. Ye, *Nano Lett.* **2014**, *14*, 6275-6280.

presence of traces of molecules still adsorbed on the MoS_2 surface, or due to the solvent effect mentioned earlier.

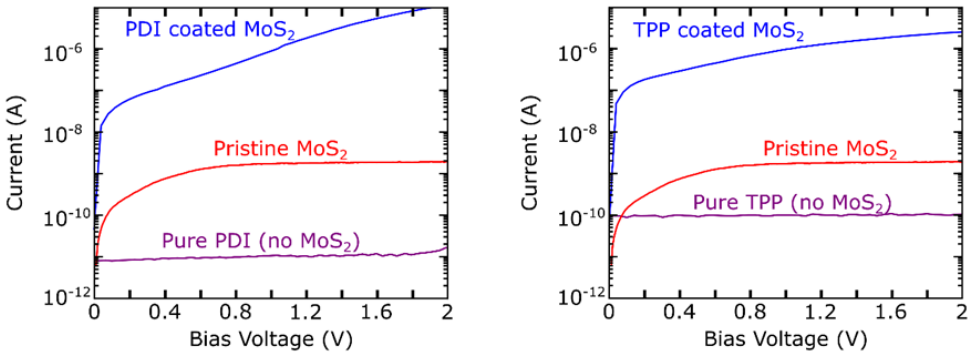

Figure 2. Comparison of the current-voltage curves measured in the pristine device, the coated device and the molecules without MoS_2 bridging the electrodes. It can be seen that the molecules are highly resistive when compared to the coated device.

We characterize the device not only under dark conditions, but also upon illumination. In Figure 3a we show a sketch of the optoelectronic measurement: the device is illuminated with a light beam guided through an optical fiber (the spot on the device has a diameter of 200 µm, illuminating the whole device). The light is switched on and off while measuring the current. In Figures 3b and c we show the photocurrent (I_{ph}, the difference between the current upon illumination and in the dark) as a function of time when the device is coated with PDI (Figure 3b, left) and with TPP (Figure 3c, left). The photocurrent is larger for the PDI coating than that for the TPP coating due to the higher doping of the device by PDI and a better match of its absorption with the light source (see UV-vis spectra in Figure S2 in the Experimental Section). In Figures 3b and c, right, we show the same measurements after cleaning the device with CH_2Cl_2 in order to remove the molecular coating. The

functionalized devices show a most remarkable enhancement of the photocurrent of 2 x 10^4 times for the TPP coating and 3 x 10^4 times for PDI.

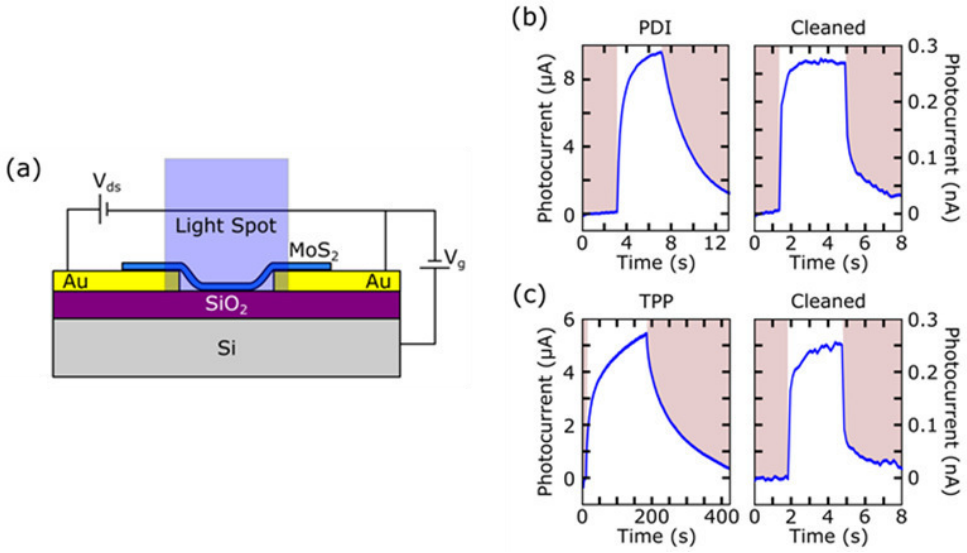

Figure 3. (a) Schematic drawing of the measurement method: a light spot (typically a LED beam guided by an optical fiber) illuminates the whole flake while the current passing through the MoS_2 flake is measured. The light is switched on and off to measure the photocurrent. (b) Photocurrent measured for the device shown in Figure 1b functionalized with PDI (left) and after cleaning the molecules (right) with a light wavelength of 455 nm and a power density of 72 mW cm^{-2} (V_{ds} = 2 V, V_g = 30 V). The photoresponse of the PDI functionalized device is 3 x 10^4 times larger than that of the cleaned device. (c) Photocurrent measured for the device shown in Figure 1b covered by TPP (left) and after removing the molecules (right) with a light wavelength of 455 nm and a power density of 72 mW cm^{-2} (V_{ds} = 2 V, V_g = 30 V). The functionalized device photoresponse is 2 x 10^4 times larger than that after being cleaned.

Note that scanning photocurrent and wavelength dependent photocurrent measurements (Figures 4 and S3 in the Experimental Section, respectively) show that the photocurrent is generated only when the MoS_2 is illuminated, and the absorption of MoS_2 dominates over the absorption of molecules (the photocurrent

spectra after functionalization do not show strong spectral features due to the coating).

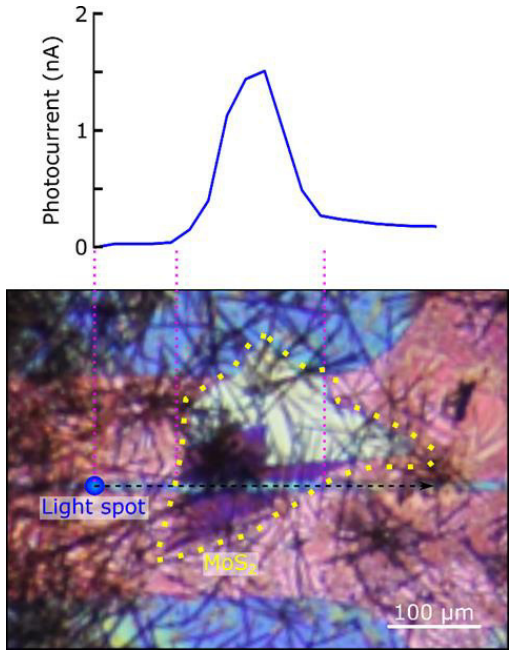

Figure 4. Scanning photocurrent of the PDI-coated device with light wavelength of 455 nm. The light spot (diameter of 25 µm) is displaced over the sample while the current between the source and drain electrodes is measured. As it can be seen, when the light spot is outside the MoS_2 flake there is not photocurrent generation.

In order to study the reproducibility and reversibility of the functionalization/cleaning process, we repeat the characterization several times in the same device, not only coating with one molecule, but also changing the molecule. In Figure 5a we show a plot of the responsivity (R), a figure-of-merit for photodetectors that represents the input-output gain of the device for a given light power. The responsivity is defined as $R = I_{ph}/P_{eff}$, where P_{eff} is the effective light power reaching the device and is calculated as $P_{eff} = P \cdot A_{dev}/A_{spot}$, with P the light

power reaching the substrate, A_{dev} the area of the flake between the two electrodes and A_{spot} the area of the spot on the device.

As shown in Figure 5a, the responsivity of the device is enhanced when it is functionalized with PDI (~10^2 A W^{-1}) by three orders of magnitude with respect to the pristine device (~10^{-1} A W^{-1}). When the device is cleaned, we recover a similar situation to that in the pristine device with a responsivity of ~10^{-2} A W^{-1}. The process is then repeated twice using the same device, obtaining similar values of responsivity with a PDI coating and in the cleaned device.

When the device is functionalized with TPP, the responsivity oscillates between 10^2 A W^{-1} and 10^1 A W^{-1}, and after cleaning the responsivity drops to ~10^{-1} A W^{-1}. The dramatic enhancement of the responsivity originates from the combination of photogating effect and a high photoconductive gain. The photogating effect is translated in the trapping of photogenerated charges in localized states within the bandgap of the material.[46,47] In this case, these states are introduced at the surface of MoS_2 by the functionalization with PDIs or TPPs, making photogenerated holes get trapped in these localized states where they reside for long times, thus quenching the electron-hole recombination and, consequently, increasing the photoconductive gain. Together with the photogating mechanism, hybrid MoS_2/molecular dye systems are expected to present a high photoconductive gain because of the short carrier transit time ($\tau_{transit}$), due to the high mobility of MoS_2, and the long trapping lifetime in the dye molecule ($\tau_{lifetime}$): the gain is $\tau_{lifetime}/\tau_{transit}$.[21,52,53]

We also investigate the rise/fall time of the device with and without the coating, defined as the time measured between 10% and 90% of the maximum

[52] M. Buscema, J. O. Island, D. J. Groenendijk, S. I. Blanter, G. A. Steele, H. S. van der Zant, A. Castellanos-Gomez, *Chem. Soc. Rev.* **2015**, *44*, 3691-3718.
[53] D. Kufer, I. Nikitskiy, T. Lasanta, G. Navickaite, F. H. L. Koppens, G. Konstantatos, *Adv. Mater.* **2015**, *27*, 176-180.

photocurrent in the rising or falling edge. Here, we observe that the rise/fall time increases from ~1 s for the pristine and cleaned devices to ~10 s for the PDI-coated device and to ~300 s for the TPP-coated device (Figure 5b). This indicates that the trapping lifetime of photogenerated holes due to the presence of the dye molecules is 1-2 orders of magnitude longer than those of intrinsic traps in pristine MoS_2 devices, in good agreement with a much higher photoconductive gain in the functionalized devices.

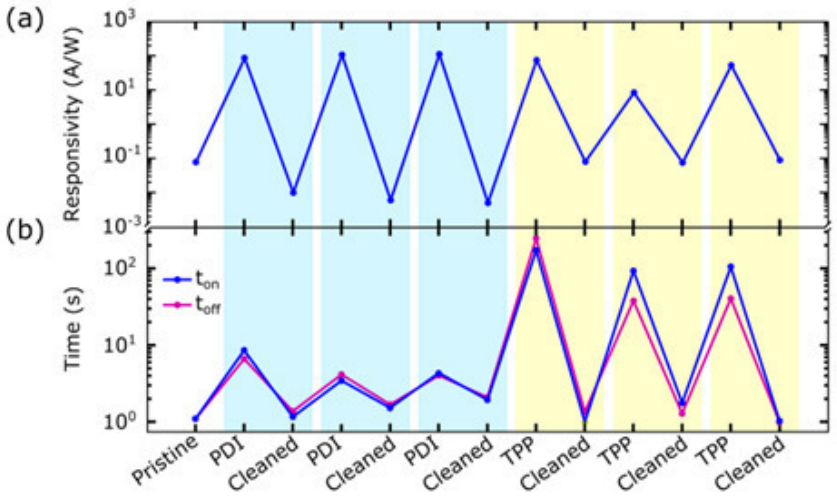

Figure 5. (a) Responsivity for the different cycles of chromophore functionalization and solvent cleaning. The highest responsivity values are achieved when the device is covered with PDI. The LED wavelength is 455 nm, and the power density is 43 mW cm^{-2}. (b) Time response for the different cycles. The fastest response is achieved with the pristine and cleaned devices, but the time response with PDI is just one order of magnitude larger than the pristine device.

5.3. Conclusions

In summary, we have effectively functionalized MoS_2-based photodetectors with PDIs and TPPs using a simple drop-casting method, resulting in a dramatic enhancement of the photoresponse and responsivity (three orders of magnitude higher) to visible light. The process is fully reversible and reproducible, demonstrating that molecular dyes are an easy and interesting way of improving the performance of photodetectors based on two-dimensional materials.

5.4. Experimental Section

Synthesis and characterization of perylenediimide (PDI) and tetraphenyl porphyrin (TPP)

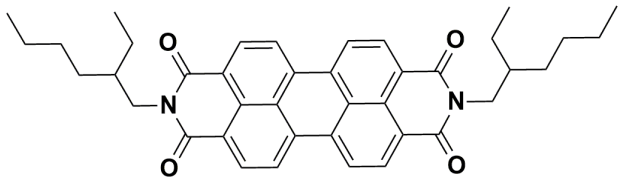

N,N′-bis(2-ethylhexan-1-amine)perylene-3,4,9,10-tetracarboxylic dianhydride was synthesized and characterized as describe in *J. Org. Chem.* **2015**, *80*, 3036-3049, and showed identical spectroscopic data to those reported therein.

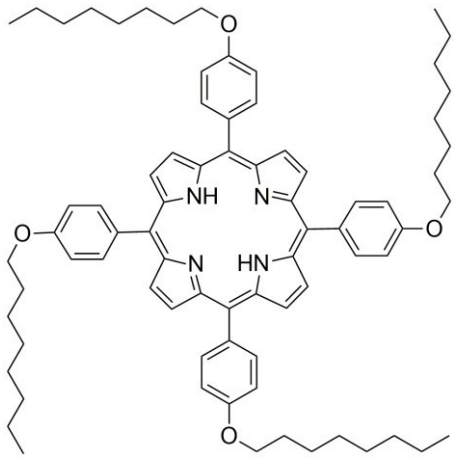

5,10,15,20-tetra-(4-octyloxyphenyl)porphyrin. 5,10,15,20-tetra-(4-hydroxyphenyl)porphyrin (500 mg, 0.74 mmol) was dissolved in dry DMF (100 mL) under argon and K_2CO_3 (2.65 g, 19.16 mmol) was added. 1-bromooctane (1.27 mL, 7.37 mmol) was added dropwise and the resulting mixture was stirred under reflux overnight. The mixture was poured onto cold HCl 1N and the solid was removed by filtration and dissolved in $CHCl_3$, then washed with water. The organic phase was dried over $MgSO_4$ and the solvent was removed under vacuum, obtaining the pure product. This compound (708 mg, 85%) was characterized by ^1H, ^{13}C -NMR and MALDI.

^1H NMR (400 MHz, $CDCl_3$) δ 8.89 (s, 8H), 8.13 (d, *J* = 8.8 Hz, 8H), 7.30 (d, *J* = 8.8 Hz, 8H), 4.28 (t, *J* = 6.5 Hz, 8H), 2.01 (q, *J* = 6.8 Hz, 8H), 1.66 (q, *J* = 7.6 Hz, 8H), 1.55 – 1.38 (m, 32H), 0.97 (t, *J* = 6.9 Hz, 12H), -2.68 (s, 2H). ^{13}C NMR (101 MHz, $CDCl_3$) δ 158.9, 135.6, 134.5, 119.9, 112.7, 68.3, 31.9, 29.5, 29.4, 26.3, 22.8, 14.2. MS m/z: calculated for $C_{76}H_{94}N_4O_4$ 1127.6, found MALDI 1127.7.

Field-effect characteristics of the functionalized MoS_2-based devices

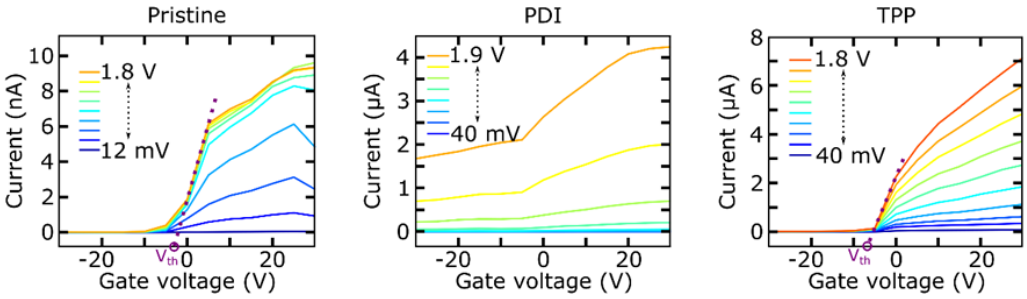

Figure S1. Current-gate voltage traces for different drain-source voltages of the MoS_2-based device, measured in the pristine device, the PDI-coated device and the TPP-coated device.

The current-gate voltage traces are measured in air and under dark conditions. The ON/OFF ratio in the pristine device is 400, with a mobility of 3.4 x 10^{-3} cm^2 V^{-1} s^{-1} and a threshold voltage of ~ -3 V. When the device is coated with PDI, the ON/OFF ratio decreases approximately a factor of 100, the mobility increases a factor of 1000 and the threshold voltage shifts below -30 V, clearly showing a high n-doping due to the presence of the molecules. When the device is coated with TPP, the ON/OFF ratio remains the same, the mobility increases a factor of 1000 and the threshold voltage shifts to ~ -8 V, indicating a moderate n-type doping. Thus, for TPP we attribute the current enhancement to be dominated by a reduction of the Schottky barrier height induced by the molecule/MoS_2 charge transfer rather than the direct n-type doping.

Table S1. Field-effect characteristics of the MoS_2-based device at the different cycles of coating-cleaning-functionalization.

	Mobility ($cm^2\ V^{-1}\ s^{-1}$)	V_{th} (V)	ON/OFF ratio
Pristine	3.4×10^{-3}	-3	460
PDI	0.3	< - 30	10
Cleaned	0.5×10^{-3}	0	30
PDI	1.11	< - 30	10
Cleaned	0.3×10^{-3}	-2	20
PDI	-	-	-
Cleaned	-	-	-
TPP	-	-	-
Cleaned	6.6×10^{-3}	0	1200
TPP	1.1	-8	400
Cleaned	-	-	-
TPP	0.6	-10	10
Cleaned	7.4×10^{-3}	0	2200

UV-vis spectra of PDI and TPP

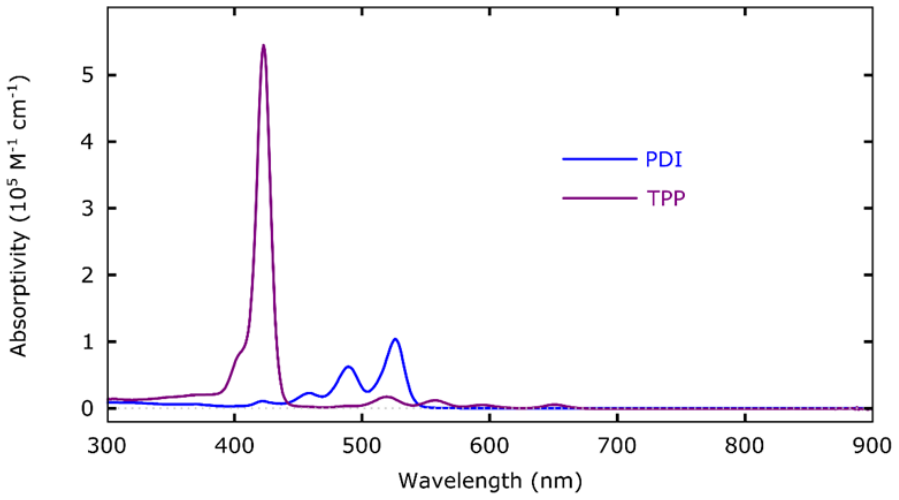

Figure S2. UV-vis absorption spectra of PDI and TPP in CH_2Cl_2.

Optoelectronic characteristics of the functionalized MoS_2-based devices

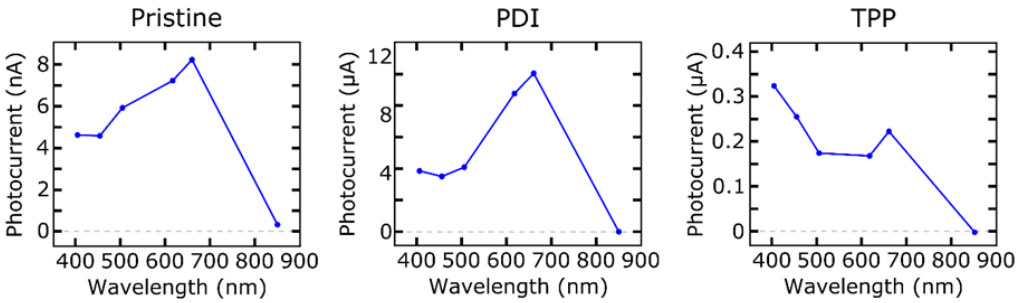

Figure S3. Photocurrent measured in the device as a function of the light wavelength for the pristine device, the PDI-coated device and the TPP-coated device. The LED power is 100 nW and the photocurrent is measured with V_{ds} = 2 V and V_g = 30 V.

As shown in the plots, the device is responding to light for wavelengths shorter than 660 nm, where there is a photocurrent peak related to the MoS_2 A exciton. The photocurrent is enhanced in the coated device about 3 orders of magnitude with respect to the pristine device, although in the TPP-coated device the spectrum seems to be on top of a background which could be due to a high absorption of the TPP at high energies.

6. CONCLUSIONS – CONCLUSIONES

6. Conclusions

- We have synthesized new U-shaped precursors based on porphyrin derivatives and documented their interfacing with SWCNTs *via* mechanical interlocking, through the synthesis of rotaxane-type architectures. The threading of the macrocycles with SWCNTs without introducing defects was confirmed by means of AFM, AC-HRTEM and Raman spectroscopy. Moreover, from Raman and steady state absorption spectroscopy we concluded the selective functionalization of smaller diameter SWCNTs.

- We have explored an unprecedented approach to solubilize SWCNTs in apolar solvents that relies on dynamic macrocycle clamping around the nanotube sidewalls, and on cooperative noncovalent interactions, which supplies the required reversibility to simply and effectively recover the pristine material. The combination of theoretical, spectroscopic and microscopic techniques provide solid evidence of the mutual benefits offered by the combination of these two species: nanoring stability is enhanced in the presence of SWCNTs and H-bonded rings allow for efficient SWCNT debundling and for the production of long-lasting dispersions.

- We have described a simple drop-casting method to functionalize MoS_2-based photodetectors with PDI and TPP, resulting in a great enhancement of the photoresponse (four orders of magnitude) and responsivity (three orders of magnitude) to visible light. Furthermore, the process is fully reversible and reproducible, demonstrating that molecular dyes are an easy and interesting way of improving the performance of photodetectors based on 2D materials.

6. Conclusiones

- Hemos sintetizado nuevos receptores en forma de U basados en derivados de porfirina y hemos analizado su interacción con nanotubos de carbono de pared sencilla (SWCNTs) mediante enlace mecánico, a través de la síntesis de estructuras de tipo rotaxano. El enlace de los macrociclos con los SWCNTs sin introducir defectos en su estructura se confirmó mediante AFM, AC-HRTEM y espectroscopía Raman. Además, con Raman y espectroscopía de absorción de estado estacionario, concluimos una funcionalización selectiva de los SWCNTs de pequeño diámetro.

- Hemos investigado un nuevo método para solubilizar SWCNTs en disolventes apolares que se basa en la colocación de macrociclos alrededor de los nanotubos, y en interacciones cooperativas no covalentes que además proporcionan la reversibilidad necesaria para recuperar de manera efectiva el material prístino. La combinación de técnicas teóricas, espectroscópicas y microscópicas proporciona sólida evidencia de los beneficios mutuos que ofrece la combinación de estas dos especies: la estabilidad del macrociclo mejora en presencia de SWCNTs y, por otro lado, estos macrociclos también permiten una eficiente ruptura de los agregados de SWCNTs, dando lugar a dispersiones de larga duración.

- Hemos descrito un método sencillo basado en 'drop-casting' para funcionalizar fotodetectores de MoS_2 con PDI y TPP, obteniendo un excelente aumento de la fotorrespuesta (cuatro órdenes de magnitud) y la responsividad (tres órdenes de magnitud) a la luz visible. Además, el proceso es completamente reversible y reproducible, demostrando que los colorantes moleculares nos permiten mejorar el rendimiento de los fotodetectores basados en materiales 2D de manera fácil e interesante.